R-1490
CU-387
Nevis-281

Nevis Laboratories
Columbia University
Physics Department
Irvington-on-Hudson, New York

QUASI-ELASTIC PRODUCTION OF CHARMED BARYONS BY NEUTRINOS

Yunsil Ho

Submitted in partial fulfillment of
the requirements for the degree
of Doctor of Philosophy in the
Graduate School of Arts and Sciences,
Columbia University

National Science Foundation
NSF PHY 89-21320

1993

QUASI-ELASTIC PRODUCTION OF CHARMED BARYONS BY NEUTRINOS*†

Yunsil Ho
Columbia University, New York, NY

*Research supported by the National Science Foundation.
†Submitted in partial fulfillment of the requirement for the degree of Doctor of Philosophy in the Graduate School of Arts and Sciences, Columbia University.

Abstract

The data from the E776 WBB neutrino (ν_μ) run and the antineutrino ($\overline{\nu}_\mu$) run have been analyzed for the presence of opposite sign dimuon events. The experiment was performed at the Alternating Gradient Synchrotron (AGS) at Brookhaven National Laboratory (BNL), Upton, New York. The data samples were based on 1,377K AGS pulses of neutrino run and 1,256K AGS pulses of anti-neutrino run. The number of events observed is consistent with the background rate expected for both the neutrino and antineutrino runs. We conclude that there is no evidence for observation of charmed particle production. The expected number of events based on the current theoretical value of cross section times branching ratio for the various charmed particles and the neutrino flux and the acceptance is 0.14. For the antineutrinos, the expected number is nearly zero, as the quasi-elastic production of charmed baryons by antineutrinos is forbidden.

Contents

List of Figures

List of Tables

Acknowledgements

I would like to take this opportunity to thank my thesis advisor, Prof. Wonyong Lee, for his guidance throughout the years.

My special thanks go to Dr. Michael Murtagh, and Dr. Eric Mannel with whom I have had many valuable discussions regarding this work. I would like to thank both of them for meticulously going over my thesis. I also want to thank Dr. George Tzanakos and my fellow graduate student Mr. Jim Mechalakos for many discussions.

I have been involved in P860 proposal at Fermi Lab., and I have had many enlightening discussions with Dr. Mike Gormley, Dr. Allan Bross, Dr. Steve O'Day, Mr. Hyang-Kyu Park, and Mr. Chang-Lyoung Kim.

In my first two years as a graduate student I participated in the Fly's Eye experiment in Utah. I would like to thank Prof. Tom O'Halloran, Prof. Pierre Sokolsky, and Dr. John Boyer for many interesting discussions.

Finally, I would like to thank my parents for encouraging me to pursue graduate program in physics and supporting me during my graduate work at Columbia.

Chapter 1

INTRODUCTION

1.1 Historical Aspects

Wolfgang Pauli postulated the existence of the neutrino, a light and feebly interacting particle [1, 2] to account for the continuous electron energy spectrum seen in beta decay [2]. If the electron were the only particle emitted in beta decay, it would always have an energy equal to the difference between the initial and final nuclear state energies. Measurements showed, however, that some of the energy was being lost.

Beta decay could not be understood without a successful model of the nucleus which came after the discovery of the neutron by Chadwick [3] in 1932. Pauli's hypothesis and the discovery of the neutron lead E. Fermi in 1934 to the formulation of his theory of beta decay [4]. It was not until 1959 that the first direct observation of neutrinos was performed by F. Reines and C. Cowen through the inverse beta decay process [5]. In 1962, an experiment [6] at Brookhaven National Laboratory (BNL) by Danby, Gaillard, Goulianos, Lederman, Mistry, Schwarz, and Steinberger,

observed muon-neutrinos and established that the muon-neutrino is different from the electron-neutrino.

In the Standard Model the lepton family consists of three charged leptons and three neutrinos of three different flavors, each lepton possesses spin 1/2, and for each lepton there is a corresponding antilepton: e^+, μ^+, τ^+, $\overline{\nu}_e$, $\overline{\nu}_\mu$, and $\overline{\nu}_\tau$. The leptons are divided into distinct (left-handed) doublets, or *generations*, as follows:

$$\begin{pmatrix} \nu_e \\ e^- \end{pmatrix} \begin{pmatrix} \nu_\mu \\ \mu^- \end{pmatrix} \begin{pmatrix} \nu_\tau \\ \tau^- \end{pmatrix}$$

Each lepton generation has associated with it an additive quantum number called the *lepton number* (L_e, L_μ, L_τ), which is +1 for each lepton in that generation, -1 for each antilepton of that generation, and 0 for all other particles. In all *observed* processes, each lepton number is conserved.

But experimentally a small amount mixing between the different neutrino flavor states have not been ruled out. As a matter of fact, the most attractive interpretation of the solar neutrino problem is the oscillation of neutrinos as they pass through the sun.

The existence of weak charged current processes has been known for a long time and the existence of strangeness non-changing neutral current was established in 1974 [7, 8, 9, 10, 11, 12]. However, strangeness changing weak neutral currents have not been observed.

By introducing a charmed quark, c, Glashow, Iliopoulos, and Maiani [13] showed that if in addition to the weak charged current transition from an s quark to a u quark,

there was a transition from an s quark to a c quark, there would be a cancellation which suppressed strangeness changing neutral currents.

In November of 1974, a new resonance with an invariant mass of 3.1 GeV (later named the J/Ψ) was discovered at BNL and Stanford Linear Accelerator Center (SLAC) simultaneously by two different experiments. Burton Richter at SLAC was leading an experiment on e^+e^- annihilation [14], while Samuel Ting at BNL was doing an experiment on the production of e^+e^- pairs in the proton-beryllium collisions [15]. Within a short time, the same resonance, J/Ψ, a bound state of a charmed quark and an anticharm quark was also observed in a photo-production experiment at Fermilab [16].

One of several predictions was that charmed particles should also be produced in neutrino induced charged current interactions. The production of charmed particles, mostly charmed mesons, in the deep inelastic reactions was soon observed. The production of charmed baryons by exclusive processes was also predicted.

This thesis discusses the experimental search for such a process.

1.2 Charmed Quark and GIM Mechanism

The existence of a charmed quark was first speculated on as a parallel to the distinct lepton doublets in 1964, but it was not until 1970 that it received serious attention when Glashow, Iliopoulos, and Maiani [13] explained the puzzling absence of strangeness-changing weak neutral currents using this new charmed quark.

In the GIM model, with the introduction of new quark c, it was assumed that

just as the u quark is coupled to the combination d_c in the hadronic charged weak current, so is the charmed quark coupled to the combination of s_c.

$$\begin{pmatrix} d_c \\ s_c \end{pmatrix} = \begin{pmatrix} cos\theta_c & sin\theta_c \\ -sin\theta_c & cos\theta_c \end{pmatrix} \begin{pmatrix} d \\ s \end{pmatrix}$$

In the GIM model, the charged hadronic weak current is written as [17]

$$J_\lambda = \overline{D}_c \gamma_\lambda (1-\gamma_5) U + \overline{S}_c \gamma_\lambda (1-\gamma_5) C \tag{1.1}$$

and the neutral component of the hadronic weak current takes the following form, with the space-time indexes suppressed

$$\overline{U}U + \overline{C}C + \overline{D}_c D_c + \overline{S}_c S_c = \overline{U}U + \overline{C}C + \overline{D}D + \overline{S}S \tag{1.2}$$

In this expression, there are no cross terms like $\overline{D}S$ or $\overline{S}D$. Thus, we expect no neutral weak interactions in which a d quark transforms to an s quark or vice versa.

The GIM formula (Eqs 1.1, and 1.2) for the charged hadronic weak current is a generalization of Cabibbo's hypothesis, and it is further generalized to include 6 quarks in Kobayashi-Maskawa model [18].

1.3 Opposite Sign Dimuons in Charged Current Neutrino Interactions

The charged current neutrino nucleon ($\nu_\mu N$) interaction normally produces one muon, but when the neutrino (ν_μ) energy is high, it can also produce two oppositely charged muons in the final state through both the exclusive and the inclusive processes (as

mentioned earlier, there is no strangeness or charm changing weak neutral current).

$$\nu_\mu + N \rightarrow \mu^- \mu^+ X$$

This can be interpreted as charged current neutrino interaction producing charmed baryon or charmed meson which contains a single heavy charm quark, and this unstable charmed particle subsequently decays into a muon opposite in sign with respect to the muon from the lepton vertex.

The quasi-elastic reactions have lower threshold than the meson production reactions, and consequently, other things being equal, would be a more favorable means of looking for charm. Particularly for the neutrino energies not too far above quasi-elastic reaction thresholds, the exclusive quasi-elastic channel is dominant among such charm producing processes.

According to the generalized Kobayashi-Maskawa model, a charm quark couples to a d, an s, or a b quark. But for neutrino beam energies below 10 GeV (AGS neutrino beam energy range), the massive bottom sea quark can be ignored.

The charm changing part of the charged current in the GIM form of the Weinberg-Salam model is, in terms of quarks fields,

$$J^\mu_{\Delta C} = \bar{c}\gamma^\mu(1-\gamma_5)(-d\sin\theta_c + s\cos\theta_c) \tag{1.3}$$

where θ_c is the Cabibbo angle. This is a $\Delta Q = \Delta C = 1$ transition. This indicates that the observed opposite sign dimuon events in neutrino interactions are from charmed particle production through $d \rightarrow c$ or $s \rightarrow c$ transitions (for antineutrino interactions

$\overline{d} \to \overline{c}$ or $\overline{s} \to \overline{c}$ transitions). Charge conservation prohibits neutrino scattering by $\overline{d}$ and $\overline{s}$, or antineutrino scattering by d and s. Due to the charge conservation, there are no antineutrino induced quasi-elastic charm producing reactions.

Quasi elastic production of single charmed baryons in neutrino interactions can only occur for neutrinos, not for antineutrinos, and is maximally visible when the neutrino energy is not too far above the threshold, since the quasi elastic cross sections soon become constant regardless of the incident neutrino energy, while the total inclusive (noncharm) cross sections rises linearly as the neutrino energy increases.

1.4 Experimental Aspect of Charm Physics

Despite progress made in charm physics since the charmed quark was first introduced, much of the experimental work has concentrated on charmed mesons, not charmed baryons [19]. So our understanding of charmed baryons is not comparable to our understanding of charmed mesons.

In E776, the Wide Band neutrino Beam (WBB) energy ranges up to 10 GeV with a peak energy of $1 \sim 2$ GeV, providing a good place to search for the exclusive production of charmed baryons.

The Status of Exclusive Charmed Baryon Production

A couple of neutrino produced charmed baryons were first observed in the bubble chamber experiment at BNL [20] in 1975. The photoproduction of charmed baryons at FNAL [16] was reported in 1975. In an emulsion experiment at Fermilab [21], three candidates for charmed baryons produced via an exclusive

channel by neutrinos were reported in 1988. As of today, there are no significant measurements of charmed baryon production cross sections in neutrino interactions.

1.5 This Report

We have searched for charmed baryon events via exclusive channels in the BNL E776 detector. The data were taken in 1986 in the wide band beam at BNL. The primary purpose of the experiment was to search for neutrino oscillations of $\nu_\mu(\overline{\nu}_\mu)$ to $\nu_e(\overline{\nu}_e)$, and that study has been completed.

Although the experiment was not optimized to look for charmed baryons, we decided to look for them in this experiment, since there was a report from an earlier experiment with a similar setup that there were an excess of μe events [22]. If this is interpreted as evidence for charmed baryon production with cross sections significantly larger than predicted, we have the opportunity to confirm these results. Although there was a clear excess of μe events, the experiment was not designed to make sign measurements, so there was no indication whether it was $\mu^- e^+$, which would be a signal for this process, or some different combination of sign. In that case, the events should be considered as backgrounds which they could not account for. In this report, we look for $\mu^-\mu^+$ in the neutrino induced reactions; $\mu^-\mu^-$ and $\mu^+\mu^+$ would then be backgrounds. We also expect to observe no $\mu^-\mu^+$ events in the antineutrino data.

Extrapolating from the earlier results, we expected to observe about 30 events [1] in our data. As will be seen, we observe no such significant excess.

[1] Based on private communication with Prof. W. Lee of Columbia University, interpreting the earlier result as charm production. For the E776, the fiducial tonnage is 150 tons, the total protons on target is 1.43×10^{19}, the acceptance for $\mu^-\mu^+$ events in the fiducial volume is 0.28 % (0.28% : the overall acceptance 0.18 % divided by the fiducial factor of 0.64 %), while the earlier result is from the fiducial detector tonnage of 3 tons, 0.38×10^{19} POT, and the acceptance of 7.3×10^{-3}. Assuming the beam spectrum being approximately equal, and the solid angle effect of neutrino flux of 1/20 (E776 detector is further away from the target, and if we assume the $1/r^2$ dependence of the neutrino flux), if they observed 8 events (reported in [22]), then we should be able to observe about 30 events.

Chapter 2

NEUTRINO BEAM AND E776 DETECTOR

2.1 Neutrino Beam

The high energy neutrino beam at BNL was produced using the proton beam extracted from the Alternating Gradient Synchrotron (AGS). The primary proton beam was transported to hit target nuclei in the titanium target, producing secondary particles. Charged mesons in this secondary particle beam were sign selected and focused by two specially designed magnetic horns to transmit a wide range of momentum for pions and kaons. These pions and kaons decay in flight to neutrinos and other particles in an 88 m long decay tunnel, finally producing a Wide Band neutrino Beam (WBB). A 30 m long steel shield at the end of the decay tunnel stopped all the particles except the weakly interacting neutrinos.

An extensive beam Monte Carlo was developed to predict the expected fluxes of the various kinds of neutrinos, ν_μ, $\overline{\nu}_\mu$, ν_e, $\overline{\nu}_e$ in the beam. Beam monitors were placed in the AGS main ring and in the U-line (will be described later in this chapter), for

on-line monitoring, flux normalization, and comparison with Monte Carlo predictions.

2.1.1 Beam Description

The relative scale and locations of the AGS main proton ring, the proton extraction line, meson decay tunnel, and neutrino detector site are shown in Figure 2.1. The diameter of the AGS ring is 258 m and the target to detector distance is 1 km. A more detailed description can be found in [23], [24].

Proton Beam

Protons are injected into the linear accelerator (LINAC) where they are boosted up to 200 MeV/c before injection into the AGS. 200 MeV/c protons from the LINAC are subsequently injected into the AGS where they are accelerated to a final momentum of 28.3 GeV/c. The protons are then extracted in the fast extraction mode (FEB) at repetition rate of 1.4 *sec.* The beam spill has an Radio Frequency (RF) structure consisting of 12 bunches, each with a 35 ns FWHM, and bunch center to center spacing of 224 ns, for a total spill of 2.5 μs. The RF structure for the beam is shown in Figure 2.2.

Although the entire proton spill was dedicated to the neutrino experiment, occasionally one of the twelve bunches would be extracted to a different line for use in another AGS experiment, in the Single Bunch Extraction (SBE) mode. This occurred only for a small portion of the E776 data taking.

The extracted proton beam was transported to the target through the 730 feet

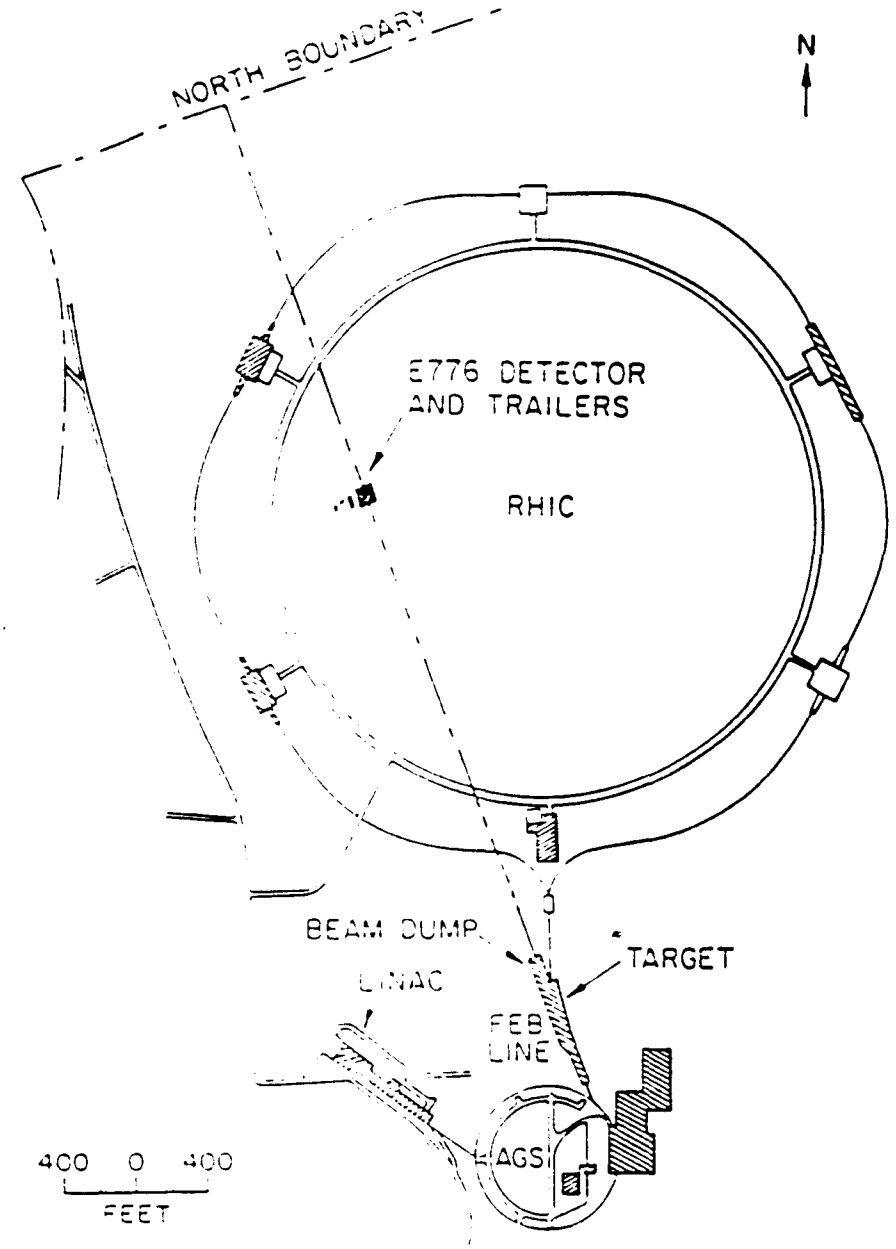

Figure 2.1: Layout of the experiment: AGS main ring, proton extraction line, decay tunnel, and E776 detector site.

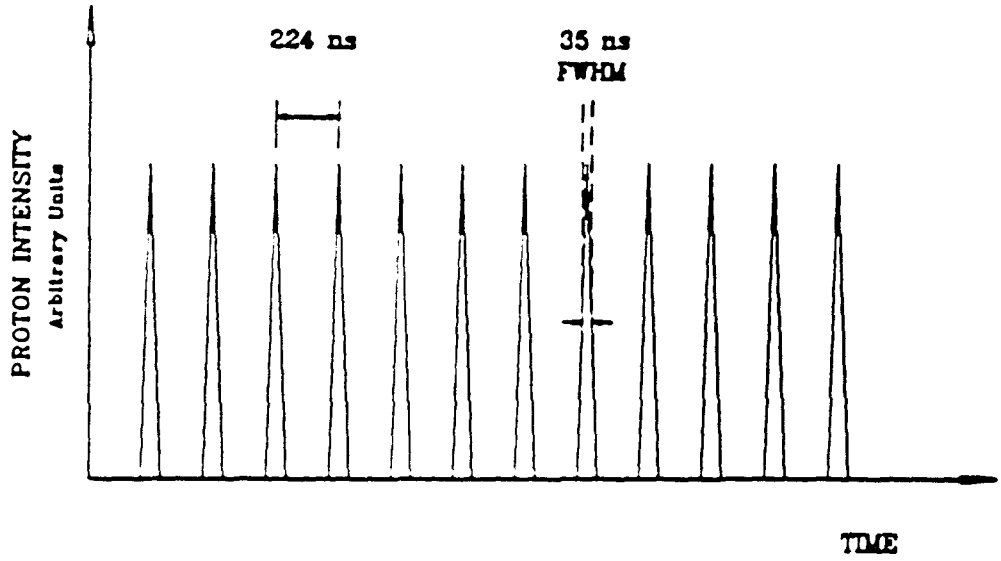

Figure 2.2: The RF structure of the Fast Extracted Beam (FEB): The FEB consists of 12 proton bunches, 35 ns in wide (FWHM), spaced 224 ns apart, resulting in a total spill of 2.5 μs.

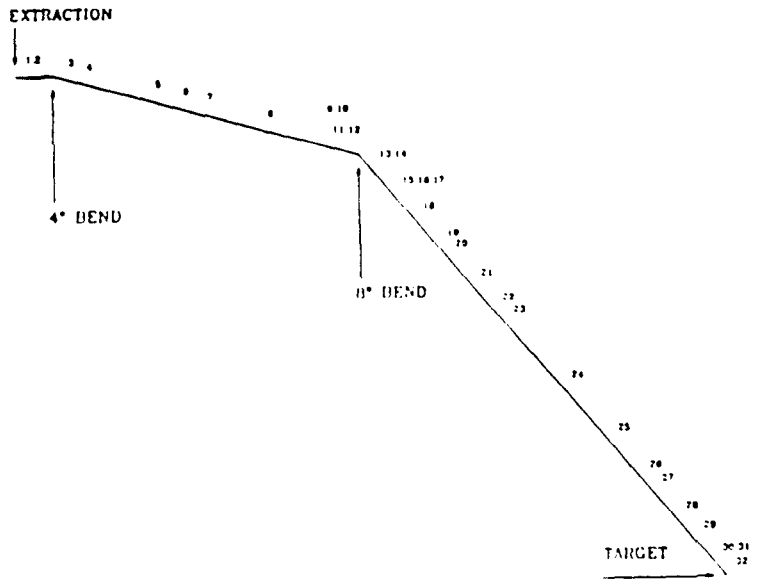

Figure 2.3: Location of radiation loss monitors in the FEB U-line

long U-line. The U-line consisted of a series of magnetic dipoles and quadrupoles.

To minimize the effect of any possible undesired background induced by the scraping of the proton beam on the materials in the transport system, the line bends twice before it finally reaches the target; a 4° bend at 50 feet and an 8° bend at 290 feet after the extraction point. The final segment of U-line points to E776 Neutrino Detector.

The U-line is equipped with 32 radiation monitors distributed throughout the entire length (the locations of these monitors are shown in Figure 2.3). The highest losses occurred between the 4° and 8° bends and near the target.

There are 3 current transformers to measure the intensity of the proton spill. The first one, XCBM, located in the main AGS ring, provides a measure of the number of protons prior to extraction. The other two, the UX15 and the UX716, were located in the U-line, 15 and 716 feet respectively, downstream of the extraction point. Since UX716 was the monitor closest to the target, the proton intensity recorded there is expected to be the best measure of the flux actually delivered to the target and this value is used for the data analysis with the other two monitors providing consistency checks.

Target

The WBB target assembly is shown in Figure 2.4. A cylindrical titanium rod, 6.4 *mm* in diameter and 50.8 *cm* long, divided into ten equal length segments, served as the target for the proton beam. This length of titanium is equivalent to about 1.9 interaction lengths for 28.3 GeV protons. The target is held in a target assembly

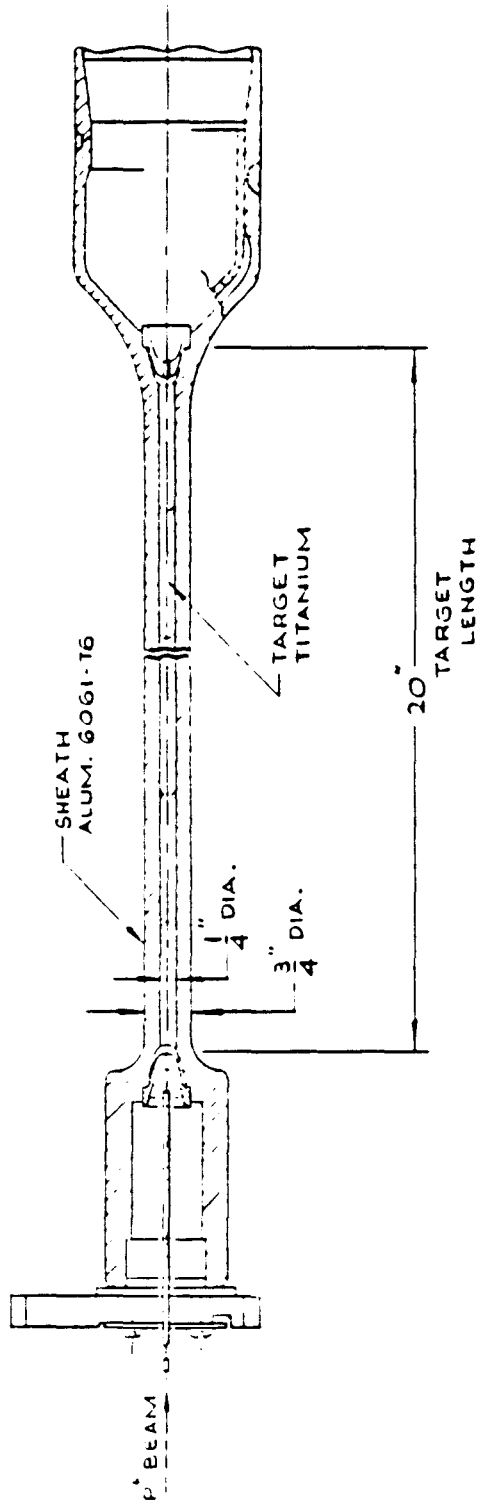

Figure 2.4: WBB proton target assembly

embedded in the front of the first horn. The target segments were pressed into a cylindrical aluminum sheath, with an inner diameter equal to the target diameter and an outer diameter of 18.4 *mm*. The target sheath was evacuated, pressurized with one atmosphere of helium, and sealed. To detect any early disintegration of the target material, the helium pressure in the target enclosure was monitored.

Magnetic Horn Focusing System

A large number of secondary particles are produced when the proton beam hits the titanium target. In order to maximize the neutrino flux and to produce a wide band neutrino beam, it is desirable to focus all the positive particles and defocus the negative particles which are the major source of beam background. The horns were designed to provide high transmission of sign selected charged particles over a wide momentum range (shown in Figure 2.5). The first horn is 213 *cm* long, and the second is 152 *cm* long. The entire length of the horn system is a little longer than 10 *m*. For the WBB run, the horns were driven at a current of 290 *kA*.

These two current carrying cylindrically symmetric aluminum horns focused sign selected charged particles emerging from the target into a nearly parallel beam travelling in the decay tunnel in the direction of the neutrino detector. Figure 2.6 shows the typical focused pion trajectories in the magnetic horn system.

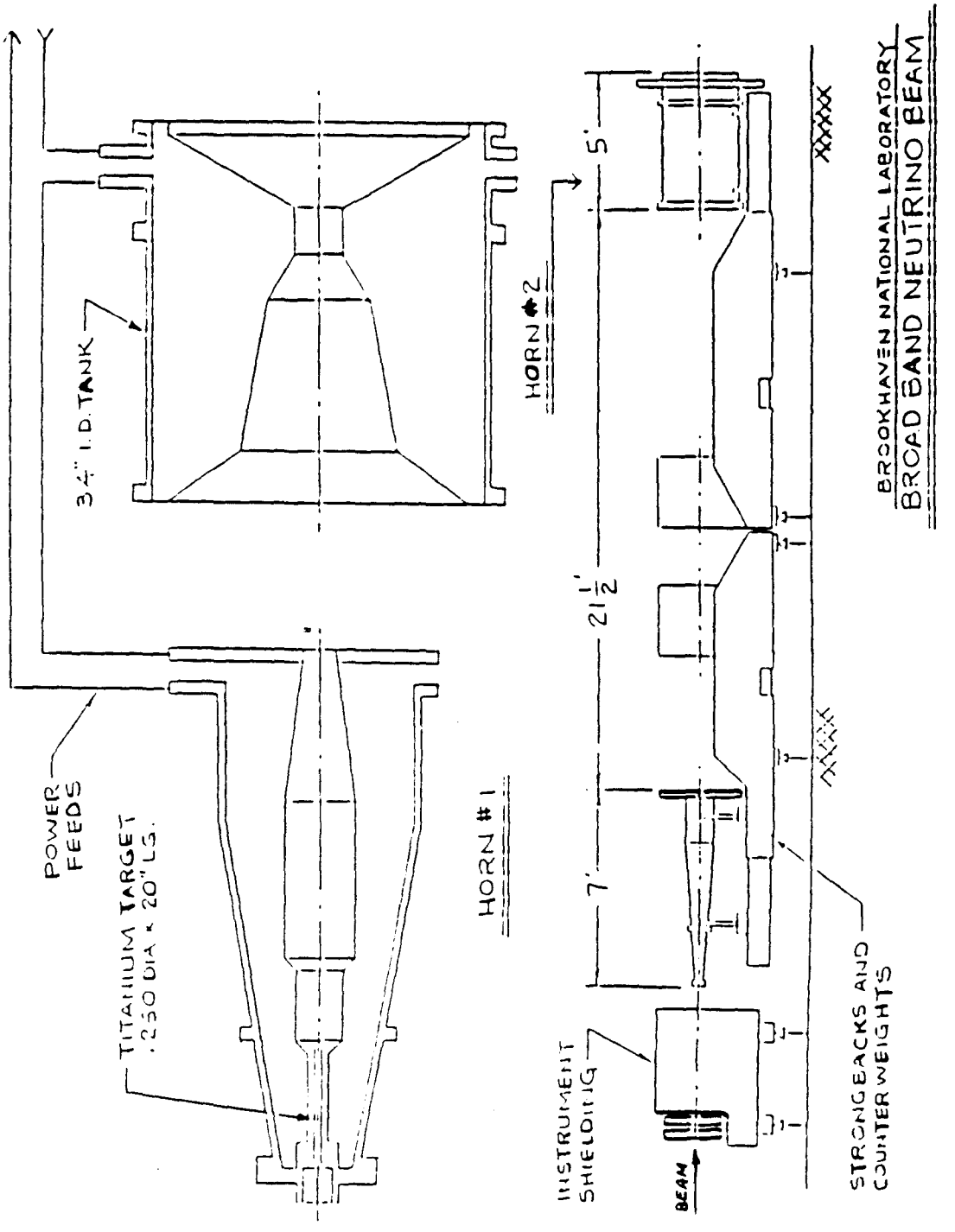

Figure 2.5: Schematic of the WBB horn system

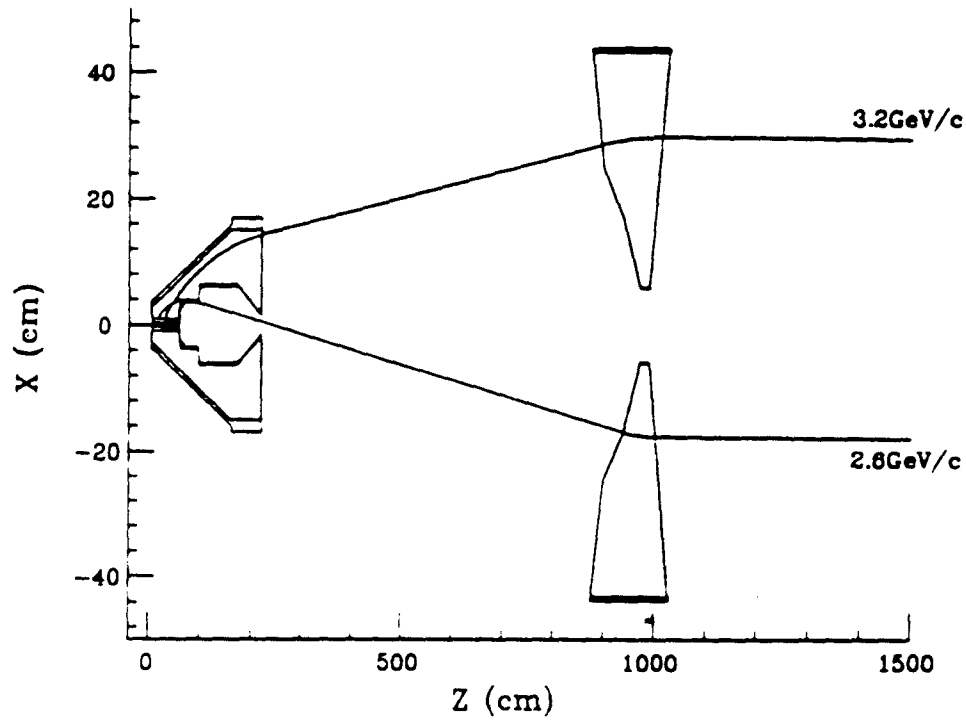

Figure 2.6: The magnetic horn system: typical focused pion trajectories in the horns. The horns are cylindrically symmetric with the proton target embedded in the front of the first horn.

Decay Tunnel and Muon Shield

Sign selected charged mesons decay in flight to yield neutrinos in the 88 m long decay tunnel between the target and beam stop. For the WBB, about half the pions and almost all the kaons decay in the tunnel. The horn system occupied about the first ten meters of the tunnel, which also housed pion monitors and Cerenkov counters. A schematic drawing of the tunnel is shown in Figure 2.7.

Three lucite Cerenkov counters, one located at 44 m and the other two at 49 m from the target, were used for beam timing by monitoring the time difference between the AGS pulse and the counter signal with 6 ns accuracy. The signals from the counters were gated with the beam trigger and sent to the data acquisition system. The Cerenkov time was used to correct for fluctuations in the extraction time.

Two pion monitors, segmented parallel plate ionization chambers, located 70 m downstream from the target, measured the charged secondary beam for on-line monitoring, and comparison with Monte Carlo calculations. Since the intensity of the beam was high enough to saturate the monitors, they could not be placed directly in the beam line. Instead two identical pion monitors were placed symmetrically off the beam axis to measure the flux.

A Muon Shield followed the decay tunnel. This was designed to stop muons produced by the decaying pions and kaons, along with the remaining mesons, protons, neutrons, and photons. The weakly interacting neutrinos passed through, producing the neutrino beam.

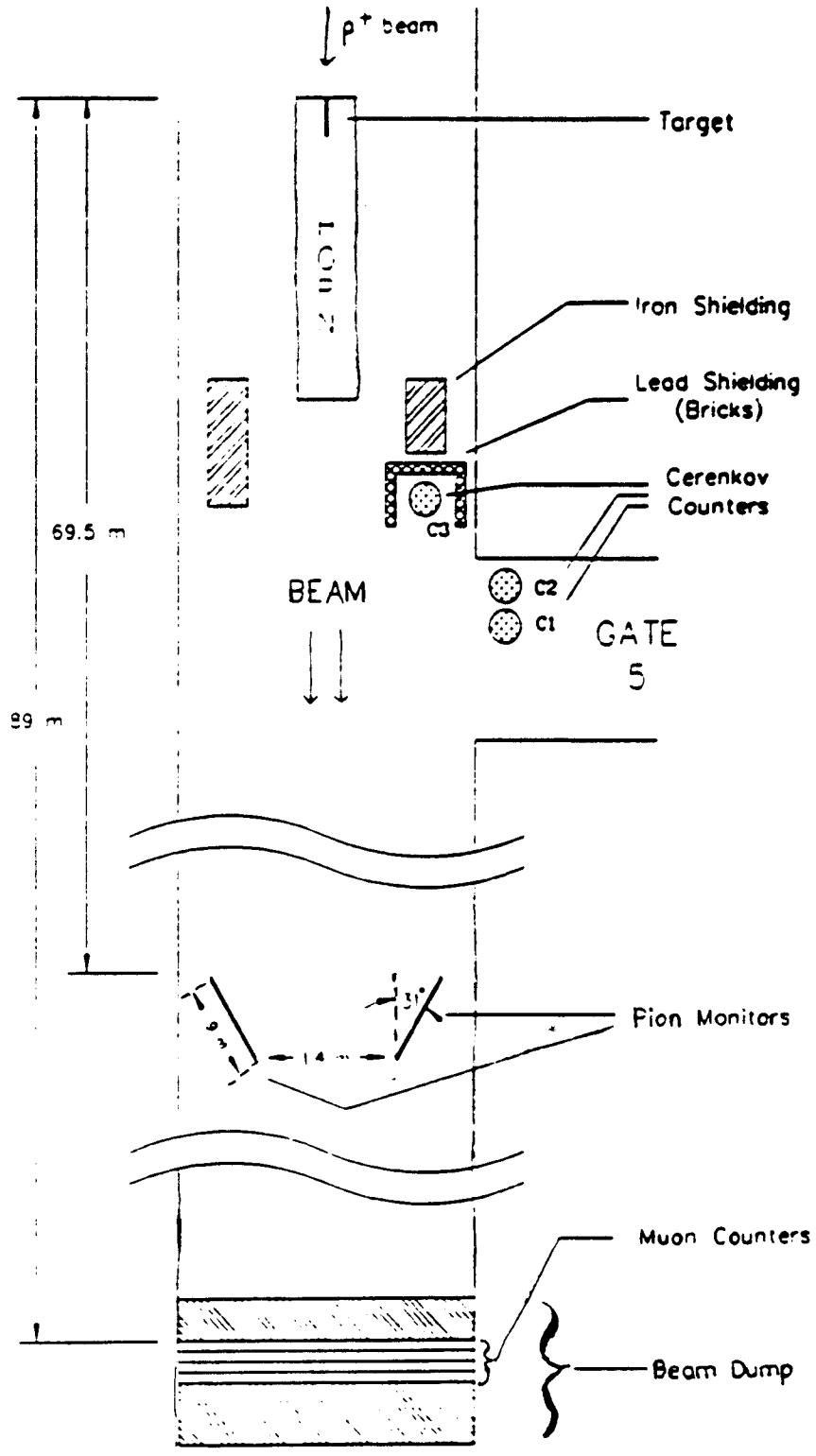

Figure 2.7: Decay tunnel configuration

Two long drift chambers installed in specially designed holes in the muon shield were used to monitor the beam alignment and intensity, and to compared it with Monte Carlo predictions.

2.1.2 Beam Monte Carlo

Production Models of Proton-Nucleus Collision

An extensive beam Monte Carlo, called BMTRAN, was developed to predict the expected fluxes and spectra of ν_μ, $\overline{\nu}_\mu$, ν_e, $\overline{\nu}_e$ in the primarily ν_μ ($\overline{\nu}_\mu$) beam. This program was tested extensively with the previously run E776 Narrow Band Neutrino Beam, and proven to be in good agreement with the pion monitors and neutrino data. A detailed description of BMTRAN and the tests of its predictions can be found in references [23] and [24]. The program was modified to accommodate the WBB target (titanium) and horn system, and monitor locations which are different from those of the NBB run.

The hadron production in proton-nucleus collisions at proton momentum around 28 GeV/c were calculated using 3 different models, they were:

- EVENTQ (EVQ) [25] which consists of two models:
  - NUCEVT: a multi-chain fragmentation model for projectile momenta above 5 GeV/c [26, 27].
  - NUCLIN: a resonance production model for projectile momenta below 5 GeV/c [28].

- GHR [29]: a parameterized model by Grote, Hagendorn, and Ranft which provides production spectra for solid targets from the Atlas of Particle Spectra.

- SW [30]: a semi-empirical model by Sanford and Wang which provides the production formula by fitting existing measurements at various momenta and angles.

The production spectra of pions and all other particles except kaons were obtained directly from EVQ. The K^+/π^+ ratio showed some difference between EVQ and GHR, and the GHR parameterization was used for kaon production. The discussions as to how big the difference is and why we used the GHR model can be found in [23]. The SW model and the GHR model for pion and proton production are compared as a redundancy.

Neutrino Sources and Fluxes

All possible decay modes of secondary particles originating from proton-nucleus collisions which can produce neutrinos in their final state were considered in BMTRAN. Unstable particles are also allowed to decay during transport. Pions and kaons are the dominant sources of neutrinos.

Decay modes leading to each flavor of neutrino productions are listed in Tables 2.1, 2.2, 2.3, 2.4. Integrated dominant contributions to the fluxes and the total neutrino flux are tabulated in Table 2.5 for the $\nu-$run, and Table 2.6 for the $\overline{\nu}-$run.

The spectra of the dominant neutrino producing sources of the charged and neutral

1. $\pi^+ \rightarrow \mu^+\nu_\mu$
2. $K^+ \rightarrow \mu^+\nu_\mu$
3. $K^+ \rightarrow \pi^0\pi^+ \rightarrow \mu^+\nu_\mu$
4. $K^+ \rightarrow \pi^0\mu^+\nu_\mu$
5. $\pi^- \rightarrow \mu^-\bar{\nu}_\mu \rightarrow e^-\nu_\mu\bar{\nu}_e$
6. $K^- \rightarrow \mu^-\bar{\nu}_\mu \rightarrow e^-\nu_\mu\bar{\nu}_e$
7. $K^- \rightarrow \pi^0\mu^-\bar{\nu}_\mu \rightarrow e^-\nu_\mu\bar{\nu}_e$
8. $K^- \rightarrow \pi^0\pi^- \rightarrow \mu^-\bar{\nu}_\mu \rightarrow e^-\nu_\mu\bar{\nu}_e$
9. $K_S^0 \rightarrow \pi^-\pi^+ \rightarrow \mu^+\nu_\mu$
10. $K_S^0 \rightarrow \pi^-\pi^+ \rightarrow \mu^-\bar{\nu}_\mu \rightarrow e^-\nu_\mu\bar{\nu}_e$
11. $K_L^0 \rightarrow \pi^+e^-\bar{\nu}_e \rightarrow \mu^+\nu_\mu$
12. $K_L^0 \rightarrow \pi^-\mu^+\nu_\mu$
13. $K_L^0 \rightarrow \pi^+\mu^-\bar{\nu}_\mu \rightarrow \mu^+\nu_\mu$
14. $K_L^0 \rightarrow \pi^+\mu^-\bar{\nu}_\mu \rightarrow e^-\nu_\mu\bar{\nu}_e$
15. $K_L^0 \rightarrow \pi^-e^+\nu_e \rightarrow \mu^-\bar{\nu}_\mu \rightarrow e^-\nu_\mu\bar{\nu}_e$
16. $K_L^0 \rightarrow \pi^-\mu^+\nu_\mu \rightarrow \mu^-\bar{\nu}_\mu \rightarrow e^-\nu_\mu\bar{\nu}_e$
17. $K_L^0 \rightarrow \pi^0\pi^-\pi^+ \rightarrow \mu^+\nu_\mu$
18. $K_L^0 \rightarrow \pi^0\pi^-\pi^+ \rightarrow \mu^-\bar{\nu}_\mu \rightarrow e^-\nu_\mu\bar{\nu}_e$

Table 2.1: Decay modes leading to ν_μ production

1. $\pi^+ \rightarrow \mu^+\nu_\mu \rightarrow e^+\bar{\nu}_\mu\nu_e$
2. $\pi^+ \rightarrow e^+\nu_e$
3. $K^+ \rightarrow \pi^0e^+\nu_e$
4. $K^+ \rightarrow \mu^+\nu_\mu \rightarrow e^+\bar{\nu}_\mu\nu_e$
5. $K^+ \rightarrow \pi^0\mu^+\nu_\mu \rightarrow e^+\bar{\nu}_\mu\nu_e$
6. $K^+ \rightarrow \pi^0\pi^+ \rightarrow \mu^+\nu_\mu \rightarrow e^+\bar{\nu}_\mu\nu_e$
7. $K_S^0 \rightarrow \pi^-\pi^+ \rightarrow e^+\nu_e$
8. $K_S^0 \rightarrow \pi^-\pi^+ \rightarrow \mu^+\nu_\mu \rightarrow e^+\bar{\nu}_\mu\nu_e$
9. $K_L^0 \rightarrow \pi^-e^+\nu_e$
10. $K_L^0 \rightarrow \pi^+e^-\bar{\nu}_e \rightarrow e^+\nu_e$
11. $K_L^0 \rightarrow \pi^+\mu^-\bar{\nu}_\mu \rightarrow e^+\nu_e$
12. $K_L^0 \rightarrow \pi^-\mu^+\nu_\mu \rightarrow e^+\bar{\nu}_\mu\nu_e$
13. $K_L^0 \rightarrow \pi^+e^-\bar{\nu}_e \rightarrow \mu^+\nu_\mu \rightarrow e^+\bar{\nu}_\mu\nu_e$
14. $K_L^0 \rightarrow \pi^+\mu^-\bar{\nu}_\mu \rightarrow \mu^+\nu_\mu \rightarrow e^+\bar{\nu}_\mu\nu_e$
15. $K_L^0 \rightarrow \pi^0\pi^-\pi^+ \rightarrow e^+\nu_e$
16. $K_L^0 \rightarrow \pi^0\pi^-\pi^+ \rightarrow \mu^+\nu_\mu \rightarrow e^+\bar{\nu}_\mu\nu_e$

Table 2.2: Decay modes leading to ν_e production

1. $\pi^- \rightarrow \mu^- \overline{\nu}_\mu$
2. $K^- \rightarrow \mu^- \overline{\nu}_\mu$
3. $K^- \rightarrow \pi^0 \pi^- \rightarrow \mu^- \overline{\nu}_\mu$
4. $K^- \rightarrow \pi^0 \mu^- \overline{\nu}_\mu$
5. $\pi^+ \rightarrow \mu^+ \nu_\mu \rightarrow e^+ \overline{\nu}_\mu \nu_e$
6. $K^+ \rightarrow \mu^+ \nu_\mu \rightarrow e^+ \overline{\nu}_\mu \nu_e$
7. $K^+ \rightarrow \pi^0 \mu^+ \nu_\mu \rightarrow e^+ \overline{\nu}_\mu \nu_e$
8. $K^+ \rightarrow \pi^0 \pi^+ \rightarrow \mu^+ \nu_\mu \rightarrow e^+ \overline{\nu}_\mu \nu_e$
9. $K_S^0 \rightarrow \pi^- \pi^+ \rightarrow \mu^- \overline{\nu}_\mu$
10. $K_S^0 \rightarrow \pi^- \pi^+ \rightarrow \mu^+ \nu_\mu \rightarrow e^+ \overline{\nu}_\mu \nu_e$
11. $K_L^0 \rightarrow \pi^+ \mu^- \overline{\nu}_\mu$
12. $K_L^0 \rightarrow \pi^- e^+ \nu_e \rightarrow \mu^- \overline{\nu}_\mu$
13. $K_L^0 \rightarrow \pi^- \mu^+ \nu_\mu \rightarrow \mu^- \overline{\nu}_\mu$
14. $K_L^0 \rightarrow \pi^- \mu^+ \nu_\mu \rightarrow e^+ \overline{\nu}_\mu \nu_e$
15. $K_L^0 \rightarrow \pi^+ e^- \overline{\nu}_e \rightarrow \mu^+ \nu_\mu \rightarrow e^+ \overline{\nu}_\mu \nu_e$
16. $K_L^0 \rightarrow \pi^+ \mu^- \overline{\nu}_\mu \rightarrow \mu^+ \nu_\mu \rightarrow e^+ \overline{\nu}_\mu \nu_e$
17. $K_L^0 \rightarrow \pi^0 \pi^- \pi^+ \rightarrow \mu^- \overline{\nu}_\mu$
18. $K_L^0 \rightarrow \pi^0 \pi^- \pi^+ \rightarrow \mu^+ \nu_\mu \rightarrow e^+ \overline{\nu}_\mu \nu_e$

Table 2.3: Decay modes leading to $\overline{\nu}_\mu$ production

1. $\pi^- \rightarrow e^- \overline{\nu}_e$
2. $\pi^- \rightarrow \mu^- \overline{\nu}_\mu \rightarrow e^- \nu_\mu \overline{\nu}_e$
3. $K^- \rightarrow \pi^0 e^- \overline{\nu}_e$
4. $K^- \rightarrow \mu^- \overline{\nu}_\mu \rightarrow e^- \nu_\mu \overline{\nu}_e$
5. $K^- \rightarrow \pi^0 \mu^- \overline{\nu}_\mu \rightarrow e^- \nu_\mu \overline{\nu}_e$
6. $K^- \rightarrow \pi^0 \pi^- \rightarrow \mu^- \overline{\nu}_\mu \rightarrow e^- \nu_\mu \overline{\nu}_e$
7. $K_S^0 \rightarrow \pi^- \pi^+ \rightarrow e^- \overline{\nu}_e$
8. $K_S^0 \rightarrow \pi^- \pi^+ \rightarrow \mu^- \overline{\nu}_\mu \rightarrow e^- \nu_\mu \overline{\nu}_e$
9. $K_L^0 \rightarrow \pi^+ e^- \overline{\nu}_e$
10. $K_L^0 \rightarrow \pi^- e^+ \nu_e \rightarrow e^- \overline{\nu}_e$
11. $K_L^0 \rightarrow \pi^- \mu^+ \nu_\mu \rightarrow e^- \overline{\nu}_e$
12. $K_L^0 \rightarrow \pi^+ \mu^- \overline{\nu}_\mu \rightarrow e^- \nu_\mu \overline{\nu}_e$
13. $K_L^0 \rightarrow \pi^- e^+ \nu_e \rightarrow \mu^- \overline{\nu}_\mu \rightarrow e^- \nu_\mu \overline{\nu}_e$
14. $K_L^0 \rightarrow \pi^- \mu^+ \nu_\mu \rightarrow \mu^- \overline{\nu}_\mu \rightarrow e^- \nu_\mu \overline{\nu}_e$
15. $K_L^0 \rightarrow \pi^0 \pi^- \pi^+ \rightarrow e^- \overline{\nu}_e$
16. $K_L^0 \rightarrow \pi^0 \pi^- \pi^+ \rightarrow \mu^- \overline{\nu}_\mu \rightarrow e^- \nu_\mu \overline{\nu}_e$
17. $\Lambda^0 \rightarrow p e^- \overline{\nu}_e$

Table 2.4: Decay modes leading to $\overline{\nu}_e$ production

ν_μ flux		
Source	Integrated flux	Percent of total
$\pi^+ \rightarrow \mu^+\nu_\mu$	2.2×10^{-5}	95
$K^+ \rightarrow \mu^+\nu_\mu$	7.3×10^{-7}	3
$K^0_S \rightarrow \pi^-\pi^+ \rightarrow \mu^+\nu_\mu$	5.7×10^{-7}	2
Total	2.3×10^{-5}	100

ν_e flux		
Source	Integrated flux	Percent of total
$K^+ \rightarrow \pi^0 e^+\nu_e$	6.4×10^{-8}	44
$\pi^+ \rightarrow \mu^+\nu_\mu \rightarrow e^+\bar{\nu}_\mu\nu_e$	6.2×10^{-8}	42
$K^0_L \rightarrow \pi^- e^+\nu_e$	1.4×10^{-8}	10
$\pi^+ \rightarrow e^+\nu_e$	3.3×10^{-9}	2
$K^+ \rightarrow \mu^+\nu_\mu \rightarrow e^+\bar{\nu}_\mu\nu_e$	2.1×10^{-9}	1
$K^0_S \rightarrow \pi^-\pi^+ \rightarrow \mu^+\nu_\mu \rightarrow e^+\bar{\nu}_\mu\nu_e$	2.2×10^{-9}	1
Total	1.4×10^{-7}	100

$\bar{\nu}_\mu$ flux		
Source	Integrated flux	Percent of total
$\pi^- \rightarrow \mu^-\bar{\nu}_\mu$	7.1×10^{-7}	84
$\pi^+ \rightarrow \mu^+\nu_\mu \rightarrow e^+\bar{\nu}_\mu\nu_e$	6.0×10^{-8}	7
$K^- \rightarrow \mu^-\bar{\nu}_\mu$	3.4×10^{-8}	4
$K^0_S \rightarrow \pi^-\pi^+ \rightarrow \mu^-\bar{\nu}_\mu$	1.6×10^{-8}	2
$K^0_L \rightarrow \pi^+\mu^-\bar{\nu}_\mu$	1.0×10^{-8}	1
Total	8.4×10^{-7}	100

$\bar{\nu}_e$ flux		
Source	Integrated flux	Percent of total
$K^0_L \rightarrow \pi^+ e^-\bar{\nu}_e$	1.5×10^{-8}	76
$K^- \rightarrow \pi^0 e^-\bar{\nu}_e$	3.0×10^{-9}	14
$\pi^- \rightarrow \mu^-\bar{\nu}_\mu \rightarrow e^-\nu_\mu\bar{\nu}_e$	1.3×10^{-9}	4
$\Lambda^0 \rightarrow pe^-\bar{\nu}_e$	1.1×10^{-9}	4
Total	1.9×10^{-8}	100

Table 2.5: Integrated flux of dominant decay modes and the total neutrino flux in $\nu-$run. The flux is per proton on target per m^2.

$\bar{\nu}_\mu$ flux		
Source	Integrated flux	Percent of total
$\pi^- \rightarrow \mu^- \bar{\nu}_\mu$	1.6×10^{-5}	95
$K_S^0 \rightarrow \pi^- \pi^+ \rightarrow \mu^- \bar{\nu}_\mu$	5.6×10^{-7}	3
$K^- \rightarrow \pi^0 \mu^- \bar{\nu}_\mu$	2.6×10^{-7}	2
Total	1.6×10^{-5}	100

$\bar{\nu}_e$ flux		
Source	Integrated flux	Percent of total
$\pi^- \rightarrow \mu^- \bar{\nu}_\mu \rightarrow e^- \nu_\mu \bar{\nu}_e$	4.5×10^{-8}	54
$K^- \rightarrow \pi^0 e^- \bar{\nu}_e$	2.0×10^{-8}	24
$K_L^0 \rightarrow \pi^+ e^- \bar{\nu}_e$	1.5×10^{-8}	18
$\pi^- \rightarrow e^- \bar{\nu}_e$	1.9×10^{-9}	2
$K_S^0 \rightarrow \pi^- \pi^+ \rightarrow \mu^- \bar{\nu}_\mu \rightarrow\rightarrow e^- \nu_\mu \bar{\nu}_e$	1.6×10^{-9}	2
$K^- \rightarrow \pi^0 \mu^- \bar{\nu}_\mu \rightarrow e^- \nu_\mu \bar{\nu}_e$	6.6×10^{-10}	1
Total	8.3×10^{-8}	100

ν_μ flux		
Source	Integrated flux	Percent of total
$\pi^+ \rightarrow \mu^+ \nu_\mu$	1.1×10^{-6}	85
$K^+ \rightarrow \mu^+ \nu_\mu$	1.1×10^{-7}	9
$\pi^- \rightarrow \mu^- \bar{\nu}_\mu \rightarrow e^- \nu_\mu \bar{\nu}_e$	4.5×10^{-8}	4
$K_S^0 \rightarrow \pi^- \pi^+ \rightarrow \mu^+ \nu_\mu$	1.6×10^{-8}	1
$K_L^0 \rightarrow \pi^- \mu^+ \nu_\mu$	1.0×10^{-8}	1
Total	1.2×10^{-6}	100

ν_e flux		
Source	Integrated flux	Percent of total
$K_L^0 \rightarrow \pi^- e^+ \nu_e$	1.5×10^{-8}	54
$K^+ \rightarrow \pi^0 e^+ \nu_e$	1.1×10^{-8}	41
$\pi^+ \rightarrow \mu^+ \nu_\mu \rightarrow e^+ \bar{\nu}_\mu \nu_e$	1.2×10^{-9}	4
$K^+ \rightarrow \pi^0 \mu^+ \nu_\mu \rightarrow e^+ \bar{\nu}_\mu \nu_e$	1.6×10^{-10}	1
Total	2.7×10^{-8}	100.0

Table 2.6: Integrated flux of dominant decay modes and the total neutrino flux in $\bar{\nu}$−run. The flux is per proton on target per m^2.

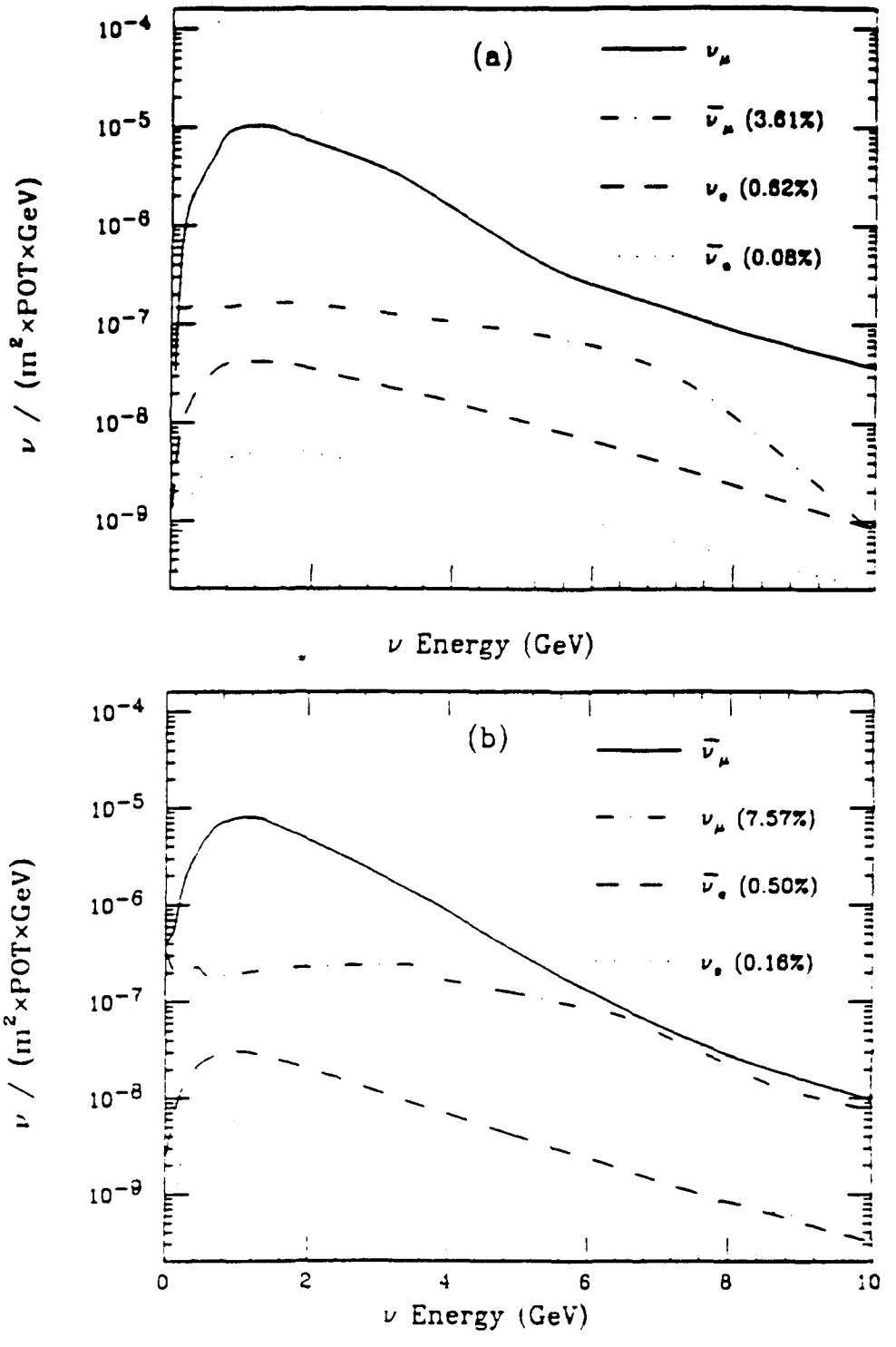

Figure 2.8: Total calculated spectra for ν_μ, ν_e, $\bar{\nu}_\mu$, and $\bar{\nu}_e$: (a) WBB $\nu-$Run (b) WBB $\bar{\nu}-$Run

secondary beam and of pions and kaons can be found in [24], and [31]. The total calculated neutrino spectra for ν_μ, ν_e, $\overline{\nu}_\mu$, and $\overline{\nu}_e$ are shown in Figure 2.8

2.1.3 Beam Monitoring

The beam was continuously monitored during the run. The proton beam intensity was measured by the UX716 current transformer and the integrated number of protons on target (POT) was 1.43×10^{19} for the neutrino run and 1.55×10^{19} for the antineutrino run. An extensive discussion of beam monitoring was presented in [23].

2.2 E776 Neutrino Detector

The BNL E776 experiment was originally designed to search for the neutrino oscillation ν_μ $(\overline{\nu}_\mu) \rightarrow \nu_e$ $(\overline{\nu}_e)$.

The neutrino is a weakly interacting particle with a very small interaction cross section. To make a statistically meaningful measurement in the neutrino oscillation search, the detector should satisfy the following two conditions. The first requirement is that the neutrino detector should be very massive to provide a reasonable interaction rate. The second requirement is that the detector should be able to tell electrons from muons, and measure physical parameters (like energy, momentum and direction cosines) very well, since they are the products of interactions of ν_μ and ν_e respectively.

The E776 detector, which is located 1 *km* away from the target, is made of two sections; a massive but finely segmented electromagnetic(EM)-calorimeter and a toroid spectrometer. At AGS beam energy, electrons develop showers in the calorimeter, but muons travel straight through without showering, and some of them enter the toroid. For high energy muons penetrating calorimeter, the toroid provides charge determination and additional momentum measurement. The details of the E776 neutrino detector are shown in Figure 2.9.

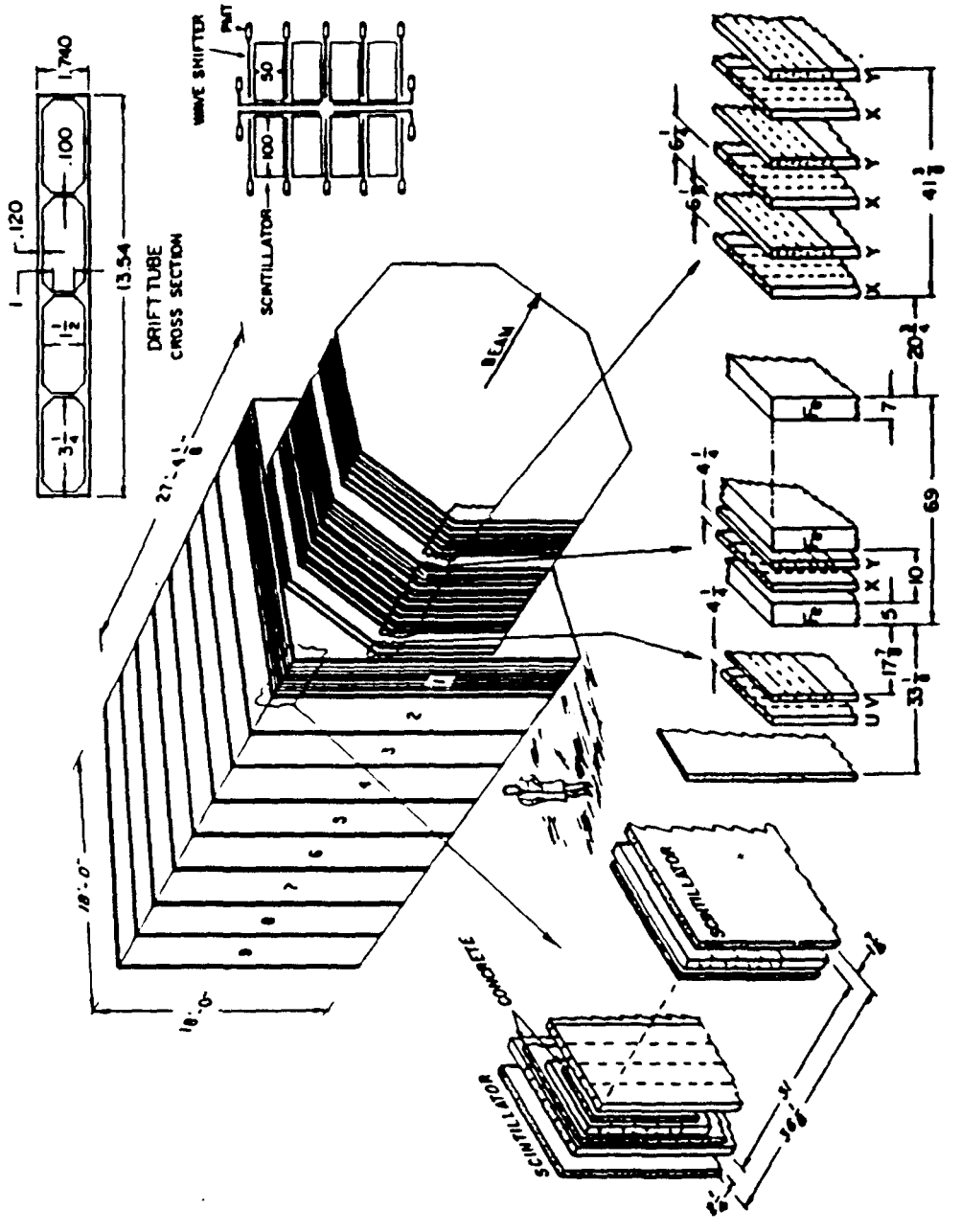

Figure 2.9: The E776 neutrino detector

2.2.1 Electromagnetic Calorimeter

The electromagnetic calorimeter was made of 90 planes of proportional drift tubes (PDT) with a 1″ thick concrete absorber slab inserted between the PDT planes. Every 10th plane of concrete was replaced with an acrylic scintillator counter plane, with approximately the same radiation length as the concrete slab, for event timing and cosmic ray triggering.

The overall dimensions of the calorimeter are 18′ × 18′ × 27′ 4″, and the total weight of about 225 metric tons. The physical properties of the components making up the calorimeter are listed in Table 2.7.

Component	Material	Z Average	A Average	Density (g/cm^3)	Mass per plane (kg)	Number of planes
Absorber	Concrete	10.7	21.5	2.31	1775	81
Drift cell	Aluminum	13	26.98	2.7	692	90
Scintillator jacket	Aluminum	13	26.98	2.7	1145	10
Scintillator	Acrylic	6	12	1.17	814	10

Table 2.7: Composition of EM calorimeter

Each PDT plane contained 64 wire cells. They were alternated in the X (horizontal) and the Y (vertical) directions (the Z direction is taken to be the same as beam

direction). Measurements of two independent X and Y views provided a stereo view of the events, which could later be reconstructed in 3-dimensional space.

Two shielding walls were placed upstream of the detector to remove any sources of beam related background. A 1.5 m thick concrete wall located 5 m upstream of the detector was installed to shield against neutrons which may cause background problem as well as against muons. The second shielding wall comprised of a 2″ lead (9.1 radiation lengths), was located right before the detector to remove any beam related high energy gamma rays by converting them into electromagnetic showers before reaching the calorimeter.

Proportional Drift Tubes (PDT)

Proportional Drift Tubes were chosen as the sampling device for the experiment. When a charged particle travels through a medium, it loses energy through the excitation and the ionization of the atoms in the medium. By applying an electric field in the medium, the ionized particles can be collected, and by measuring the total charge, the energy lost by the ionizing particle can be determined. The heavy positive ions drift slowly toward the cathode plane, while light electrons drift quickly towards the anode wire. The ionization process multiplies as it approaches the anode wire, and finally an "avalanche" occurs near the wire. The PDT's were operated in the proportional mode, where the signal is proportional to the energy deposited in the chamber.

The PDT chamber were constructed from an extruded aluminum box with a gold

plated tungsten wire running through the center. Each PDT plane consisted of 16 aluminum modules, each module containing 4 single wire chambers, making 64 wires altogether. The aluminum wall of the PDT chamber was grounded and the wire was held at $2.25kV$ where PDT's were at least 98 % efficient (Figure 2.10). A cross sectional view of one module is shown in Figure 2.11

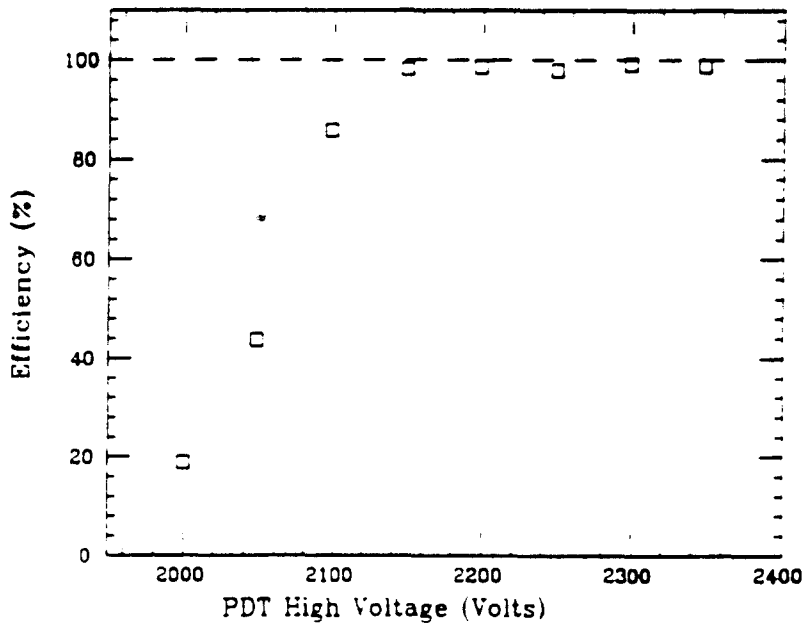

Figure 2.10: Efficiency of a PDT chamber with respect to applied high voltage

A gas mixture of 80 % Ar and 20 % C_2H_6 were used. The maximum drift time was about $2\mu s$, with a gain of 4×10^4. The drift times and distances are shown in Figure 2.12, while equipotential lines and drift time contours are shown in Figure 2.13 [32].

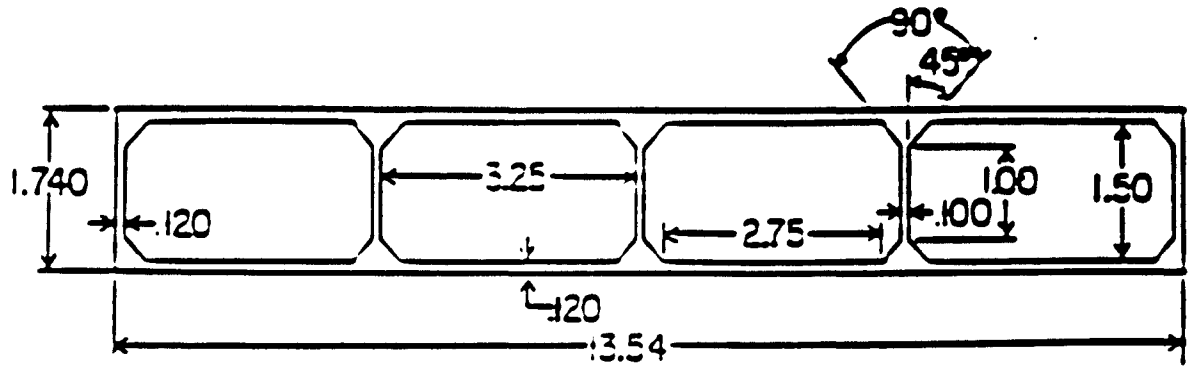

Figure 2.11: Cross sectional view of one PDT module. One PDT plane was made of 16 of these modules.

Concrete Absorber

Concrete was chosen as the absorber material for the neutrino detector after all the following requirements for the neutrino detector were considered.

1. **High density material:** To force the weakly interacting neutrinos to interact, a high density material, which has lots of target nucleons, is required.

2. **High Z material for shower development:** To generate rich electromagnetic showers, the radiation length of the material must be small. Since radiation length inversely proportional to the atomic number Z of the material, a high Z material is needed.

3. **Low Z material for good sampling:** To achieve good sampling, it's better to have low Z material so that between the sampling less shower development

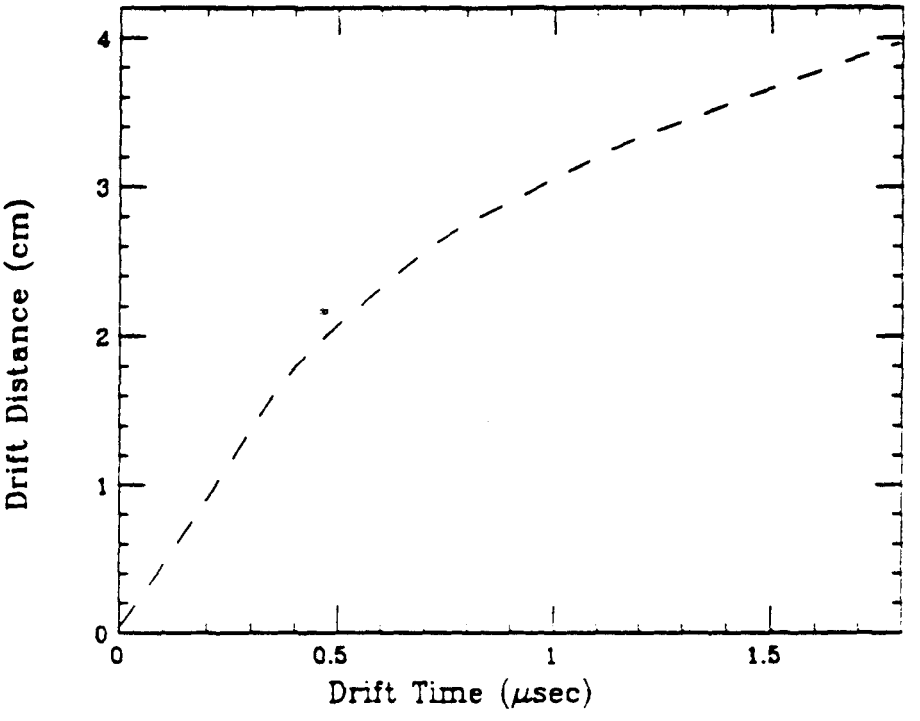

Figure 2.12: Calculated drift time and distance map of PDT.

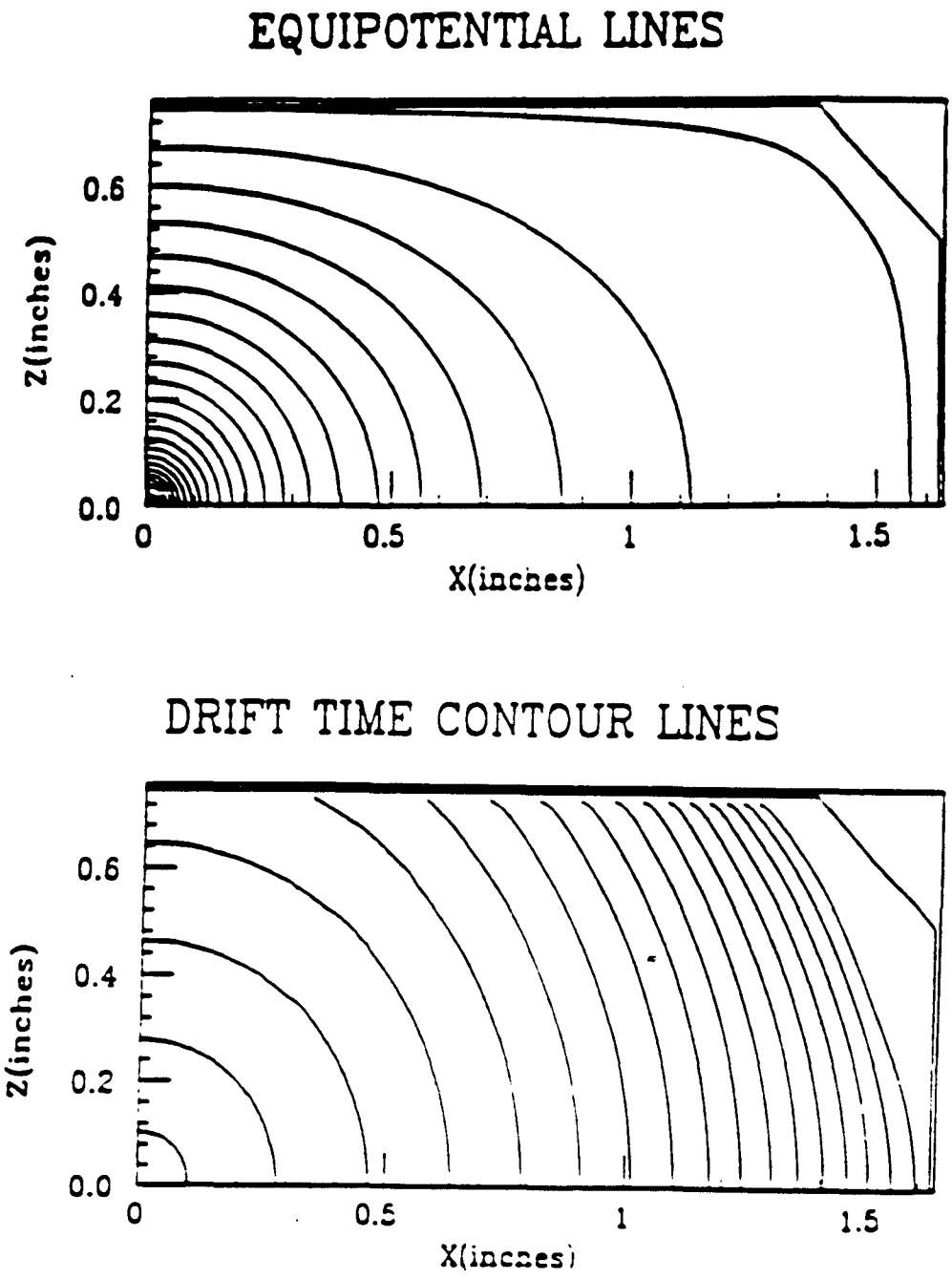

Figure 2.13: Calculated equipotential lines and equal drift time contours of PDT. Z is the beam direction, and X is either horizontal or vertical direction perpendicular to the beam direction

occurs.

4. **Cost of the material:** To be realistic, the cost of the material should be reasonable.

The composition of the concrete used as absorber is listed in Table 2.8. The concrete had an average Z of 10.7, with a density of $2.3 g/cm^3$.

Compound	Per cent	Z Average	A Average	Density (g/cm^3)
CaO	36.5	14.0	28.03	3.3
SiO_2	13.8	10.0	20.03	2.6
MgO	6.3	10.0	20.16	3.6
CO_2	27.1	7.3	14.67	1.6
other	16.3	10.0	20.0	2.3
Concrete Average		10.7	21.5	2.3

Table 2.8: Composition of concrete absorber

Each plane of drift tubes together with the absorber corresponds to 1/3 of a radiation length, 1/12 of an interaction length, and 14.5 MeV/plane energy loss due to dE/dX for a minimum ionizing particle.

Scintillation Counters

Every 10th plane of concrete absorber was replaced with a plane scintillation counters to measure event timing and provide a cosmic ray trigger. Each scintillation plane was built as two separate half-planes; each half plane containing four sheets of $100'' \times 50'' \times 1''$ acrylic scintillator. 14 BBQ waveshifter bars surrounded the edges of the scintillating planes and were connected to RCA 8575 photomultiplier tubes (PMT). A scintillator plane is shown in Figure 2.14

Cosmic rays were used to study the performance of the scintillator. For a minimum ionizing particle, each PMT sees 3 to 8 photoelectrons. The average efficiency for all phototubes is 94.4 % [32].

2.2.2 Toroid Spectrometer

The toroid spectrometer was designed to measure muon momentum and charge in conjunction with the measurement made in the calorimeter.

Five $5'' - 5'' - 5'' - 7'' - 7''$ thick octagonal magnetized Fe-plates with 2 X and Y view PDT planes between the toroidal plates and 3 pairs of PDT planes at the end of the toroid make up the toroid spectrometer for E776. Each toroidal plane was magnetized by a 4 turn conductor made of insulated hollow copper pipe which passed through a $8'' \times 8''$ central hole and carried a current of 15 kA. The nominal B-field was 18 kG dropping to 15.5 kG at the edge. A description of the B-field measurement can be found in reference [33]. For the neutrino run, the toroid magnetic field was

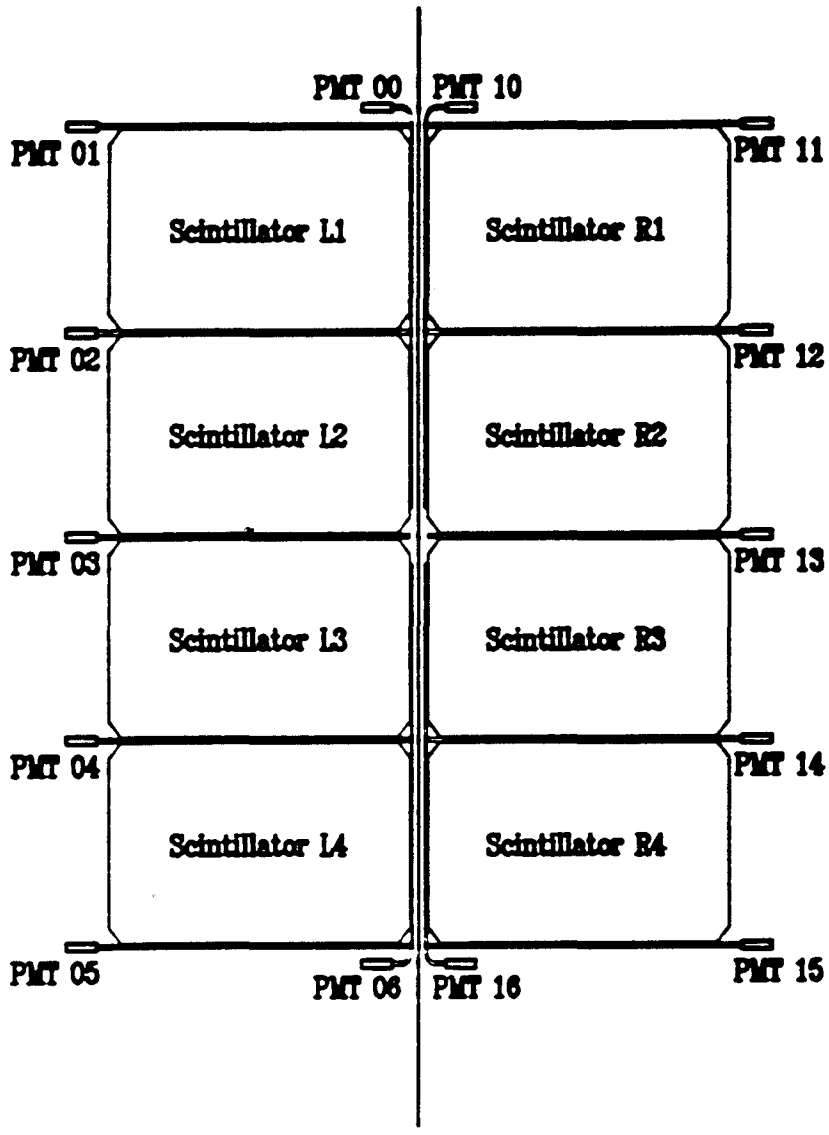

Figure 2.14: A Scintillator plane

set to focus μ^-, and for the antineutrino run, it was set to focus μ^+.

To resolve the ambiguity of tracks entering the toroid resulting from the independent measurement of the X and Y views, UV-planes, rotated at 45° with respect to the xy-planes, were inserted between the calorimeter and the toroid.

2.2.3 Data Readout

There are three major sources of signals from the detector. They are;

- **PDT's in the calorimeter :**

  Signals, read off from the wire, were amplified in preamps, digitized by a 6 bit fast-sampling Flash ADC (FADC: Flash Analog-to-Digital Converter) every 22.4 ns, and recorded in a 256 word deep static flash memory chip. In this way the memory chip always kept the data for the past $256 \times 22.4ns$. Sampling by FADC allowed to the shape of the pulse to be fully reconstructed, providing pulse height and pulse area information.

- **Scintillator PMT's in the calorimeter :**

  Signals from the PMT were split with half of the signal being discriminated. The time that the signal crossed threshold was recorded by a 5.6 ns TDC (Time-to-Digital Converter). The second half of the signal was stretched, then this stretched signal was recorded by the FADC system.

- **PDT's in the toroid spectrometer:** Signals from the PDT planes in the toroid, were recorded by 22.4 ns sampling TDC's, not by FADC's as were the

case of PDT's in the calorimeter.

All the circuit diagrams and engineering details of electronics can be found in [34]. The overall diagram of the data acquisition system is shown Figure 2.15

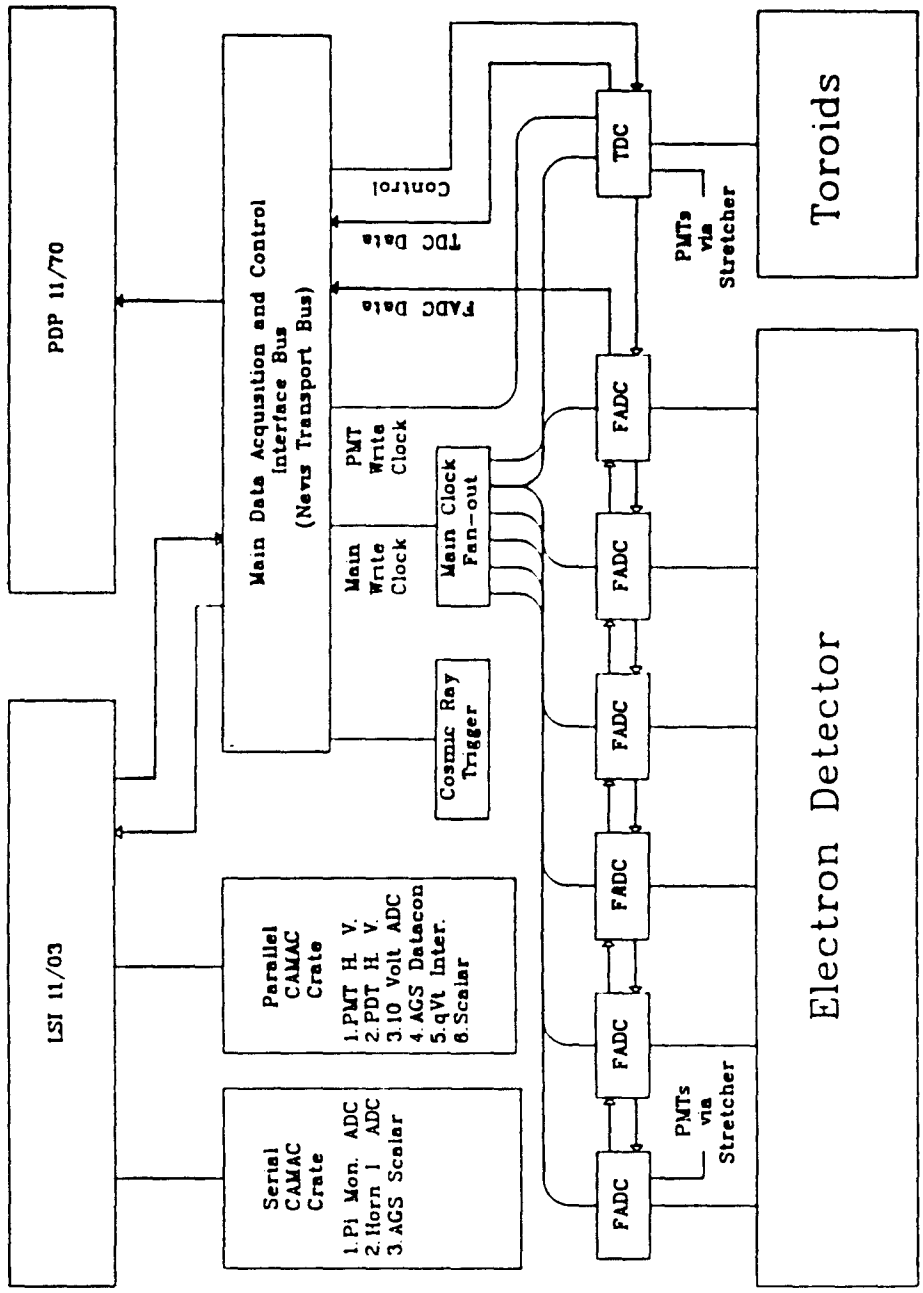

Figure 2.15: Schematic diagram of the data acquisition system

Chapter 3

PHENOMENOLOGY OF NEUTRINO INTERACTIONS AND MONTE CARLO SIMULATION

Neutrinos, which interact with matter only weakly, are very useful for probing the weak interaction. Weak interactions, in general, can be categorized as *charged* and *neutral* according to whether they occur by $W^{\pm}$ exchange or Z exchange. They are also classified as *leptonic*, *semileptonic*, or *nonleptonic* depending on whether the final state contains only leptons, leptons and hadrons, or no leptons. Among the many types of neutrino interactions, particular emphasis was given to neutrino-nucleon interactions in the E776 experiment, since all the neutrino events in the experiment are from neutrino-nucleon interactions.

Combining theoretical knowledge of these interactions with an experimental parameterization of effects inside nuclear matter, gives the ability to predict the interaction rate for various channels and their behavior inside the detector. This was done by

an extensive Monte Carlo simulation, exclusively developed for the E776 experiment, and described in this chapter.

3.1 Neutrino-Nucleon Interactions

The neutrino-nucleon interaction can be either a charged current or a neutral current semileptonic process:

Charged-current interactions:

- Quasi-Elastic Scattering (QE)
- Charged-Current (semi-inclusive) Single Pion Production (CCSP)
- Charged-Current (inclusive) Deep-Inelastic Scattering (CCDIS)

Neutral-current interactions:

- Elastic Scattering (EL)
- Neutral-Current (semi-inclusive) Single Pion Production (NCSP)
- Neutral-Current (inclusive) Deep-Inelastic Scattering (NCDIS)

Possible neutrino interactions in each category are summarized in Table 3.1.

		ν *Interactions*	$\overline{\nu}$ *Interactions*
CC	*Quasi – Elastic*	$\nu_\mu n \longrightarrow \mu^- p$	$\overline{\nu}_\mu p \longrightarrow \mu^+ n$
NC	*Elastic*	$\nu_\mu n \longrightarrow \nu_\mu n$ $\nu_\mu p \longrightarrow \nu_\mu p$	$\overline{\nu}_\mu n \longrightarrow \overline{\nu}_\mu n$ $\overline{\nu}_\mu p \longrightarrow \overline{\nu}_\mu p$
CC	*Single – Pion*	$\nu_\mu p \longrightarrow \mu^- p\pi^+$ $\nu_\mu n \longrightarrow \mu^- p\pi^0$ $\nu_\mu n \longrightarrow \mu^- n\pi^+$	$\overline{\nu}_\mu n \longrightarrow \mu^+ n\pi^-$ $\overline{\nu}_\mu p \longrightarrow \mu^+ p\pi^0$ $\overline{\nu}_\mu p \longrightarrow \mu^+ p\pi^-$
NC	*Single – Pion*	$\nu_\mu n \longrightarrow \nu_\mu n\pi^0$ $\nu_\mu p \longrightarrow \nu_\mu p\pi^0$ $\nu_\mu n \longrightarrow \nu_\mu p\pi^-$ $\nu_\mu p \longrightarrow \nu_\mu n\pi^+$	$\overline{\nu}_\mu n \longrightarrow \overline{\nu}_\mu n\pi^0$ $\overline{\nu}_\mu p \longrightarrow \overline{\nu}_\mu p\pi^0$ $\overline{\nu}_\mu n \longrightarrow \overline{\nu}_\mu p\pi^-$ $\overline{\nu}_\mu p \longrightarrow \overline{\nu}_\mu n\pi^+$
CC	*Deep – Inelastic*	$\nu_\mu N \longrightarrow \mu^- X$	$\overline{\nu}_\mu N \longrightarrow \mu^+ X$
NC	*Deep – Inelastic*	$\nu_\mu N \longrightarrow \nu_\mu X$	$\overline{\nu}_\mu N \longrightarrow \overline{\nu}_\mu X$

Table 3.1: Charm-Nonproducing Neutrino-Nucleon Interactions: (ν_μ, μ^- can be replaced by ν_e, e^-, and ν_τ, τ^-). X is an excited hadronic matter.

All the above interactions were written for ν_μ flavor only, for the sake of convenience. Interactions for the other lepton flavors are given by changing the neutrino and the corresponding lepton flavor in Table 3.1. The total charm-nonproducing neutrino-nucleon interaction cross sections can be obtained by adding the cross sections of all the channels listed.

In high energy νN collisions, opposite sign dilepton events can be observed through the production of a heavy charmed quark via charged current interactions and its subsequent decay to a lepton opposite in sign to the lepton from the lepton vertex.

A neutrino induced opposite sign dimuon event is the signal sought for in this analysis. We separated *charm – producing* neutrino-nucleon interactions from conventional *charm – nonproducing* neutrino-nucleon interactions for the sake of presentation.

Even in the E776 neutrino beam energy region, charm-producing neutrino interactions can occur. However, available neutrino beam energy and flux in E776 were not enough for the production of charmed quark pairs, the *charm – producing* neutrino-nucleon interactions presented here always mean *single charmed quark production.*

Charm producing neutrino interactions can be categorized as follows.

- Quasi-Elastic Charmed Baryon Production
- Charged-Current Single Pion Charmed Baryon Production
- Charged-Current Deep-inelastic Charmed Meson production

Possible interaction channels for charm-producing channels are listed in Table 3.2.

There are several important features to note about charm producing neutrino-nucleon interactions:

- There are no neutral current single charm-producing weak interactions as there exist no neutral strangeness-changing weak interactions.

		ν *Interactions*	$\overline{\nu}$ *Interactions*
CC	$Quasi-Elastic$	$\nu_\mu n \longrightarrow \mu^- \Lambda_c^+$ $\nu_\mu p \longrightarrow \mu^- \Sigma_c^{++}$ $\nu_\mu n \longrightarrow \mu^- \Sigma_c^+$	$forbidden$
NC	$Quasi-Elastic$	$forbidden$	$forbidden$
CC	$Single-Pion$	$\nu_\mu p \longrightarrow \mu^- \Sigma_c^{*++}$ $\nu_\mu n \longrightarrow \mu^- \Sigma_c^{*+}$	$forbidden$
NC	$Single-Pion$	$forbidden$	$forbidden$
CC	$Deep-Inelastic$	$\nu_\mu N \longrightarrow \mu^- cX$	$\overline{\nu}_\mu N \longrightarrow \mu^+ \overline{c} X$
NC	$Deep-Inelastic$	$forbidden$	$forbidden$

Table 3.2: Charm producing Neutrino-Nucleon Interactions. X is an excited state of hadronic matter which doesn't carry charm quantum number.

- There are no exclusive antineutrino-induced charm-producing reactions.

Since there are no exclusive antineutrino induced charm producing reactions, we should not have dimuon events from antineutrino data.

Since we have both neutrino and antineutrino data, we have one more handle to understand and check the validity of the results on dimuon events induced from neutrino, or antineutrino produced charmed particles. This will be further explained later in the QE charmed baryon production cross section calculation section.

In the search for the opposite sign dimuon events, all these channels are important to understand the signal (charm induced opposite sign dimuon events), and possible backgrounds (mostly from conventional charm-nonproducing neutrino interactions). Therefore, all the possible interactions were properly parameterized in the E776 neutrino beam energy region and included in the Monte Carlo event generation and simulation.

The charged-current interaction always produces a muon from the lepton vertex. So if a high energy hadron fakes a second muon, these charged current interactions become a major source of background for dimuon events.

Since neutral current interactions do not produce primary muons from the lepton vertex, it is very unlikely to have two hadrons faking muons in the same event, so neutral currents are rarely a source of background. Therefore, special emphasis is given to charged-current interactions in this analysis, and are described in detail in the following sections.

3.2 Charm-Nonproducing Charged-Current Neutrino-Nucleon Interactions

3.2.1 Quasi-Elastic Scattering

Quasi-elastic(QE) scattering, charged-current neutrino-nucleon elastic scattering (Figure 3.1), is the simplest, and by far the best understood of the various $\nu - N$ interactions. The QE cross section rises steadily from the threshold energy up to about $E_\nu = 1$ GeV, then remains constant independent of the neutrino energy. As a result, it plays a rather important role around 1 GeV where the deep-inelastic cross section is relatively small compared to the QE cross section. In the E776 experiment, the neutrino beam energy peaks around $1 \sim 2$ GeV, so the QE process is the dominant process.

The differential cross section for the QE process averaged over nucleon spins [35] is,

$$\frac{d\sigma}{dQ^2}\left(\begin{array}{c}\nu n \to l^- p \\ \bar{\nu} p \to l^+ n\end{array}\right) = \frac{M^2 G^2 cos^2\theta_c}{8\pi E_\nu^2}[A(q^2) \mp B(q^2)\frac{(s-u)}{M^2} + \frac{C(q^2)(s-u)^2}{M^4}] \quad (3.1)$$

where M is hadron (p, or n) mass, m is lepton mass, E_ν is neutrino lab energy, Q^2 is the four-momentum transfer between the lepton vertex and the hadron vertex, and the invariant quantity $s - u$ (s is the center of mass energy squared) is defined as the following.

$$Q^2 = -q^2 > 0$$

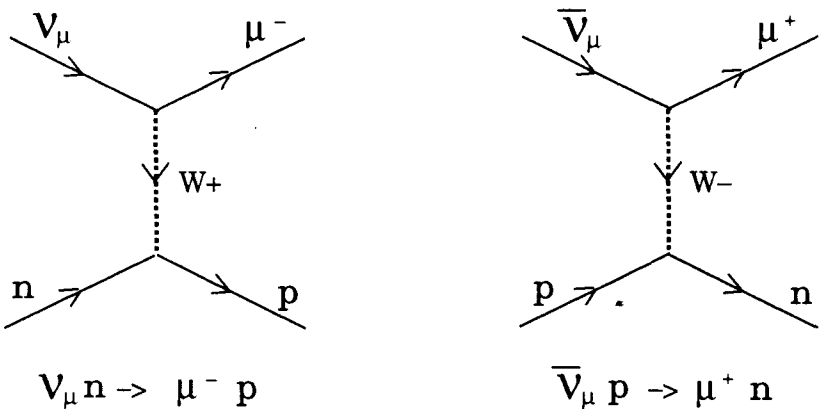

Figure 3.1: Feynman diagram for QE scattering

$$s - u = 4ME_\nu + q^2 - m^2$$

Explicitly $A(q^2)$, $B(q^2)$, and $C(q^2)$ are given in terms of form factors,

$$\begin{aligned}
A(q^2) &= \frac{(m^2-q^2)}{4M^2}[(4-\frac{q^2}{M^2})\mid F_A\mid^2 - (4+\frac{q^2}{M^2})\mid F_V^1\mid^2 - \frac{q^2}{M^2})\mid \xi F_V^2\mid^2 \\
&\quad -\frac{4q^2F_V^1\xi F_V^2}{M^2} - \frac{m^2}{M^2}(\mid F_V^1+\xi F_V^2\mid^2 + \mid F_A\mid^2)] \\
B(q^2) &= -\frac{q^2}{M^2}F_A(F_V^1+\xi F_V^2) \\
C(q^2) &= \frac{1}{4}(\mid F_A\mid^2 + \mid F_V^1\mid^2 - \frac{q^2}{M^2}\mid \frac{\xi F_V^2}{2}\mid^2)
\end{aligned}$$

Assumptions, which restrict the form factors, are as follows:

- T invariance $\rightarrow$ All form factors are real.
- Charge symmetry
- No second-class currents
- Conserved Vector Current hypothesis (CVC)

The form factors, F_V^1 (Dirac electromagnetic isovector form factor), and F_V^2 (Pauli electromagnetic isovector form factor) have the form

$$\begin{aligned}
F_V^1(q^2) &= F_1^p(q^2) - F_1^n(q^2) \\
F_V^2(q^2) &= \frac{\mu_p F_2^p(q^2) - \mu_n F_1^n(q^2)}{\mu_p - \mu_n} \\
\xi &= \mu_p - \mu_n
\end{aligned} \tag{3.2}$$

In terms of Sachs form factors, they are,

$$\begin{aligned}
F_V^1(q^2) &= (1-\tfrac{q^2}{4M^2})^{-1}[G_E^V(q^2) - \tfrac{q^2}{4M^2}G_M^V(q^2)] \\
\xi F_V^2(q^2) &= (1-\tfrac{q^2}{4M^2})^{-1}[G_M^V(q^2) - G_E^V(q^2)]
\end{aligned} \tag{3.3}$$

where,

$$\begin{aligned} G_E^V(q^2) &= \frac{1}{(1-\frac{q^2}{M_V^2})^2} \\ G_M^V(q^2) &= \frac{1+\mu_p-\mu_n}{(1-\frac{q^2}{M_V^2})^2} \end{aligned} \tag{3.4}$$

The axial-vector form factor, $F_A(q^2)$, is

$$F_A(q^2) = F_A(0)(1-\frac{q^2}{M_A^2})^{-2} \tag{3.5}$$

Using experimentally determined parameters,

$$\begin{aligned} M_V &= 0.84 \quad GeV \\ M_A &= 1.098 \quad GeV \\ cos\theta_c &= 0.9737 \\ \xi &= 3.71 \\ F_A(0) &= -1.23 \end{aligned} \tag{3.6}$$

and the known lepton masses, the QE cross sections for all 3 flavors (e, μ, τ) were calculated and are shown in Figure 3.2.

As one can see from the QE cross section graph, around $1 \sim 2$ GeV where our neutrino beam energy peaks, the QE cross section of neutrino (ν_μ and ν_e) is twice as large as that of antineutrino ($\overline{\nu}_\mu$ and $\overline{\nu}_e$) cross section.

One kinematical aspect where the neutrino interaction is different from antineutrino interaction is the angular distribution, $d\sigma/dcos\theta^*$. In the neutrino case, the total spin of the $\nu N-$system is zero in the center of mass frame, which results in no angular dependence in the cross section formula. By contrast, the total spin of $\overline{\nu}N-$system is one, so the differential cross section has a corresponding angular de-

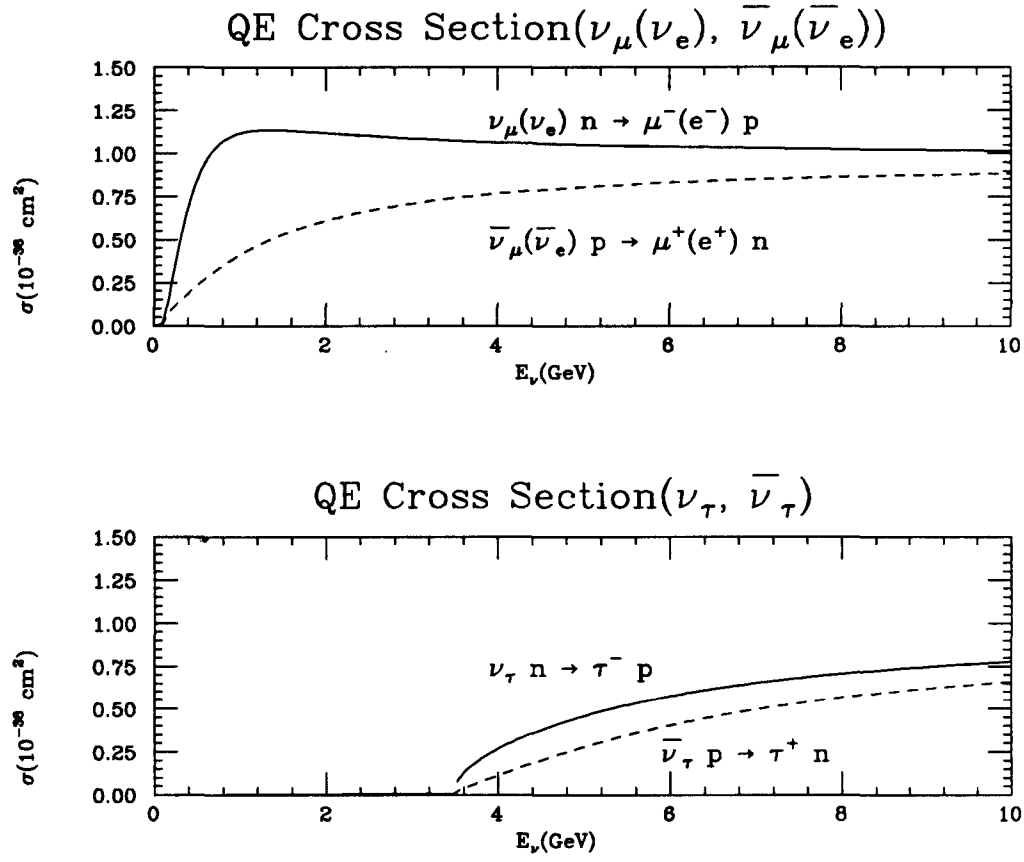

Figure 3.2: QE Cross Sections

pendence, proportional to $\{(1 + cos\theta^*)/2\}^2$, and this makes the outgoing μ^+ more focused to forward direction.

3.2.2 Single Pion Production

Single pion production by neutrinos, the exclusive process of the neutrino-nucleon scattering in which a pion-nucleon final state is observed, can be considered to be mediated by all interfering resonances with $\pi N-$ invariant mass below 2 GeV. This process can occur through a large variety of channels in both neutrino and antineutrino charged-current and neutral-current interactions as explicitly written in Table 3.1.

The simplest way of understanding this process is based on the idea that a nucleon can be treated as a bound state of 3 constituent quarks whose excitations are the resonances seen in the pion-nucleon system. Several models have been proposed to explain single pion production in the resonance region, and have been compared to existing experimental data, with considerable success to photoproduction of nucleon resonances. Among those, we have used the model developed by Rein and Sehgal [36], [37] for all channels of single pion production in the calculation of E776 Monte Carlo event generator.

We can get some qualitative idea of how big these cross sections should be by considering the following process. Charged current neutrino excitation of a single

nonstrange nucleon resonance can be written,

$$\nu_\mu + N \longrightarrow \mu^- + N^* \tag{3.7}$$

where N^* denotes the nucleon resonance.

The cross section can be estimated the same way as the QE cross section, but with a N^* mass, which is 1.232 GeV. The results are shown in Figure 3.3. To produce one more pion, the threshold energy must be higher than that of QE process, but overall the charged-current single pion production cross section is comparable to that of QE scattering. The cross sections for ν_e and ν_μ which were used in the E776 Monte Carlo generator are shown in Figure 3.4. The cross sections were calculated based on the model by Rein and Sehgal, and the original programming code developed by them was carefully combined into our Monte Carlo event generator.

In the Rein and Sehgal single pion production model, all the leptons are treated as massless, so it can not be applied to the massive τ lepton. Even though no established picture exists for tau neutrino single pion production, an estimate of the cross section can still be made using the QE cross section and the results are shown in Figure 3.3. Since the E776 neutrino beam is mainly ν_μ with about 1 % ν_e contamination, and ν_τ is not believed to be in the neutrino beam, no effort has been made to incorporate ν_τ single pion production in the Monte Carlo.

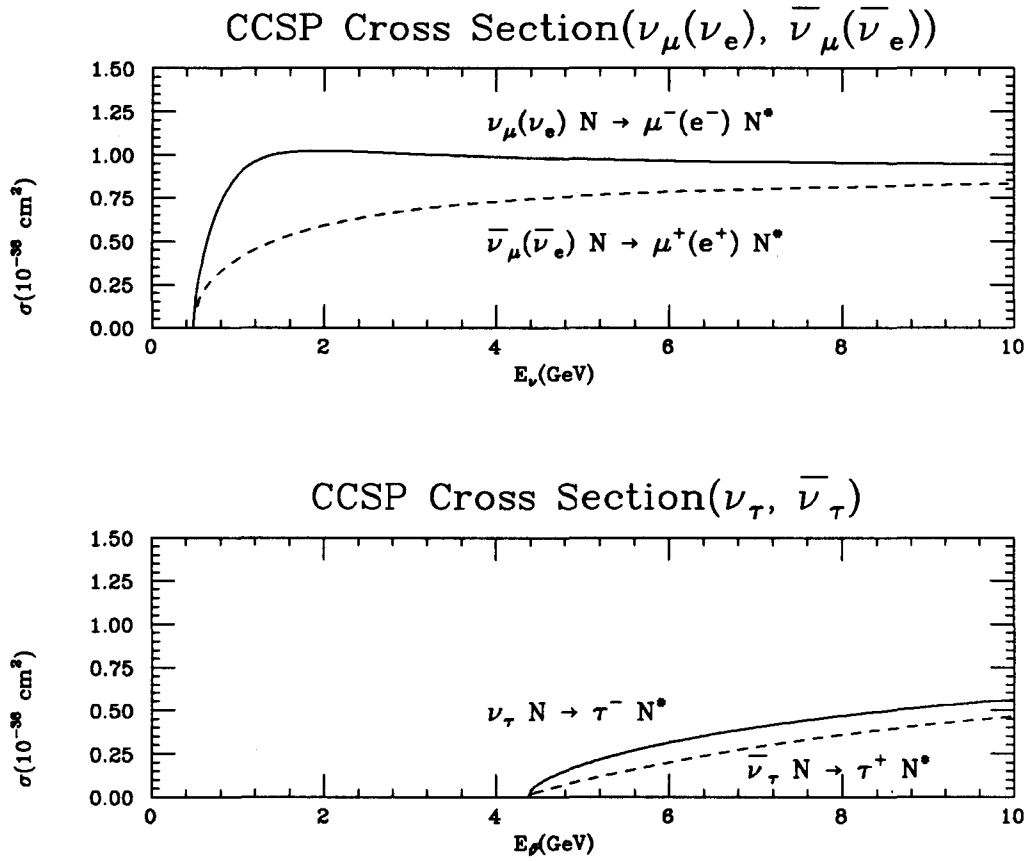

Figure 3.3: Charged-Current Single Pion Production Cross Sections assuming QE cross sections with final state nucleon to be N^*

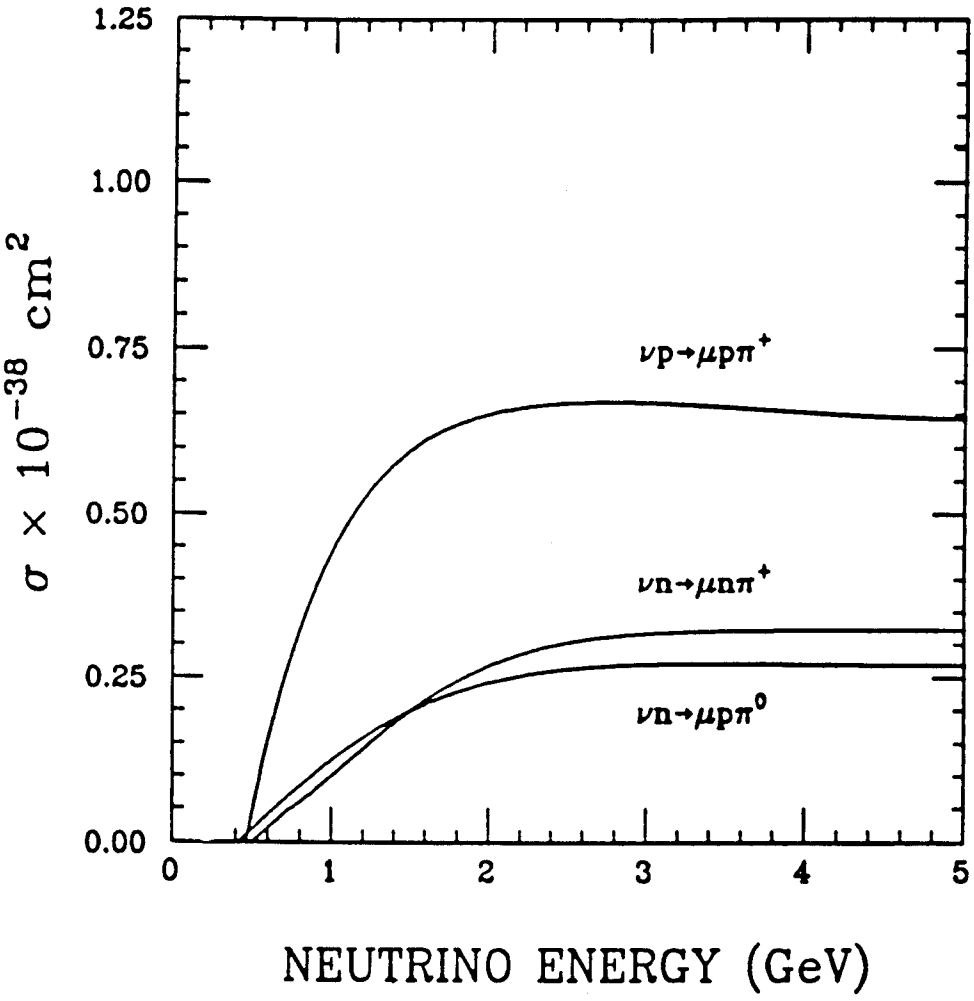

Figure 3.4: Charged-Current Single Pion Production Cross Sections based on model by Rein and Sehgal

3.2.3 Deep-Inelastic Scattering

The deep-inelastic scattering by neutrinos has contributed significantly to the understanding of the compositeness of hadrons, and to testing fundamental parameters in QCD (quantum chromodynamics). Since high energy neutrinos interact only weakly, they can penetrate deep into a nucleon and collide with individual constituents of the nucleon revealing valuable information about the structure of matter inside the nucleon.

The Feynman diagram for charged-current deep-inelastic scattering is shown in Figure 3.5. The notation used is,

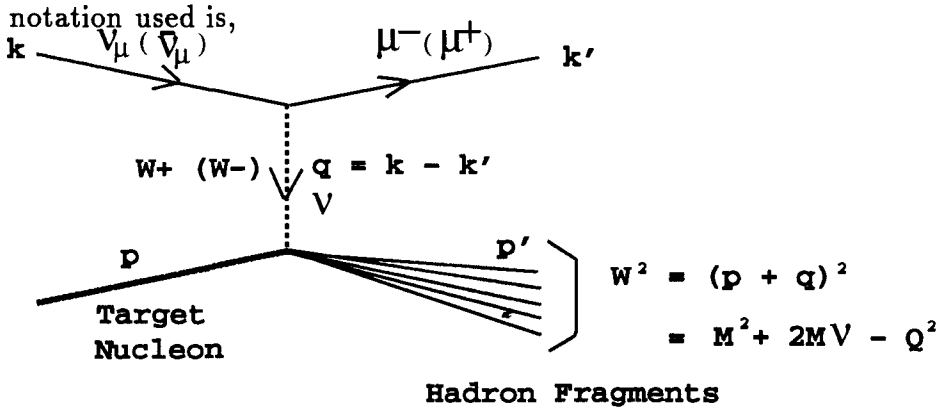

Figure 3.5: Feynman diagram for Charged-Current Deep-Inelastic Scattering

k : Four-momentum of incoming neutrino

k' : Four-momentum of outgoing muon

p : Four-momentum of target nucleon

p' : Four-momentum of X(ensemble of hadronic fragments)

E : Neutrino energy in lab frame(E_ν)

M : Mass of the target nucleon

Q^2 : The square of the four-momentum transfer between
the lepton vertex and the hadron vertex
(or, of the exchanged virtual boson)
$Q^2 = -q^2 > 0$

W^2 : The square of the invariant mass of highly
excited hadronic matter
$W^2 = p'^2 = (p+q)^2 = M^2 + 2M\nu - Q^2$

ν : Energy transfer from incoming lepton to the target
in the Lab frame
$\nu = p \cdot q/M = E_\nu - E_\mu$

To describe deep-inelastic scattering, the following additional parameters are required.

s : The square of the center-of-mass energy

$$s = (p + k)^2 = 2ME_\nu + M^2$$

x : The Bjorken scaling variable (x_{BJ})

$$x = \frac{-q^2}{2p \cdot q} = \frac{Q^2}{2M\nu}$$

y : Fraction of energy lost by the neutrino in the lab frame

$$y = \frac{p \cdot q}{p \cdot k} = \frac{\nu}{E_\nu}$$

The dimensionless scaling variables, x and y, provide an intuitive picture of the scattering between lepton and parton. The variable, x, is often interpreted as the fraction of momentum carried by the struck point-like parton. Then the definition of x is just a condition for elastic scattering from a parton with longitudinal momentum xp in the infinite momentum frame [38]. To see this, ignoring the parton mass and transverse momentum as relatively small, the elastic scattering condition is,

$$\begin{aligned} (xp + q)^2 &= (xp)^2 \\ x^2p^2 + 2xp \cdot q + q^2 &= x^2p^2 \\ x = \frac{Q^2}{2p \cdot q} &= \frac{Q^2}{2M\nu} \end{aligned}$$

The variable, y, is directly related to the center-of-mass scattering angle, θ^*. The relation is shown in detail when all the leptons and partons can be treated as massless in Figure 3.6 [39].

The differential cross sections for charged current deep-inelastic scattering can be written in terms of the scaling variables x, y, and structure functions with explicit

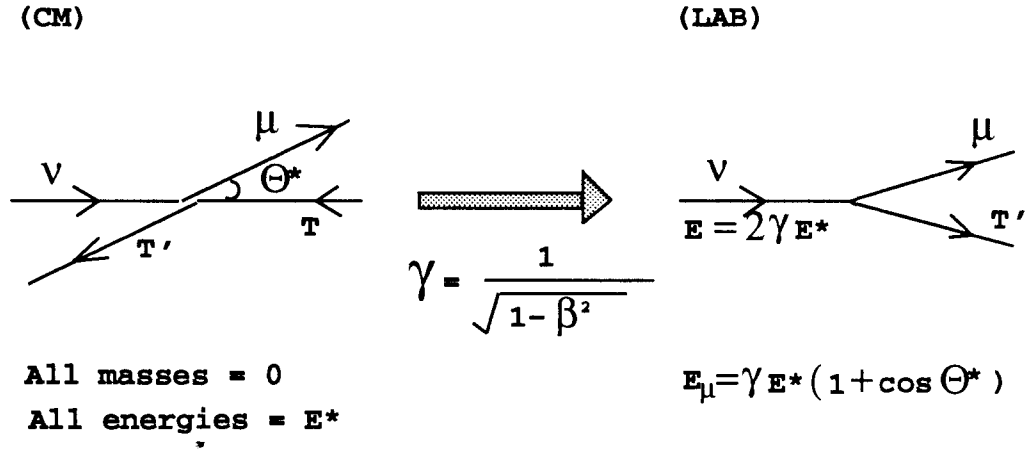

Figure 3.6: Scaling variable, y: the relation to the center-of-mass scattering angle θ^*.

lepton mass.

$$\begin{aligned}\frac{d^2\sigma^{\nu,\bar{\nu}}}{dxdy} = \; & \frac{G^2ME}{\pi}\{(xy+\frac{m^2}{2ME})yF_1+[(1-y)-(\frac{M}{2E}xy+\frac{m^2}{4E^2})]F_2 \\ & \mp[xy(1-\tfrac{1}{2}y)-\frac{m^2}{4ME}y]F_3+\frac{m^2}{M^2}[(\frac{M}{2E}xy+\frac{m^2}{4E^2})F_4-\frac{M}{2E}F_5]\}\end{aligned} \tag{3.8}$$

The kinematical limit on x and y are given by

$$\begin{aligned}\tfrac{m^2}{2M(E-M)} \; \leq x \leq \; 1 \\ A-B \; \leq y \leq \; A+B\end{aligned} \tag{3.9}$$

where

$$\begin{aligned}A \; &= \tfrac{1}{2}(1-\tfrac{m^2}{2MEx}-\tfrac{m^2}{2E^2})/(1+x\tfrac{M}{2E}) \\ B \; &= \tfrac{1}{2}\{(1-\tfrac{m^2}{2MEx})^2-\tfrac{m^2}{E^2}\}^{1/2}/(1+x\tfrac{M}{2E})\end{aligned} \tag{3.10}$$

For neutrinos interacting with spin 1/2 partons within the nucleons, the following assumptions for the structure functions can be made. (All the following assumptions about structure functions and quark distribution functions were suggested by Carl H. Albright by private communication.)

$$\begin{aligned} F_2(x,Q^2) &= 2xF_1(x,Q^2) = xF_5(x,Q^2) \\ F_4(x,Q^2) &= 0 \end{aligned} \tag{3.11}$$

where the first relation is just the Callen-Gross relation and the others follow from the positivity conditions. In the Bjorken limit of $Q^2 \to \infty$ with fixed x, the structure functions are functions of x only. The following expressions for an isoscalar target were used.

$$\begin{aligned} F_2^{\nu N} &= x(u+d+s) + x(\bar{u}+\bar{d}+\bar{s}) \\ -xF_3^{\nu N} &= x(u+d) + x(s+\bar{s}) - x(\bar{u}+\bar{d}) \\ &= F_2^{\nu N} - 2x(\bar{u}+\bar{d}) \\ F_2^{\bar{\nu}N} &= F_2^{\nu N} \\ -xF_3^{\bar{\nu}N} &= x(u+d) - x(\bar{u}+\bar{d}+s+\bar{s}) \\ &= F_2^{\nu N} - 2x(\bar{u}+\bar{d}+s+\bar{s}) \end{aligned} \tag{3.12}$$

For quark distribution functions, we have used the results from the CCFR group [40] which were extracted from the E616 charged current data. The particular parameterization quoted in [40] for the quark distribution functions are as follows,

$$\begin{aligned} xu_{proton}^{val}(x,Q^2) &= \{1 + (g - h\sqrt{x})log_{10}(\tfrac{Q^2}{10})\}ax^b(1-x)^c \\ xd_{proton}^{val}(x,Q^2) &= \eta\{1 + (g - h\sqrt{x})log_{10}(\tfrac{Q^2}{10})\}ax^b(1-x)^{c+1} \end{aligned} \tag{3.13}$$

Where η is a constant obtained from requiring that there be twice as many u quarks as d quarks in a proton:

$$2\eta = \frac{\frac{\Gamma(b)\Gamma(c+1)}{\Gamma(b+c+1)}(1 + g\ \log_{10}(\frac{Q^2}{10})) - \frac{\Gamma(b+\frac{1}{2})\Gamma(c+1)}{\Gamma(b+c+\frac{3}{2})} h\ \log_{10}(\frac{Q^2}{10})}{\frac{\Gamma(b)\Gamma(c+2)}{\Gamma(b+c+2)}(1 + g\ \log_{10}(\frac{Q^2}{10})) - \frac{\Gamma(b+\frac{1}{2})\Gamma(c+2)}{\Gamma(b+c+\frac{5}{2})} h\ \log_{10}(\frac{Q^2}{10})} \tag{3.14}$$

The quark-antiquark sea distribution $S_{nucleon}(x, Q^2)$ as a whole is given by

$$\begin{aligned} xS_{nucleon}(x, Q^2) = \ & \{1 + (g - h\sqrt{x})log_{10}(\tfrac{Q^2}{10})\} \\ & \cdot\{(1 + ex)(1 - x)^f - xu^{val}_{proton}(x, Q^2) - xd^{val}_{proton}(x, Q^2)\} \end{aligned} \tag{3.15}$$

where the values for the constants a - h are,

$$\text{a} = 2.3691$$

$$\text{b} = 0.5348$$

$$\text{c} = 2.5473$$

$$\text{d} = 1.6489$$

$$\text{e} = 0.7607$$

$$\text{f} = 2.5761$$

$$\text{g} = 0.3324$$

$$\text{h} = 0.9512$$

To get the actual quark distribution functions, one must take into account that the target is non-isoscalar, i.e. the number of protons and the number of neutrons are

not the same. The following is to take the non-isoscalar target effect into the quark distribution function.

The neutron excess fraction, f, can be defined as

$$f \equiv \frac{N-Z}{A} \tag{3.16}$$

where N is the number of neutrons, Z is the number of protons, and $A = N + Z$. For an isoscalar target, $f = 0$.

Noting that neutron= (udd) and proton= (uud), we have

$$u^{val}_{proton}(x,Q^2) = u^{val}_{neutron}(x,Q^2) \qquad d^{val}_{proton}(x,Q^2) = u^{val}_{neutron}(x,Q^2) \tag{3.17}$$

The average valance quark distributions in a nucleon expressed by proton quark distribution functions are:

$$\begin{aligned} d^{val}_{nucleon}(x,Q^2) &= \tfrac{1}{A}\{N d^{val}_{neutron}(x,Q^2) + Z d^{val}_{proton}(x,Q^2)\} \\ &= \tfrac{1}{A}\{N u^{val}_{proton}(x,Q^2) + Z d^{val}_{proton}(x,Q^2)\} \\ &= \tfrac{1}{2}\{(1+f) u^{val}_{proton}(x,Q^2) + (1-f) d^{val}_{proton}(x,Q^2)\} \end{aligned} \tag{3.18}$$

$$\begin{aligned} u^{val}_{nucleon}(x,Q^2) &= \tfrac{1}{A}\{N u^{val}_{neutron}(x,Q^2) + Z u^{val}_{proton}(x,Q^2)\} \\ &= \tfrac{1}{A}\{N d^{val}_{proton}(x,Q^2) + Z u^{val}_{proton}(x,Q^2)\} \\ &= \tfrac{1}{2}\{(1+f) d^{val}_{proton}(x,Q^2) + (1-f) u^{val}_{proton}(x,Q^2)\} \end{aligned}$$

Assuming that the composition of the quark-antiquark sea is the same for neutrons

and protons, then

$$\begin{aligned} u^{sea} &= \overline{u}^{sea} = d^{sea} = \overline{u}^{sea} \\ s^{sea} &= \overline{s}^{sea} = \tfrac{1}{2}\overline{u}^{sea} \end{aligned} \tag{3.19}$$

For the sea quark distributions in the nucleon, assuming no charm sea quark in the Q^2 range probed by this experiment, we have

$$\begin{aligned} u^{sea}_{nucleon}(x,Q^2) &= \tfrac{1}{5}S_{nucleon}(x,Q^2) \\ s^{sea}_{nucleon}(x,Q^2) &= \tfrac{1}{10}S_{nucleon}(x,Q^2) \end{aligned} \tag{3.20}$$

where $S_{nucleon}(x,Q^2)$ is the combined distribution of all sea quarks.

The calculated cross sections for the charged current deep-inelastic processes are shown in Figure 3.7, while the total charm-nonproducing νN ($\overline{\nu}N$) cross sections for both neutrino and antineutrino interactions by adding all the QE, EL, CCSP, NCSP, CCDIS, and NCDIS cross sections are shown in Figure 3.8.

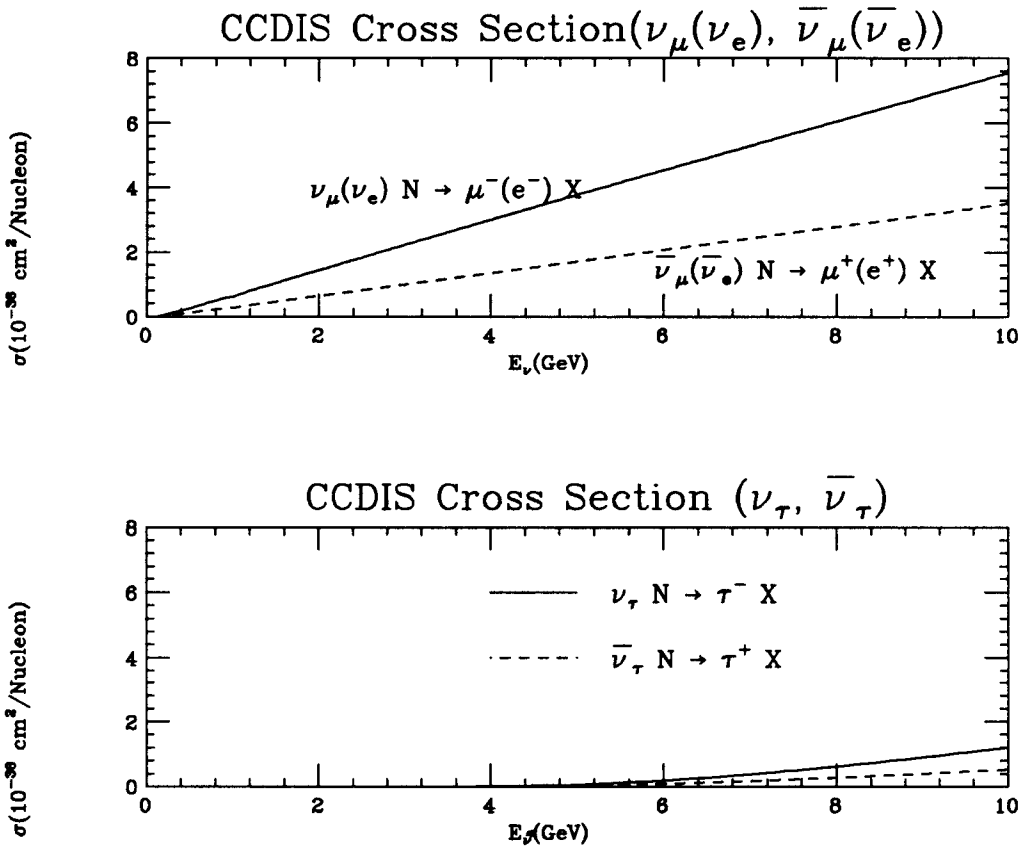

Figure 3.7: Charged Current Deep-Inelastic Cross Sections

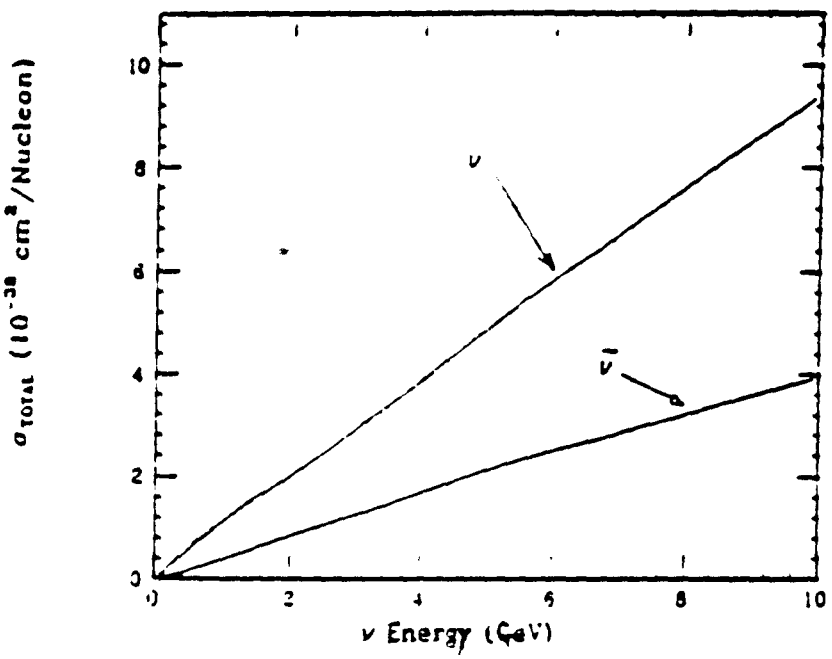

Figure 3.8: Total neutrino Cross sections

3.3 Charm-Producing Charged-Current Neutrino Interactions

3.3.1 Quasi-Elastic Charmed Baryon Production

Quasi-elastic charmed baryon production is the simplest type of exclusive charm-production reaction, Feynman diagrams of such processes are shown in Figure 3.9.

The original theoretical work for charmed baryon production was done by Benjamin W. Lee [41] before the discovery of charmed baryons. He even predicted the mass of the lightest charmed baryon to be around 2 GeV. In this section, all the cross section formulae follow his convention.

This is the most important channel for signal in this experiment since the neutrino beam peaks around $1 \sim 2$ GeV, and the lowest threshold energy to produce a charmed particle is 2.5 GeV for Λ_c^+, much lower than that for charmed meson production. Possible channels for exclusive QE production of charmed baryons are

$$\begin{aligned} \nu_\mu n &\longrightarrow \mu^- \Lambda_c^+ \quad (\Lambda_c^+ : \quad I = 0, \quad udc) \\ \nu_\mu p &\longrightarrow \mu^- \Sigma_c^{++} \quad (\Sigma_c^{++} : \quad I = 1, \quad uuc) \\ \nu_\mu n &\longrightarrow \mu^- \Sigma_c^+ \quad (\Sigma_c^+ : \quad I = 1, \quad udc) \end{aligned} \tag{3.21}$$

These are $\Delta Q = \Delta C = 1$, $\Delta S = 0$, $\Delta I = \frac{1}{2}$ transitions. There is no QE production of Σ_c^0. One important feature to note is that there are no antineutrino-induced quasielastic charm-producing reactions [41] due to the charge conservation.

Due to the $\Delta I = \frac{1}{2}$ property of the transition, the differential cross sections satisfy the relation

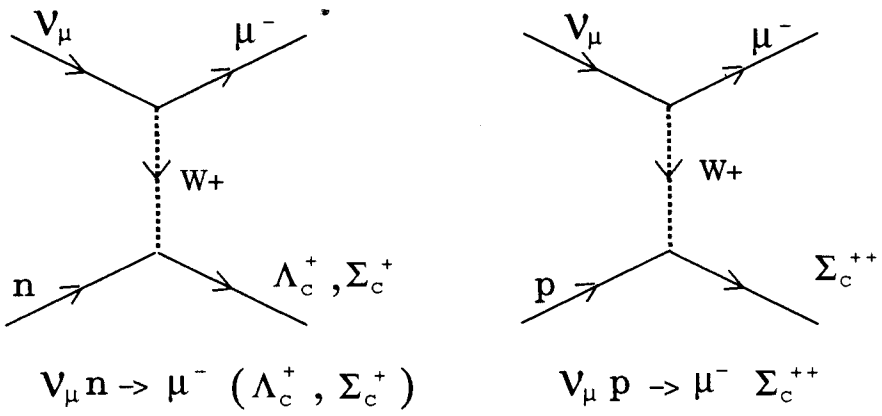

Figure 3.9: Feynman diagram for QE charmed baryon production

$$\frac{d\sigma}{dQ^2}(\nu_\mu p \longrightarrow \mu^- \Sigma_c^{++}) = 2\frac{d\sigma}{dQ^2}(\nu_\mu n \longrightarrow \mu^- \Sigma_c^{+}) \tag{3.22}$$

The invariant amplitudes for these reactions can be written in the form

$$M = \frac{G sin\theta_c}{\sqrt{2}} \overline{u}_\mu(l_2)\gamma_\lambda(1-\gamma_5)u_\nu(l_1) < C(p_2)|J^\lambda_{D+}|N(p_1) > \tag{3.23}$$

The matrix elements of the current J^μ_{D+} can be calculated using SU(4) symmetry, and expressed as

$$\begin{aligned} < \Lambda_c^+|J^\mu_{D+}|n > &= \sqrt{\tfrac{3}{2}}(\tfrac{1}{3}D + F)^\mu \\ < \Sigma_c^{++}|J^\mu_{D+}|p > &= \sqrt{\tfrac{3}{2}}(F - D)^\mu \end{aligned} \tag{3.24}$$

where,

$$\begin{aligned} F^\mu &= (F_V - F_A)^\mu \\ D^\mu &= (D_V - D_A)^\mu \end{aligned} \tag{3.25}$$

One then obtains for the vector part of the F and D matrix elements

$$\begin{aligned} F^\mu_V &= < p|J^\mu_{em}|p > + \tfrac{1}{2} < n|J^\mu_{em}|n > \\ D^\mu_V &= -\tfrac{3}{2} < n|J^\mu_{em}|n > \end{aligned} \tag{3.26}$$

That is,

$$\begin{aligned} F^\mu_V &= \overline{u}(p_2)\{(F_1^p - \tfrac{1}{2}F_1^n)\gamma^\mu + (F_2^p - \tfrac{1}{2}F_2^n)\tfrac{i\sigma^{\mu\nu}q_\nu}{m_N+m_C}\}u(p_1) \\ D^\mu_V &= -\tfrac{3}{2}\overline{u}(p_2)\{F_1^n\gamma^\mu + F_2^n\tfrac{i\sigma^{\mu\nu}q_\nu}{m_N+m_C}\}u(p_1) \end{aligned} \tag{3.27}$$

However, the vector part of J^μ_D is presumably dominated by the D^* meson, in contrast to the electromagnetic current, whose hadronic matrix elements exhibit vector-meson dominance by ρ, ω, and ϕ. In order to take this into account, the vector dipole

mass, m_V^2 in the Sachs form factor is replaced by $m_{D^*}^2$,

$$\begin{aligned} G_E^p(q^2) &= \frac{G_M^p(q^2)}{1+\mu_p} = \frac{G_M^p(q^2)}{\mu_n} = \frac{1}{(1-q^2/m_{D^*}^2)^2} \\ G_E^n(q^2) &\simeq 0 \end{aligned} \tag{3.28}$$

The Dirac and Pauli form factors are given by an obvious generalization of the usual relation to incorporate the mass difference between the initial and final baryons:

$$\begin{aligned} F_1^{p,n}(q^2) &= \frac{G_E^{p,n}(q^2)-\{q^2/(m_N+m_C)^2\}G_M^{p,n}(q^2)}{1-q^2/(m_N+m_C)^2} \\ F_2^{p,n}(q^2) &= \frac{G_M^{p,n}(q^2)-G_E^{p,n}(q^2)}{1-q^2/(m_N+m_C)^2} \\ F_2^p(0) &= \mu_p \\ F_2^n(0) &= \mu_n \end{aligned} \tag{3.29}$$

For the axial-vector part of the F and D matrix elements,

$$\begin{aligned} F_A^\mu &= \frac{F}{F+D} < p|F_{1+i2}^{5\mu}|n > \\ D_A^\mu &= \frac{D}{F+D} < p|F_{1+i2}^{5\mu}|n > \end{aligned} \tag{3.30}$$

where $F = 0.45 \pm 0.02$, $D = 0.78 \pm 0.02$, and

$$\begin{aligned} < p|F_{1+i2}^{5\mu}|n > &= \overline{u}(p_2)\gamma^\mu\gamma_5 F_A(q^2)u(p_1) \\ F_A(q^2) &= \frac{1}{(1-q^2/m_A^2)^2} \end{aligned} \tag{3.31}$$

Finally the expressions for the axial-vector part can be determined,

$$\begin{aligned} F_A^\mu &= F\overline{u}(p_2)\gamma^\mu\gamma_5 F_A(q^2)u(p_1) \\ D_A^\mu &= D\overline{u}(p_2)\gamma^\mu\gamma_5 F_A(q^2)u(p_1) \end{aligned} \tag{3.32}$$

Here for the axial-vector mass, m_A, the mass of D^* (m_{D^*}) was used to reflect the dominance of the axial-vector part of the current by charmed axial-vector mesons. In these expressions, the following assumptions were made:

- T invariance $\rightarrow$ All form factors are real.

- Absence of second-class currents

  $\rightarrow$ There is no q^ν term in Eq. (3.27) and no $i\sigma^{\mu\nu}q_\nu\gamma_5$ term in eq.(3.31).

- Induced pseudoscalar term $F_p(q^2)q^\mu\gamma_5$ is negligible, since it gives a contribution proportional to the muon mass.

In general,

$$\begin{aligned} < C|J^\mu_{D+}|N >= \ & \bar{u}(p_2)\{A(q^2)\gamma^\mu + B(q^2)\tfrac{i\sigma^{\mu\nu}q_\nu}{(m_N+m_C)} \\ & +C(q^2)\gamma^\mu\gamma_5\}u(p_1) \end{aligned} \tag{3.33}$$

where A, B, and C can be determined for the various reactions using the equations above, and are explicitly written as follows. For $< \Lambda_c^+|J^\mu_{D+}|n >$, A, B, and C are

$$\begin{aligned} A(q^2) = \ & \sqrt{\tfrac{3}{2}}F_1^p \\ B(q^2) = \ & \sqrt{\tfrac{3}{2}}F_2^p \\ C(q^2) = \ & -\sqrt{\tfrac{3}{2}}(\tfrac{1}{3}D + F)F_A(q^2) \end{aligned} \tag{3.34}$$

For $< \Sigma_c^{++}|J^\mu_{D+}|p >$, A, B, and C are

$$\begin{aligned} A(q^2) = \ & \sqrt{\tfrac{3}{2}}(F_1^p + 2F_2^n) \\ B(q^2) = \ & \sqrt{\tfrac{3}{2}}(F_2^p + 2F_2^n) \\ C(q^2) = \ & -\sqrt{\tfrac{3}{2}}(F - D)F_A(q^2) \end{aligned} \tag{3.35}$$

Then, neglecting the lepton mass, the differential cross section can be written as

$$\frac{d\sigma}{dQ^2} = \frac{G^2 sin^2\theta_c}{8\pi E_\nu^2}\{-2q^2W_1 + (4E_\nu E_\mu + q^2)W_2 + \frac{(E_\nu + E_\mu)}{m_N}q^2W_3\} \tag{3.36}$$

where E_ν is the energy of the neutrino in the lab frame, E_μ is the energy of the scattered muon in the lab frame,

$$E_\mu = E_\nu + \frac{q^2}{2m_N} + \frac{M^2 - M_C^2}{2M} \tag{3.37}$$

and W_1, W_2, and W_3 are

$$\begin{aligned} W_1 = & \frac{1}{4m_N^2}\{[(m_C - m_N)^2 - q^2]|A+B|^2 \\ & +[(m_C + m_N)^2 - q^2]|C|^2\} \\ W_2 = & |A|^2 - \frac{q^2}{(m_N+m_C)^2}|B|^2 + |C|^2 \\ W_3 = & 2C(A+B) \end{aligned} \tag{3.38}$$

The calculated cross sections of neutrino induced QE charmed baryon production are shown in Figure 3.10.

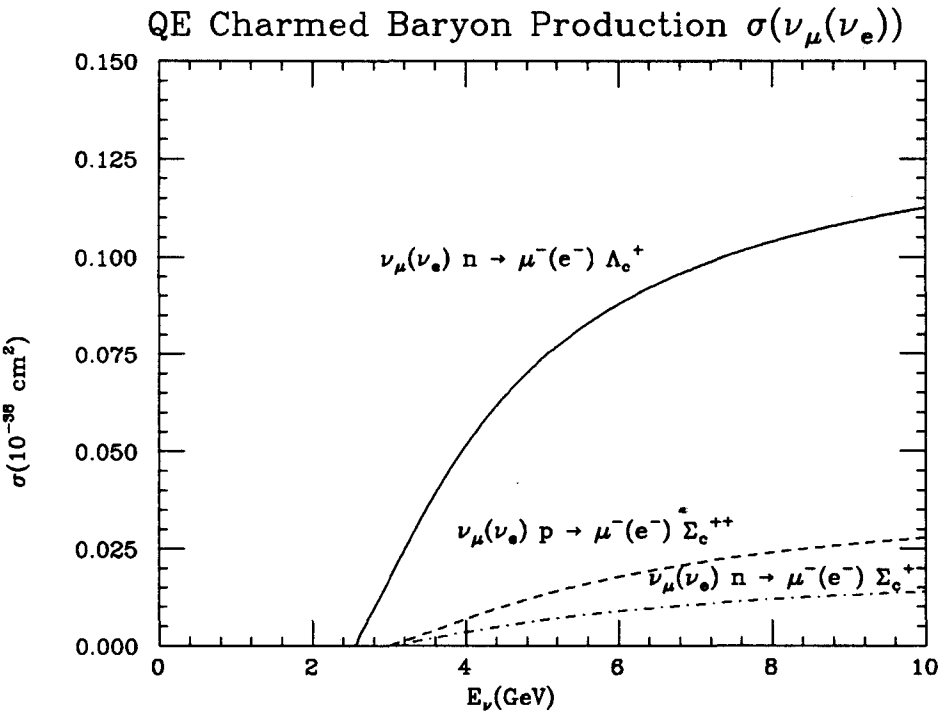

Figure 3.10: Cross sections of QE charmed baryon production

3.3.2 Deep-Inelastic Charm Production

In the AGS neutrino beam energy region up to 10 GeV, charged-current deep-inelastic charm production is dominated by the production of a single charmed quark from a down or strange quark from either a valance quark or a sea quark. Antineutrinos can also produce an anti-charm quark from an antiquark, but this can only be from a sea quark since there are no valance antiquarks. Feynman diagrams for these processes are shown in Figure 3.11. In the AGS beam energy region the sea quark contribution is very small, so the dominant mechanism for this process is a charmed quark produced from a down valance quark, which is shown in the box in Figure 3.11.

Charm production is an specific case of the usual charged-current deep-inelastic scattering. In the previous section, the deep-inelastic cross section was developed assuming massless quarks, which can not be applied to the massive charm quark case. For production of a heavy charm final state particularly around the threshold energy region, the structure functions do not scale with the usual scaling variable, x_{BJ}, so this needs to be modified to incorporate the heavy quark mass effect. Georgi-Politzer and others [42, 43] introduced the so called *slow rescaling mechanism*, in which structure functions scale with the *slow rescaling variable*, ξ.

This ξ can be understood as being related to the momentum fraction carried by a struck quark when a heavy quark is produced (ξp instead of xp where p is the

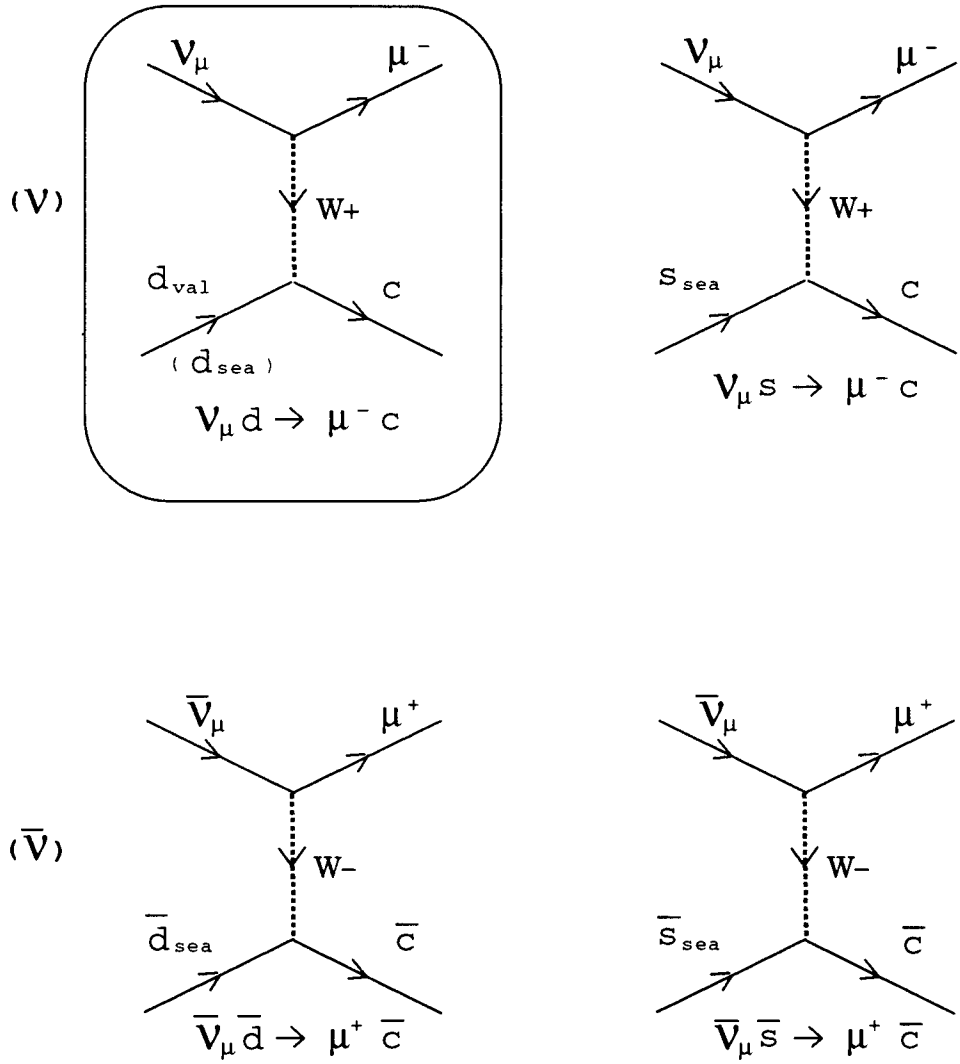

Figure 3.11: Feynman diagram for Deep-inelastic charm production

four-momentum of the target nucleon). This can be demonstrated as follows

$$\begin{aligned} (\xi p + q)^2 &= (p_c)^2 \\ \xi^2 M^2 + 2\xi p \cdot q + q^2 &= m_c^2 \\ \xi &\simeq \tfrac{Q^2}{2M\nu} + \tfrac{Q^2}{2M\nu} \\ \xi &\simeq x_{BJ} + \tfrac{Q^2}{2M\nu} \end{aligned} \tag{3.39}$$

where p_c is four-momentum of produced charm quark. Note that ξ reduces to x_{BJ} for $\nu \to \infty$ and for $m_c \to 0$. From the definition,

$$\xi = x + \frac{Q^2}{2M\nu} = x + \frac{Q^2}{2ME_\nu y} \tag{3.40}$$

it's easy to see that the kinematically accessible region is given by

$$\begin{aligned} \tfrac{m_c^2}{2ME_\nu} &\leq \xi \leq 1 \\ \tfrac{m_c^2}{2ME_\nu \xi} &\leq y \leq 1 \end{aligned} \tag{3.41}$$

For heavy quark production by ν and $\overline{\nu}$, the y-distribution for the cross section is changed from a flat distribution to the distribution of the following form,

$$(1-y) + \frac{xy}{\xi} = 1 - \frac{m_c^2}{2ME_\nu \xi} \equiv \kappa \tag{3.42}$$

which is due to the mixed helicity of heavy charm quark states.

Changes in the quark distribution functions are also needed. For the process, $d_{valance} \to c$, we define

$$d^{val}_{nucleon}(\xi, Q^2) = \kappa\theta_D\{(1+f)u^{val}_{proton}(\xi, Q^2) + (1-f)d^{val}_{proton}(\xi, Q^2)\} \tag{3.43}$$

where $\theta_D \equiv \theta(W^2 - (M_D + M)^2)$, a step function. For the processes, $d_{sea} \rightarrow c$, $s_{sea} \rightarrow c$, we define

$$\begin{aligned} d^{sea}_{nucleon}(\xi, Q^2) &= \kappa\theta_D \tfrac{1}{5} S_{nucleon}(\xi, Q^2) \\ s^{sea}_{nucleon}(\xi, Q^2) &= \kappa\theta_D \tfrac{1}{10} S_{nucleon}(\xi, Q^2) \end{aligned} \tag{3.44}$$

Note that these expressions do not include radiative corrections which are negligible in the low (below 10 GeV) beam energy region. The strange quark distribution was assumed to be [40],

$$s_{sea}(\xi, Q^2) = \frac{1}{2} d_{sea}(\xi, Q^2) \tag{3.45}$$

Another free parameter is the charm quark mass, which was chosen to be $1.3 GeV/c^2$ using the latest results from the CCFR group [44].

The charged-current deep-inelastic charm production differential cross section is described by

$$\begin{aligned} \tfrac{d^2\sigma}{dxdy}(\nu_\mu N \rightarrow \mu^- cX) &= \tfrac{G^2 M E_\nu}{\pi}\{|V_{cd}|^2(\xi d_{val}(\xi, Q^2) + \xi d_{sea}(\xi, Q^2)) + |V_{cs}|^2 \xi s_{sea}(\xi, Q^2)\} \\ &\quad \cdot(1 - \tfrac{m_c^2}{2ME_\nu\xi}) \\ \tfrac{d^2\sigma}{dxdy}(\overline{\nu}_\mu N \rightarrow \mu^+ \overline{c}X) &= \tfrac{G^2 M E_\nu}{\pi}\{|V_{cd}|^2 \xi \overline{d}_{sea}(\xi, Q^2) + |V_{cs}|^2 \xi \overline{s}_{sea}(\xi, Q^2)\} \\ &\quad \cdot(1 - \tfrac{m_c^2}{2ME_\nu\xi}) \end{aligned} \tag{3.46}$$

where V_{cd} and V_{cs} are elements of the Kobayashi-Maskawa(KM) matrix [18] describing the c to d, and d to s quark couplings respectively. The step function θ_D in the quark distribution functions is introduced to make sure that hadronic mass is large enough to produce a charmed meson. The slow rescaling suppresses the cross section at low

neutrino energy (around threshold) and at low y.

The calculated cross sections of neutrino induced charged current deep-inelastic charm productions are shown in Figure 3.12.

3.4 Event Monte Carlo

The E776 Monte Carlo consist of two parts; one is the neutrino beam simulation which was outlined in chapter 2, and the other one is the event simulation Monte Carlo.

The event Monte Carlo first generates neutrino interactions in the detector, then traces all the outcoming particles from the interaction through the detector. For a given neutrino flavor and running condition ($\nu-$run, or $\overline{\nu}-$run), we first generate the neutrino energy according to the corresponding beam spectrum at the detector site (1 km away from the target), then either a proton or a neutron was chosen as the target nucleon with a so called Fermi momentum, which follows the distribution of p^2 up to cut off momentum (Fermi level) of 230 MeV/c. (Fermi momentum distribution is shown in Figure 5.15.)

Then we calculate S, the center of mass energy squared, and select the interaction channel randomly, weighted according to the relative cross sections among the various charged and neutral current interactions possible at that energy.

The neutrino interaction can take place anywhere in the target detector. Right after the interaction, unstable particles like π^0, τ^+, τ^- Λ_c^+, Σ_c^+, or Σ_c^{++} will decay and with the granularity of the E776 detector will not be observed. So the subsequent

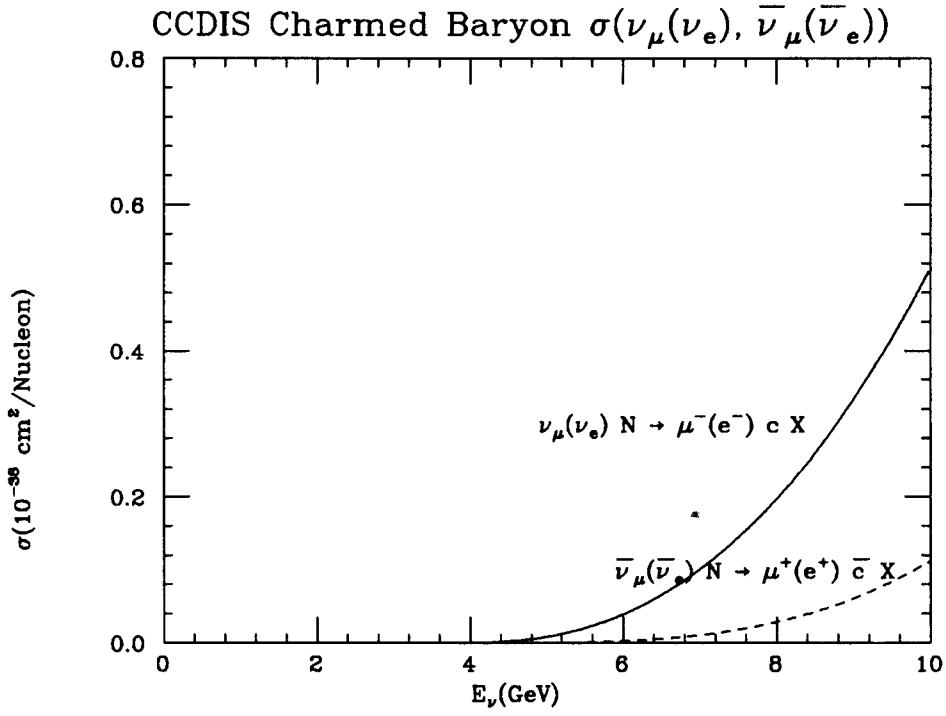

Figure 3.12: Cross section for Deep-inelastic charm production

decay of these unstable particles were included in the event generator. For charmed particles, only the muon decay mode is considered.

For τ^+, and τ^-, the package TAUOLA, which treats the decay with appropriate polarization was adapted. For various charmed baryon decays, the LUND package was incorporated into our event generator. For simple two body decays (like $\pi^0 \rightarrow \gamma\gamma$, $\pi^+ \rightarrow \mu^+\nu_\mu$, $\pi^- \rightarrow \mu^-\overline{\nu}_\mu$, etc) we wrote our own code.

After the particles are produced, they are transported through the target nucleus and then through the detector. The intranuclear transport was simulated using the routine NUCRIN, which provided a model for hadron-nucleus interactions below particle momentum of 5 GeV/c [28]. The essential features of this model were [33]:

- Leptons were treated as non-interacting.
- The particles considered included pions, nucleons, kaons, and hyperons.
- Pions could charge exchange, be absorbed, escape the nucleus without interacting, or produce a Δ resonance which then decayed.
- Baryons could hadronically interact or escape the nucleus.
- A nucleon with kinematic energy less than 25 MeV could not leave the nucleus.

After the particle propagates through the target, the four vector of the original particle is modified as a result of the intranuclear interaction.

Next the particles are transported until they leave the detector, or they reach a minimum energy (50 keV for electrons and 1 MeV for muons and hadrons).

To obtain the details of the detector, we have surveyed various parts of the detector (PDT planes, PDT wires, concrete slabs, scintillation planes, etc.) after installation, and also measured the magnetic field of the toroid spectrometer [45]. Also various electronic parameters are incorporated into the detector simulation [34].

Particles which develop electromagnetic showers are propagated using the EGS4 routine [46]. Hadrons and muons are transported step by step using a very small step size, considering the decay, and interaction probability. Daughter particles can appear as a result of a decay or an interaction, and these are also propagated in the same manner. The detector response is simulated for all the charged particles.

This completes the event simulation. All the hits generated so far are associated with the actual event. If the Monte Carlo events are compared with real data, data frames may have some random hits in the detector or be overlapped with a cosmic ray track. To be more realistic, the Monte Carlo events were combined with a free trigger frame (actual data taken between the AGS pulses), allowing the Monte Carlo to have the same noise contamination as the data.

In the Monte Carlo simulation, charm producing neutrino interactions usually have an order of magnitude smaller cross section than those of conventional charm nonproducing neutrino interactions. This analysis is designed to look for charm induced opposite sign dimuon events. In order to study these samples, charm and noncharm Monte Carlo sample were generated separately.

The first set was charm nonproducing interactions which are the source of most

of the background for dimuons, called MC events. The second set of Monte Carlo is for charm producing interactions, which subsequently decay to muons. This set of events is called Charm_MC events.

Chapter 4

DATA REDUCTION

4.1 E776 WBB Data

In 1986, data was taken with the Wide Band Neutrino Beam. The total numbers of proton on target were 1.43×10^{19} POT for neutrinos, and 1.55×10^{19} POT for antineutrinos. Although the neutrino energy peaks around $1 \sim 2$ GeV, the high energy tail extends to 10 GeV. This makes it possible to study quasi-elastic production of charmed baryons, as the threshold for the lightest charmed baryon (Λ_c^+) production is 2.5 GeV, while the deep inelastic production of charmed particles has threshold energies of $5 \sim 6$ GeV and the production cross section in this energy region is small. This makes this an ideal place to study charmed baryon production.

The data were recorded for every AGS pulse. The neutrino event rate was about one in every 10 AGS pulses for the neutrino run and one in every 20 pulses for the antineutrino run. In addition to neutrino triggers, free triggers and cosmic ray triggers were also taken. The free data was taken between the AGS pulses, to measure possible cosmic ray backgrounds. The cosmic data was taken to monitor the detector

performance during the run. The relationship between these three types of triggers are shown in the Figure 4.1, and they are :

Beam Trigger: Triggered at each AGS spill to get the beam related events. Beam trigger gate is open for 3μsec starting 2.67μsec after beam extraction to allow for long electron drift times in the PDT's.

Cosmic Trigger: To collect long cosmic rays to monitor detector performance. The cosmic trigger gate is open for 400 msec starting 500 msec before the AGS extraction time.

Free Trigger: To collect random cosmic ray background. The free trigger gate is open for the same period of time as beam gate starting 100 msec after termination of the beam gate.

The total number of raw data events collected for the neutrino and antineutrino running are shown in Table 4.1.

Approximately 3 million triggers (including free and cosmic ray triggers) each for the neutrino run and the antineutrino run were collected (Table 4.1). We first separated the cosmic triggers from the real and free neutrino triggers. The cosmic data was analyzed separately to monitor detector performance. We define a "frame" as a set of hits recorded at each trigger which can be viewed as a event picture if the trigger contains a neutrino interaction. Since each beam trigger is recorded regardless of contents and with lots of other necessary information, the raw data set

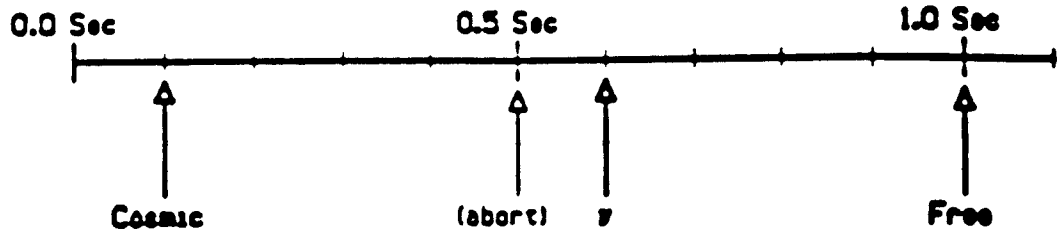

Figure 4.1: Trigger timing

is huge (hundreds of magnetic tapes), but more than 90 % of the frames contain no neutrino interactions.

The first task is to remove all the empty frames to reduce the data sample to a manageable level. This was done by series of filter programs. The data reduction scheme is shown in Figure 4.2. The real neutrino and free data were mixed in the sample and went through the analysis in the same manner.

4.2 Initial Filters

4.2.1 EDIT1

EDIT1 is the first off-line filter program, and was designed to remove a majority of the empty frames and frames which contain a few random hits. Event selection criteria for EDIT1 are:

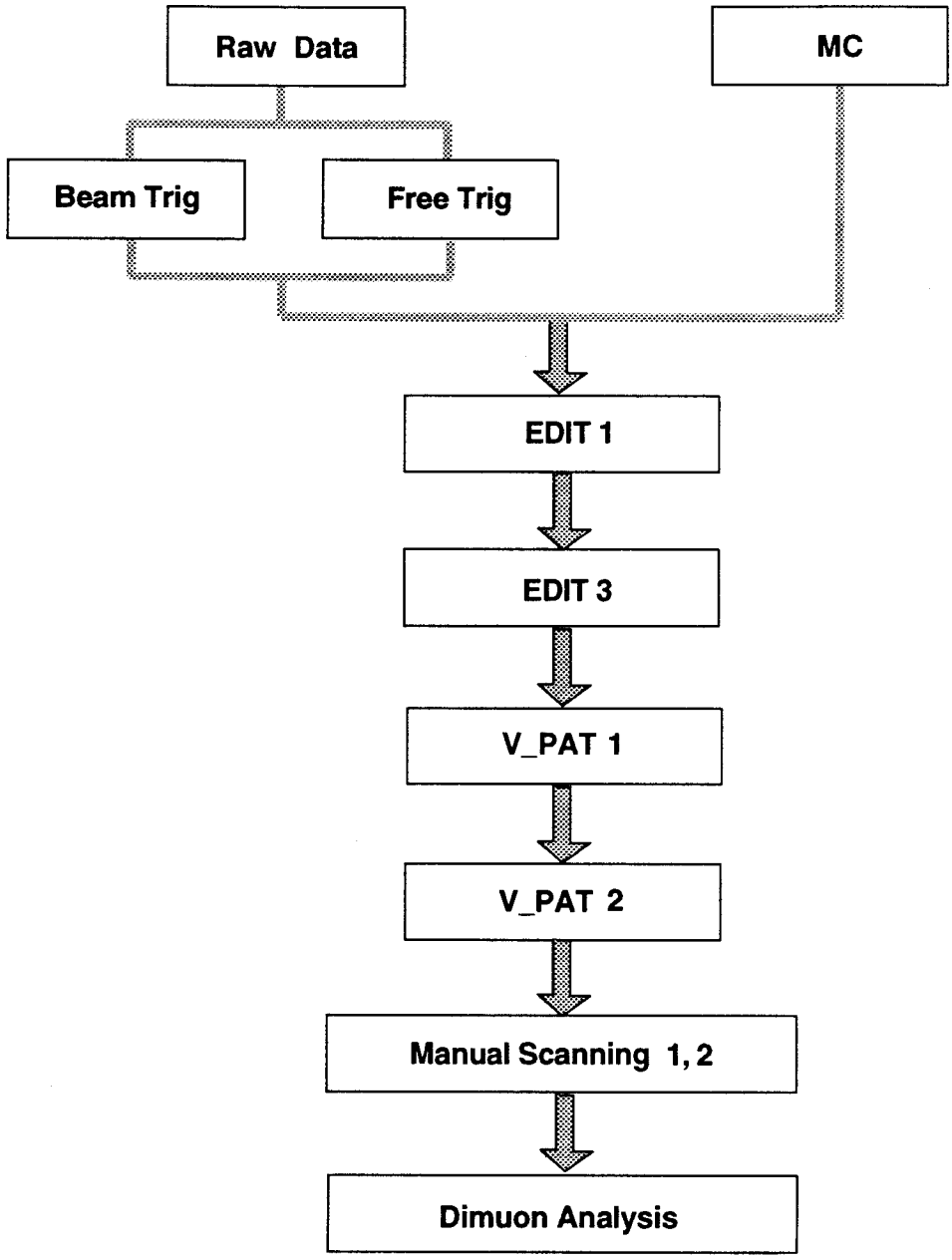

Figure 4.2: Data Reduction Flow

	ν - Run		$\overline{\nu}$ - Run	
	Beam Trigger	Free Trigger	Beam Trigger	Free Trigger
Raw Data	1,377,965	1,364,183	1,256,613	1,259,323
EDIT1	315,729 (77.1%)	26,059 (98.1%)	234,887 (81.3%)	24,050 (98.1%)
EDIT3	78,122 (94.3%)	6,488 (99.5%)	27,680 (97.8%)	6,034 (99.5%)

Table 4.1: E776 Data Reduction (data reduction factor is shown in the parentheses) Note that this was done before the analysis started, so this is not the sample the dimuon analysis is based on.

1. Total number of PDT hits in the calorimeter ≥ 10.

2. Each PDT hit should have a neighbor hit within 3 consecutive planes in each view.

3. criteria: PDT hits which satisfy the above condition should form a cluster at least 3 consecutive planes long in each view.

Event reduction factors are shown in Table 4.1. Details of the algorithms and energy dependent for the various interaction channels can be found in references [33, 47].

4.2.2 EDIT3

EDIT3 is the second off-line filter program, and performs a crude pattern reconstruction to determine whether the frame is a neutrino event related or not. Event selection

criteria for EDIT3 are:

1. The frame should have at least 4 consecutive plane hits in each view.

2. When no track is found by the simple pattern recognition routine, the frame is saved if:

   - Total number of PDT hits in the calorimeter < 250
   - Total number of PMT hits in the calorimeter < 80
   - Total number of PDT hits in the toroid < 10

     (The frames passed through the EDIT1 already have more than 10 PDT hits in the calorimeter.)

3. When a track is found in either the x, or y view, the frame is saved if:

   - Total number of PDT hits in the track ≥ 4
   - Total track length ≥ 3 planes
   - The beginning of the track (possible vertex) is within the fiducial volume (here, loosely defined as more than 2 wires in from the side and 4 planes in from the front of the calorimeter).

4. When crude tracks are found in both x and y views, the frame is saved if the most upstream hits in both views are within 10 planes of each other.

Event reduction factors for EDIT3 are shown in Table 4.1. Details of the algorithm and energy dependent acceptance for the various interaction channels can be found

in [33, 47].

These two filters, EDIT1 and EDIT3, have been used to reduce the data for both the NBB and WBB data analysis in the group and have been shown to be very effective in reducing unwanted frames. As one can see in Table 4.1, the reduction factor for the free trigger data was more than 99% for both neutrino and antineutrino runs.

4.2.3 WBB Data and Monte Carlo Event Samples

At the time this dimuon analysis began, the lowest level of data was after EDIT3 filter, and whole EDIT3 data sample was no longer available. This analysis is based on the part of the data sample available at that time, and is shown in Table 4.2. The fractions of EDIT3 data actually analyzed for this analysis. are also shown in the Table 4.2. (The previously shown Table 4.1 is not the sample this analysis is based on.)

	ν - Run		$\overline{\nu}$ - Run	
Dimuon Analysis	Beam Trigger	Free Trigger	Beam Trigger	Free Trigger
Available EDIT3	76,302	6,339	22,864	4,913
$\frac{\text{Available EDIT3}}{\text{Total EDIT3}}$	97.7 %	...	82.6 %	...

Table 4.2: E776 data after EDIT3, actually used for dimuon analysis. Fraction of analyzed EDIT3 data of the total EDIT3 data is also shown.

There are 5 sets of event samples used for dimuon analysis:

- For $\nu-$**run**, there are three samples:
  - **WBB data:** We started with 76K EDIT3 beam trigger frames.
  - **MC event sample:** The Monte Carlo event sample of charm nonproducing interactions is to study background. We started with 100K original Monte Carlo events (which include 40K CCDIS events). The actual numbers of events are shown in parentheses in the data reduction tables. The numbers in the tables without parentheses are normalized to the number of the WBB EDIT3 beam triggers, so that these event numbers can be directly compared to the WBB event numbers.
  - **Charm_MC event sample:** The Monte Carlo sample of charm produced dimuon events (only from Λ_c^+ to study the characteristics of the signal and the acceptance of the entire analysis. We started with 10K original Monte Carlo events. Only a fraction of the sample were manually scanned after the pattern program, V_PAT2, so the event number afterwards needed to be normalized to the original 10K generated event numbers.
- For $\overline{\nu}-$**run**, there are only two samples. There is no Charm_MC event sample since we expect no dimuon events from antineutrino interactions. (The antineutrino deep inelastic charm production is so small, and it can be ignored in the neutrino energies below 10 GeV.)

- **WBB data** We started with 23K EDIT3 beam trigger frames.

- **MC event sample:** The Monte Carlo event sample of charm nonproducing interactions. We started with 30K original Monte Carlo events, The actual numbers of events are shown in parentheses in the data reduction tables. The numbers in the tables without parentheses are normalized to the number of the WBB EDIT3 beam triggers, so that these event numbers can be directly compared to the WBB event numbers.

The purpose of the series of data reductions is to select all two track events in which both tracks are potential muons. Topologically, we are looking for events which have two or more tracks originating from the same vertex. A typical Monte Carlo Charm_MC dimuon event which has hits in the toroid is shown in Figure 4.3. Another Monte Carlo Charm_MC dimuon event with two tracks entering the toroid, is shown in Figure 4.4, and this is the kind of event we finally looked for in the dimuon analysis to do the sign measurement on both tracks.

To select two track events and eliminate most single track events, we first find a vertex of a two track event(V_PAT1). Then, we apply track length cuts to make sure the tracks are likely muons and not hadrons (V_PAT2). Since we are looking such a rare event in a mostly single track event sample, we take a very careful approach, manual scanning, to remove evident events containing a electromagnetic shower or hadron track characterized by second interaction vertex, and kink in the track (Manual scan1). The remaining events were studied in various way and carefully looked

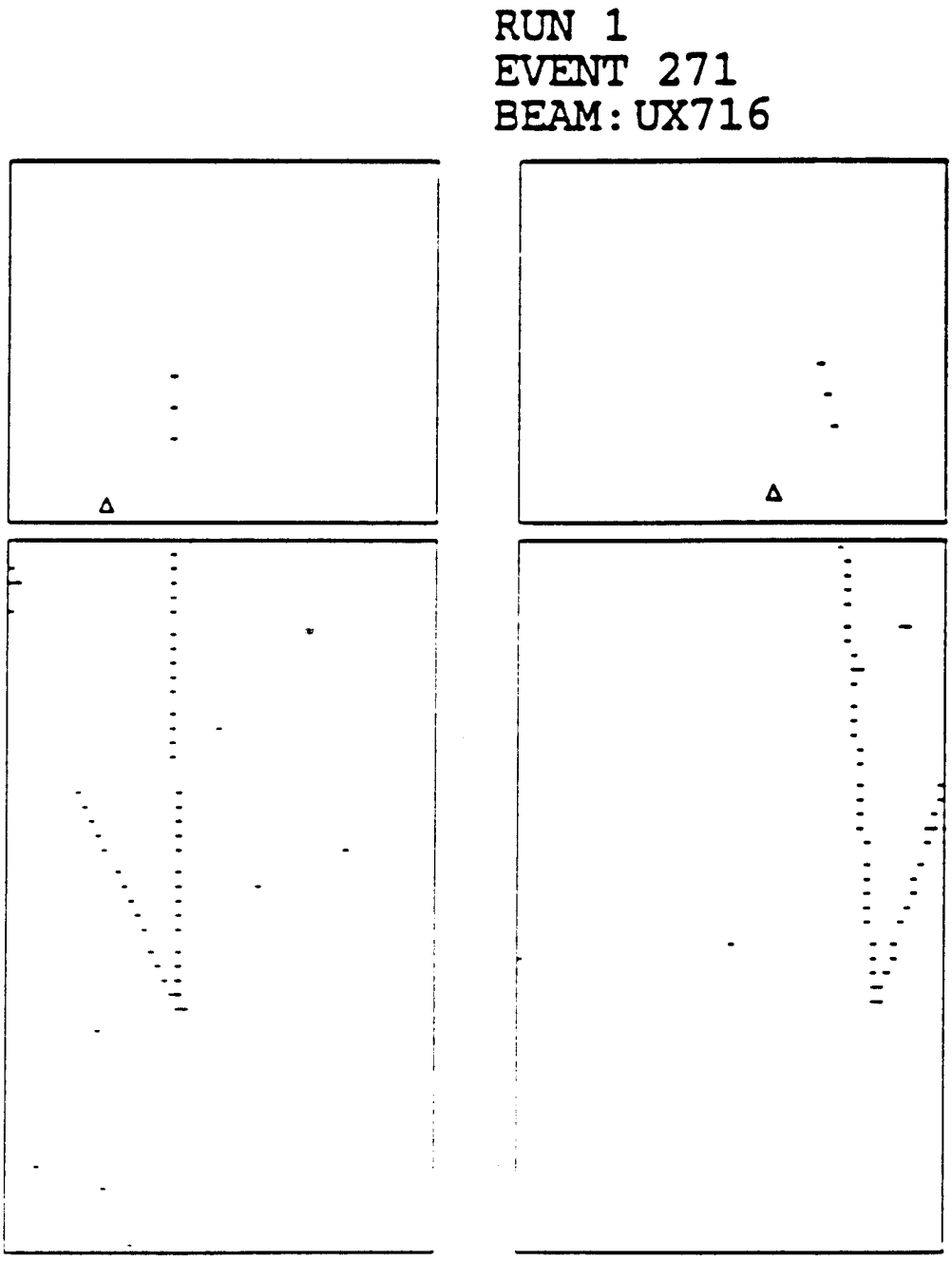

Figure 4.3: A typical Monte Carlo Charm_MC opposite sign dimuon event which has hits in the toroid

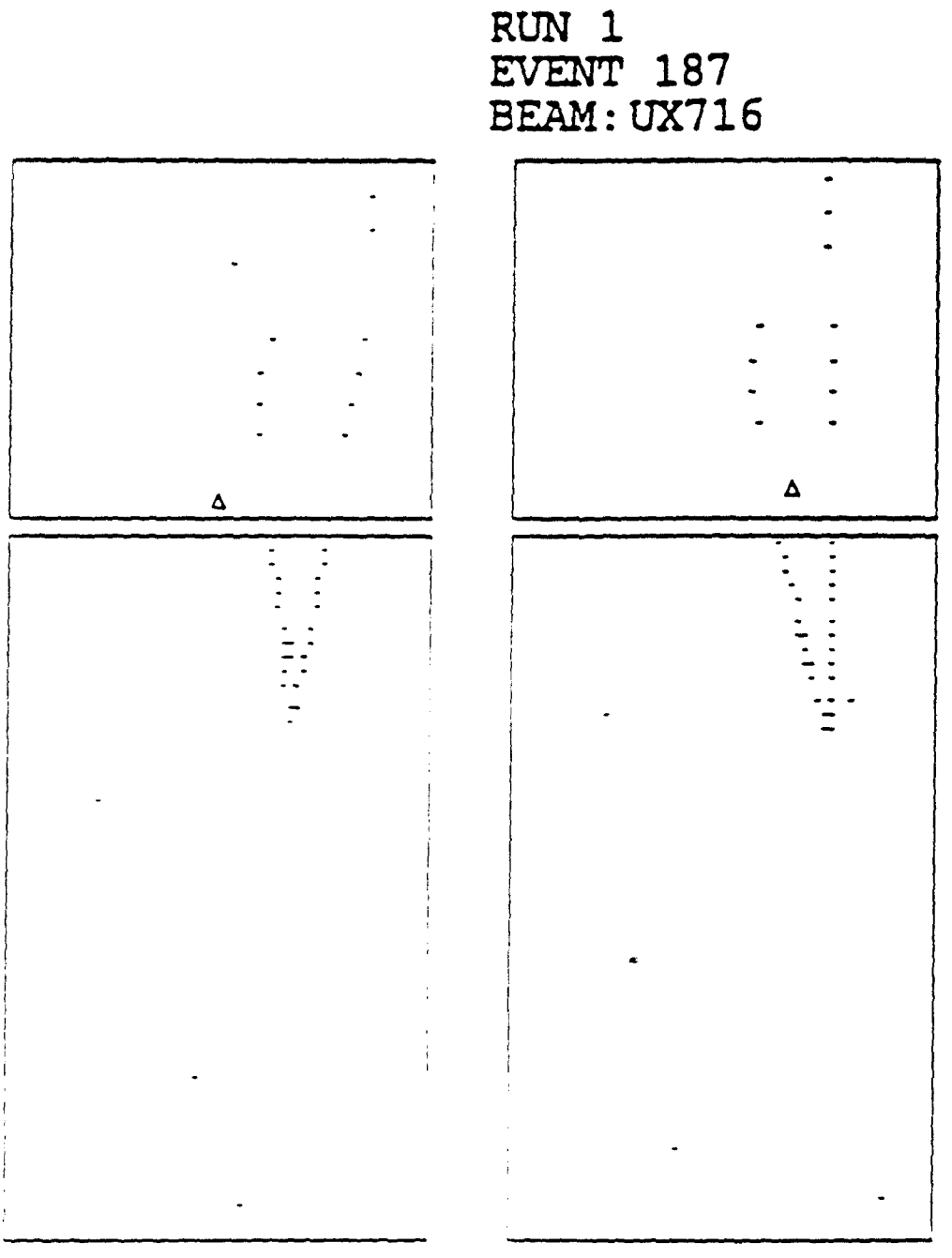

Figure 4.4: A Monte Carlo Charm_MC opposite sign dimuon event with two tracks entering the toroid. This is the kind of event we finally looked for in the dimuon analysis to do the sign measurement on both tracks.

at, then the stricter manual scanning rule was applied to remove mostly high multiplicity events and the events without toroid hits. In the dimuon search, to separate signals from the background, it is so important to measure the sign of the track, so we required the event to have at least one toroid hit. In addition, we also measured the end points of each track (Manual scan2).

Selecting events with two long tracks (not high multiplicity) with at least one hit in the toroid only using the event topology, so called pattern, without sophisticated χ^2 analysis was the goal of this entire data reduction.

4.3 V_PAT1

The event selection strategy is to select all the potential dimuon events. Topologically, we are looking for events which have two or more tracks originating from the vertex. Since the life time of charm baryons and mesons are $10^{-12} \sim 10^{-13}$ *sec*, they travel no more than 10^{-2} *cm* before decaying. We do not expect to observe any separation between the production and decay vertices of the charmed particles in the E776 detector.

Our first task is to eliminate most single track events, as most of charged current neutrino events have a leading muon with some activity around the vertex. Then we select possible two track events. Our pattern program, V_PAT1, used to find a possible vertex for the two tracks then followed the following steps.

4.3.1 Event Related Hits

We first want to eliminate hits unrelated to the event. A typical event (which is single track event) is shown in Figure 4.5. We can see hits unrelated to the event. These are random hits, or associated tracks which are usually from either cosmic ray sources or debris (mostly neutrons) from the primary proton beam interactions at the target. Most of these hits are separated from the event hits both in time and in space.

The time distribution of hits in the frame are plotted, and the peak of the distribution, t_{peak}, is determined. Hits which arrive before this peak time or significantly later than this peak time are eliminated. Once the hits are within this time window, we now ask if each hit is a part of a cluster. If the hit is isolated in space, it is eliminated.

In this particular analysis, we are interested primarily in continuous straight tracks and not in showers. If a hit is part of a track, then the hit should have additional hits in the neighboring upstream or downstream planes. If there are neighbor hits within 2 wire and 2 plane (in each view) spacings, then we look for other neighbor hits adjacent to these neighbor hits, within 5 wires and 3 (in each view) planes. Only when both of the neighbor hits are found, the test hit is considered to be part of a track.

Once the topological searching for hits is over, the total number of hits in the event are counted. We require that the total hits associated with a event should be greater than 20 to do a reasonable track reconstruction of two tracks.

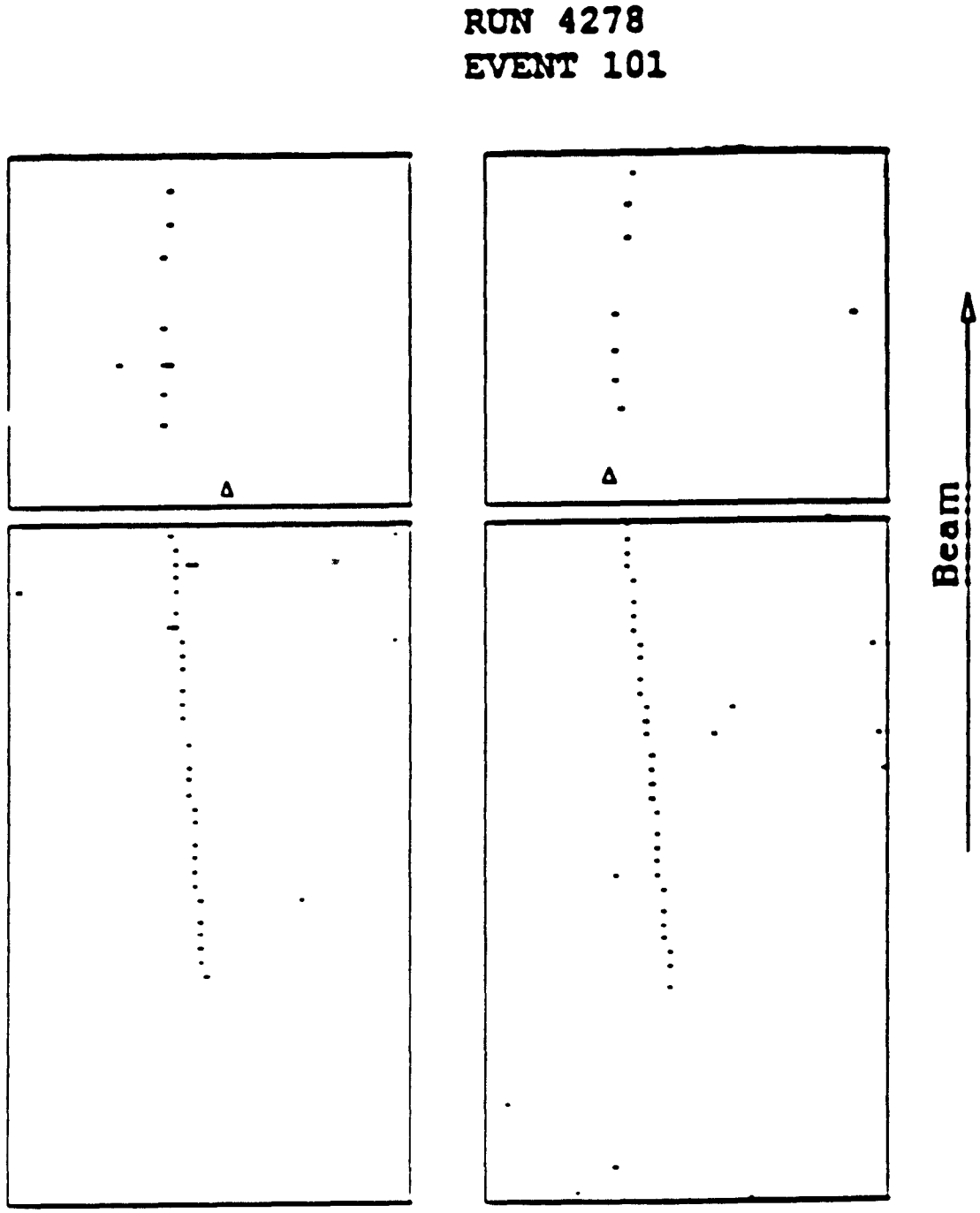

Figure 4.5: A typical E776 event

4.3.2 Vertex

Vertex plane

The first step in locating the vertex is to identify the vertex plane.

If there is a track, then we expect to see the track in both the X and Y view, beginning and ending at about the same positions in Z (beam direction). In practice, we find each vertex plane in the X and Y view independently, then the most upstream plane is defined as a vertex plane of a event, since the X and Y measurements are independent in the E776 detector.

Using the hits not eliminated from the above consideration, we ask, 'what is the average number of hits per plane for consecutive planes?'. If there is only one track in each view, we expect to see an average of two hits per combined adjacent $X + Y$ planes for the entire track length. If there are two tracks in each view, we expect the average number of hits to be four for up to the shorter track length. If two tracks overlap in one view, we expect the average number of hits to be three while overlapping. This may not be the case for a "gappy" electron shower, but remember we are only interested in muon-like tracks.

Starting from the most upstream planes of the detector, we look for the place where the combined number of hits for the adjacent $X + Y$ planes are greater than or equal to 3 hits for more than three consecutive pairs of planes. The most upstream pair of planes is then regarded as the possible vertex planes of the two tracks in both views.

Two track events often overlap at the beginning of the track when the angle between them is small and visibly separate after traveling some distance, but they rarely overlap for more than 10-15 planes in both views. Sometimes hadrons, (π^+, π^-, proton, neutron, etc.), travel some distance and interact producing secondary particles from the interaction vertex. To avoid picking up these pair of secondary interaction vertex planes, we require that upstream of the potential vertex planes, pairs of adjacent $X + Y$ planes with combined hits greater than or equal to 2 should not continue for more than 8 consecutive planes. Events which do not satisfy these conditions, mostly single track events or events with visible hadron tracks, are eliminated.

We consider the most upstream pair of the X and Y planes where the consecutive hits started as possible vertex planes in each view.

Vertex

Once we have a pair of vertex plane candidates (i.e. Z position of vertex in each X and Y view is determined), the task is to define a transverse vertex position (i.e. X and Y positions) in each view.

We calculate the geometric average position of the wires (X or Y) and the standard deviation (σ_x, or σ_y) in each view for 3 planes including the vertex plane, and the next two downstream planes. If the standard deviation is smaller than 3 wire spacings, then the hits on the possible vertex plane are vertex candidates (X or Y) in each view. Otherwise, this wire position test continues by removing a PDT hit which contributes the most to the large standard deviation, from the hits used in calculating the average

wire position, until the standard deviation becomes smaller than 3 wire spacings.

If there are multiple candidates for the vertex on the possible vertex plane, then VTEST is performed to make sure that no hits associated with the event exist upstream of the possible vertex plane. VTEST is described as follows. If a test PDT hit on the possible vertex plane is truly a vertex, then there should be at least 2 hits in the downstream box in Figure 4.6, and there should be less than 2 hits in the upstream box in Figure 4.6 (low energy back scattering particles can give a couple of hits in the upstream, but this is rare). The larger upstream box was chosen to make sure no hits exist before the vertex. When there are more hits in the upstream box of the possible vertex plane, then the vertex plane candidate moves one plane upstream in the view, and the same VTEST is repeated until the criteria are satisfied.

Now we impose the condition that the vertex hits defined this way in each view should be within 3 PDT planes of each other to be the x and y vertices for the same event. Then the most upstream plane of the X and Y vertex planes is determined to be the vertex plane of the event.

4.3.3 Vertex Fiducial Cut

A neutrino interaction can take place anywhere in the detector. In order to reconstruct the tracks and to make sure that the candidate neutrino events are indeed from the neutrino beam, and not some random cosmic ray or from other neutral particles like neutrons, we need to confine the vertex of the neutrino events into a smaller volume of the detector, the so called *fiducial volume.*

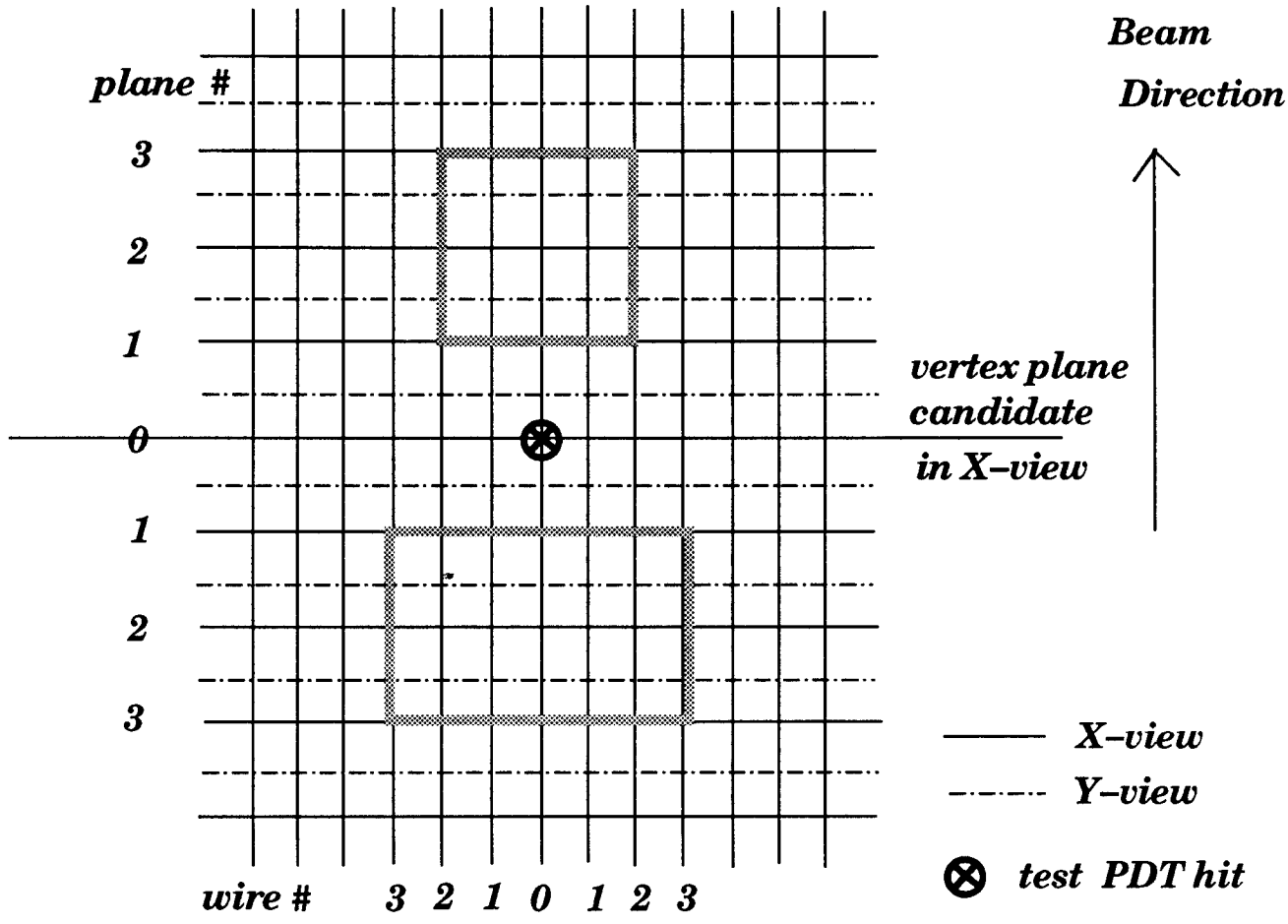

Figure 4.6: Possible vertex test in $x-$view, in routine VTEST

If the found vertex is near the edge of the detector, most likely one of the tracks will leave the detector. In this case, we can not have complete information (energy, momentum, and charge) of the track. We require that the vertex should be at least 4 wires in from the edge of the detector. Out of total 64 wires on a PDT plane, running perpendicular to the beam direction (the X and the Y direction; the wires are numbered from 0 to 63),

$$4 \leq \text{Vertex wire } \# \leq 59$$

If the found vertex is at the very upstream end of the detector, too close to the beam dump, then we do not know if the event is really initiated by a neutrino, since a high energy neutron which is neutral like the neutrino could initiate the reaction. If the found vertex is at the downstream end of the detector, then there is insufficient information from the calorimeter. Without the track informations in the calorimeter, we can not reconstruct tracks in the toroid, since the toroid segmentation is not fine enough to do tracking. As a result, we required the vertex to be within 10 planes from the beginning of the detector and 5 planes from the end of the detector. Out of total 90 planes in the calorimeter (Z direction, or beam direction; from downstream plane to upstream plane, the planes are numbered from 0 to 89),

$$10 \leq \text{Vertex plane } \# \leq 85$$

These fiducial cuts reject about a third of the event sample since,

$$\text{Fiducial factor: } (\frac{56}{64})^2 \times \frac{75}{90} = 64\%$$

4.4 V_PAT2

Now we have found the vertex in V_PAT1. Using this vertex information, the next logical step is to identify two track pattern, determine the track lengths, and apply a track length cut. This is done by the V_PAT2 routine.

4.4.1 Track Related Hits

We first try to find hits which are associated with tracks. Since we know the vertex from V_PAT1, and we know that all the tracks associated with the event should start from this vertex, we can make a topological definition of track related hits as follows. (We are not interested in assigning hits to each track, at this level of analysis, yet.)

If there are hits adjacent to the vertex, then these hits including the vertex hit are classified as event related, since it is very possible that actual vertex is one or two planes upstream of the identified vertex plane, but is not seen in the particular view. Then, the next hits downstream from the vertex are checked to see if they are associated with a track. Upstream hits were considered as random hits which have nothing to do with the actual event, although it is possible to have a couple of hits related to back-scattering particles. In this particular analysis of looking for dimuon events, those upstream hits can be neglected. We first draw a straight line connecting the vertex and a test hit, moving consecutively from the vertex plane to each downstream plane. Then we look for any previously accepted hits as associated with tracks along this line within 2 wire spacings and up to 3 planes upstream of the

plane where the test hit locates. With this method, we find out all the hits which are possibly associated with tracks.

4.4.2 Track Length Determination and Cut

Since we have the hits associated with tracks, we next try to determine the first and second track lengths, and to apply track length cut. For this determination of track lengths, we rely only on the topology of the event, sophisticated track reconstruction is done after manual scanning. To get the track lengths, we consider the X and Y view independently to avoid the confusion arising from overlapping tracks.

From the vertex plane in each view, the first track length is the number of consecutive planes in which the number of hits per plane is ≥ 1, and for the second track, the number of consecutive planes in which the number of hits is ≥ 2. Then we compare the track lengths in each view, and select the track lengths which are longer, since we see two clear tracks in one view, the event is likely to be a two track event, and by doing so, the interesting two track events will be kept even after the track length cut.

In this analysis, we are looking for dimuon events, but most of the events in the initial sample have only one leading track plus some hadronic tracks, or extra hits. So to separate the muon tracks from hadronic tracks we require that the second track (the second longest track) be longer than 24 planes, which is roughly 2 interactions lengths (more when a track is at a wide angle) in the calorimeter.

We have still not done full track reconstruction at this level, but still can still find

out whether the event has a toroid track by looking at the UV planes (this will be described in detail in next chapter) in front of the toroid. For tracks entering the toroid, we counted how many toroid Fe-plates the track passed through and convert to the corresponding number of calorimeter planes, based on the amount of material seen.

We require that the first track (the longest track) length to be $\geq$ 30 planes and the second track length to be $\geq$ 24 planes to accept the event as a two track event.

By this time we have reduced the events to 2,249 for the WBB neutrino data, and 425 for the WBB antineutrino data, 831 for the Charm_MC, 2,119 for the neutrino MC, and 344 for the antineutrino MC (MC, and Charm_MC event numbers are actual (not normalized) numbers in the sample).

4.5 Manual Scan

4.5.1 Manual Scan1

After the program, V_PAT2, the event sample was significantly reduced. Approximately six thousands events, including the WBB data, MC, and Charm_MC for both ν, and $\overline{\nu}$ runs, survived. At this stage we opted for a manual scan to reduce the number of events further, since the size of the event sample was manageable.

The scan consisted of two steps. The first one was to eliminate complicated events picked up in the previous analysis. These are the events with interacting tracks, scattering tracks, and track-like showers.

Interacting tracks are those that develop more than 2 secondary tracks after traveling some distance; topologically it looks like a tree with branches. Scattering tracks are the tracks with a visible kink. Track-like showers are showers which develop more longitudinally than horizontally, so it looks like a track with a few hits around at the first glance. There were also two track events in which one of tracks is clearly a cosmic track or second neutrino interaction in the same frame; one in hundred frames had two neutrino events. The scanning rules were defined, and described in Appendix B.

For the events which passed the first part of manual scan, to understand the characteristics of the events in each sample, we plotted the average number of PDT hits per plane. The distributions of the average number of hits per plane in the first 20 planes for neutrinos and antineutrinos are shown in Figure 4.7 and Figure 4.8 respectively for the WBB data, MC events, and Charm_MC events.

The Charm_MC sample (in Figure 4.7, this is labeled as dimuon MC) shows a cluster around two and three, while both the WBB data and the MC sample show much wider distributions. As an exercise, we have looked at the number of events with the average number of hits per plane less than three ($N_{avg}(PDT) < 3$). There appears to be some excess (several tens of events) in the number of events in the neutrino WBB data when we compare the number with the MC, while there is no such excess in the antineutrino data. This indicates that the Charm_MC events have mostly two track events in the sample, while the WBB data and MC events have many high multiplicity events in the sample. We have looked at parts of these

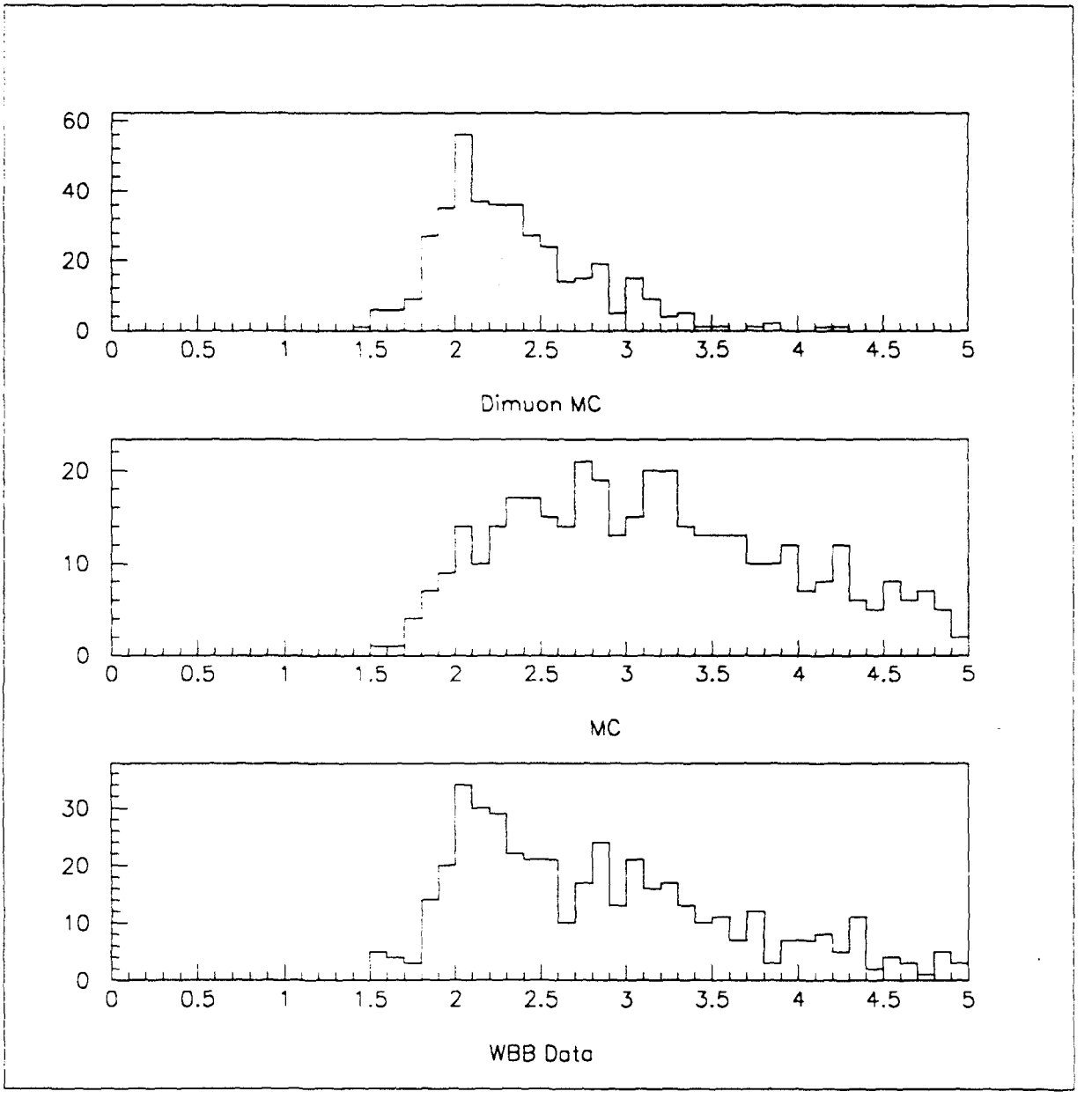

Figure 4.7: After manual scan1 (manual1), average number of PDT hits per plane from the vertex up to 20 planes for $\nu-$events.

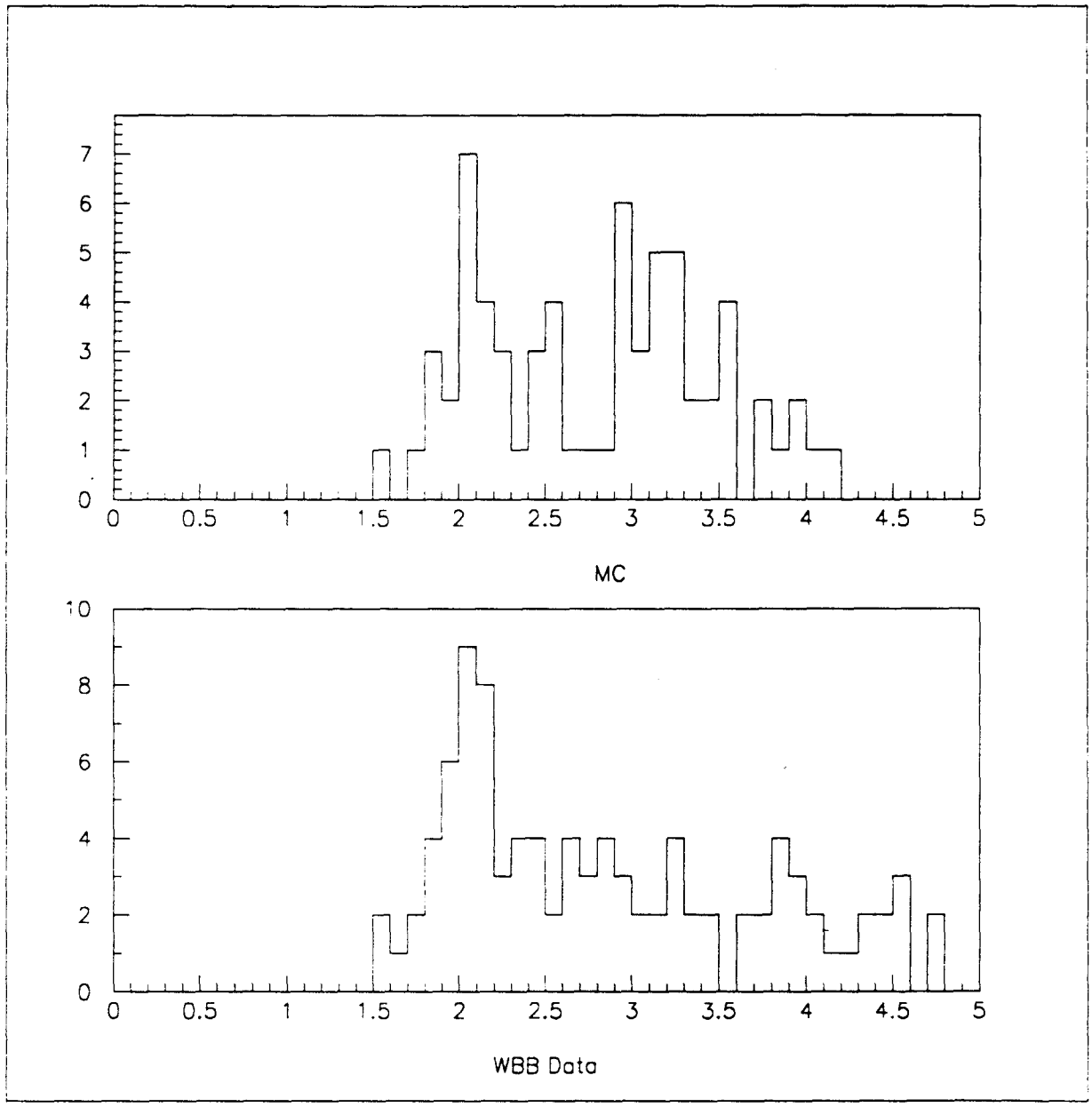

Figure 4.8: After manual scan1 (manual1), average number of PDT hits per plane from the vertex up to 20 planes for $\bar{\nu}$–events.

events after the manual scan1 very carefully, and decided not to use the criteria of $N_{avg}(PDT) < 3$ to select possible dimuon events, although it is appealing to eliminate high multiplicity events. since there are some interesting dimuon events may not pass this criteria. These are the dimuon events crossed by a cosmic ray track or dimuon events with a vertex at the very end of the detector having a very short track length in the calorimeter and other short hadron tracks around, but both tracks going into the toroid. We certainly did not want to lose these types of events.

4.5.2 Manual Scan2

The second part of scan is to get rid of high multiplicity events manually instead of requiring $N_{avg}(PDT) < 3$. In addition, we require that the event should have at least one hit associated with the tracks in the toroid, as this enables us to measure the sign of the track. We also confirm the X and Y vertices of the event found in V_PAT1, and and measure the ending points of the first and second track both in the calorimeter and in the toroid in each view. Now the remaining events after both the manual scan1 and the manual scan2 which have at least one hit in toroid are ready for actual muon track analysis.

All the data reduction is summarized in Table 4.3 and 4.4, and the changes in events in each of the reaction channels in Monte Carlo as we go through successive data reduction stages are summarized in Table 4.5 and 4.6.

	ν - Run			
	WBB Data		Monte Carlo	
	Beam Trig	Free Trig	MC	Charm_MC($\mu^+\mu^-$)
Orig	...	...	(100,000)	[10,000]
EDIT1	...	...	(88,180)	[9,612]
EDIT3	76,302	6,339	76,302 (68,373)	7,806 [7,806]
V_PAT1	22,477	141	31,236 (27,990)	4.697 [4,697]
V_PAT2	2,249	1	2,365 (2,119)	831 [831]
Manual1	454	0	444 (398)	655 [398]
Manual2	217	0	141 (126)	563 [338]

Table 4.3: E776 dimuon analysis data reduction for ν. (In MC column, the numbers are normalized to WBB beam trigger data, the numbers in the parentheses are the actual event numbers analyzed.) Charm_MC shows the acceptance for the dimuon events (the numbers in the brackets are the actual event numbers analyzed).

	$\overline{\nu}$ - Run		
	WBB Data		Monte Carlo
	Beam Trig	Free Trig	MC
Orig	...	...	(30,000)
EDIT1	...	...	(24,587)
EDIT3	22,864	4,913	22,864 (18,828)
V_PAT1	4,131	118	6,545 (5,390)
V_PAT2	425	1	418 (344)
Manual1	101	0	81 (67)
Manual2	42	0	34 (28)

Table 4.4: E776 dimuon analysis data reduction for $\overline{\nu}$. (In MC column, the numbers are normalized to WBB beam trigger data, the numbers in the parentheses are the actual event numbers analyzed.)

	$\overline{\nu}$ - Run		
	WBB Data		Monte Carlo
	Beam Trig	Free Trig	MC
Orig	...	...	(30,000)
EDIT1	...	...	(24,587)
EDIT3	22,864	4,913	22,864 (18,828)
V_PAT1	4,131	118	6,545 (5,390)
V_PAT2	425	1	418 (344)
Manual1	101	0	81 (67)
Manual2	42	0	34 (28)

Table 4.4: E776 dimuon analysis data reduction for $\overline{\nu}$. (In MC column, the numbers are normalized to WBB beam trigger data, the numbers in the parentheses are the actual event numbers analyzed.)

		Charged-Current ν–Int.			Neutral-Current ν–Int.		
	TOTAL	QE	CCSP	CCDIS	ELAS	NCSP	NCDIS
MC_GEN	100,000 (100%)	16,152 (17%)	18,066 (18%)	41,695 (42%)	5,597 (6%)	6,754 (7%)	11,366 (11%)
EDIT1	88,180	14,921	16,907	40,430	1,324	4,108	10,490
EDIT3	68,373	11,772	13,246	32,657	488	2,255	7,955
V_PAT1	27,990	1,415	4,486	18,216	82	375	3,416
V_PAT2	2,119	24	151	1,883	1	5	55
Manual1	398	2	27	367	0	2	0
Manual2	126	1	23	102	0	0	0

Table 4.5: Neutrino MC Events Reduction For Various Reaction Channels. (These numbers are actual, not normalized, event numbers.)

		Charged-Current $\overline{\nu}$–Int.			Neutral-Current $\overline{\nu}$–Int.		
	TOTAL	QE	CCSP	CCDIS	ELAS	NCSP	NCDIS
MC_GEN	30,000 (100%)	7,954 (25%)	6,652 (22%)	7,038 (24%)	2,997 (10%)	2,826 (9%)	2,893 (10%)
EDIT1	24,587	6,940	6,204	6,810	571	1,492	2,570
EDIT3	18,828	5,590	5,007	5,518	157	725	1,831
V_PAT1	5,390	207	1,432	2,981	13	89	628
V_PAT2	344	4	42	291	1	0	6
Manual1	67	0	11	54	0	0	2
Manual2	28	0	9	19	0	0	0

Table 4.6: Antieutrino MC Events Reduction For Various Reaction Channels. (These numbers are actual, not normalized, event numbers.)

Chapter 5

DIMUON ANALYSIS

We now have the potential dimuon events. The dimuon candidates are the events which have two tracks which originate in the fiducial volume and penetrate enough of toroid spectrometer, so that we can identify them as muons and measure their momentum and sign.

We have generated two sets of Monte Carlo events. The first one is to understand the backgrounds to the signal we are looking for. In what follows, we refer to the background study Monte Carlo events as just MC events. They are QE, CCSP, CCDIS, EL, NCSP, and NCDIS, which are all described in detail in Chapter 3, in the section on charm-nonproducing neutrino-nucleon interactions. We also generated the opposite sign dimuon events from the muonic decay of exclusive Λ_c^+ production. In what follows, we will call these events Charm_MC events. At this stage of the analysis, we have both the MC and the Charm_MC generated events as well as the real data which all samples have passed through the previous data reduction filter programs described earlier. We process all these events from the different samples

through the analysis in the same way as follows.

5.1 Track Reconstruction in the Calorimeter

A muon track in our E776 detector is a straight line with relatively few missing hits, in contrast to an electron, or π^0 which develop showers in the calorimeter.

We wanted to find all the hits associated with the track. They were all the hits within two wire spacings of the straight line connecting the beginning and end point of the track. The vertex point found in V_PAT1 was confirmed, and the end points of the two tracks were measured in the manual scanning. Using all these hits, we did a least squares analysis and to find the parameters of the track. They are the length of each track, and the direction cosines by combining separately measured slopes in both X and Y views. The energy loss in the calorimeter is determined by the length of the track in the calorimeter.

This completes the track reconstruction for tracks which are contained in the calorimeter. For tracks entering the toroid, we want to measure their momentum and sign.

5.2 Track Matching in X and Y View

Before we attempt to fit tracks in the toroid, we ask if the two tracks in the X and Y views are matched properly. For a long single track, it is easy to match by comparing the beginning and end point of the track in both views. However, when we have two tracks originating at the same vertex and ending at the end of calorimeter detector,

we have a built-in ambiguity. Remember we are interested in only those events in which both tracks penetrate part of the toroid. Fortunately, we have two PDT planes just before the toroid and after the calorimeter, which were rotated +/− 45 degrees with respect to the rest of the detector. These two planes are called U and V planes, hereafter. By extrapolating the hits in the calorimeter to the UV planes and matching two tracks, we were able to remove the ambiguity.

$$\begin{pmatrix} U \\ V \end{pmatrix} = \begin{pmatrix} cos\varphi & sin\varphi \\ -sin\varphi & cos\varphi \end{pmatrix} \begin{pmatrix} x \\ y \end{pmatrix} = \frac{1}{\sqrt{2}} \begin{pmatrix} x+y \\ -x+y \end{pmatrix} \tag{5.1}$$

To be more specific, we use the following procedures to match two tracks in space.

1. In each view, we calculated the X and Y positions of the track by extrapolating straight lines to the Z-positions of UV planes.

2. Using equation 5.1, we calculated the U and V positions.

3. If a toroid PDT hit lies within 2 PDT widths on either the U or V plane, then we conclude that the tracks are correctly matched.

5.3 Track Reconstruction in the Toroid

There are three kind of tracks in the toroid. The first kind is one which stops in the toroid. For this kind of track, we know the energy of the track from the range measurement assuming it is a muon. In what follows, we call these tracks stopping muons. The second kind is the one which exits the side of the toroid. We do not

analyze these leaving tracks. The third kind is the one which passes through the toroid. We call these tracks penetrating muons.

For the stopping muons, we required that there should be 5 or more hits associated with each track in the toroid. This ensures at least two or more hits in each X and Y view of toroid, i.e. the same requirement as penetrating the first two 5″ steel plates in toroid. This in practice made a momentum cut of 1 GeV/c. For both stopping and penetrating muons, we carried out a χ^2analysis.

A charged particle traveling inside the toroid experiences not only bending due to the magnetic field, but also multiple scattering which makes the particle go through a random zigzag path. However, the most probable path remains the one without multiple scattering. For a given charge and momentum assumption, and with direction cosines and position where the track enters the toroid determined from the calorimeter track reconstruction, we can predict the path of the track due to magnetic bending in the toroid. The correct charge and momentum can be found by searching for a χ^2 minimum within an allowed kinematical range, i.e. P_{min} and P_{max}. For the stopping muon tracks, we know the momentum range of the track P_{min} and P_{max} by its range in toroid. We get P_{min} by considering the material the track passes through up to the last hit in the toroid, and P_{max} by considering one more slab of material from the last hit to take it into account that the track may stop in the next steel slab. For a penetrating muon, we can only know that its actual momentum is bigger than P_{min} by the total range in the toroid, so for P_{max}, we have assigned a very large

value, since the correct momentum should be found by χ^2analysis.

We calculated the multiple scattering angles (Eq. A.1) in each slab of toroid steel plate using the average momentum in the slab of material, taking into account the air gap spacings between each steel plates.

Then, we can calculate the symmetric multiple scattering error matrix as follows (detailed derivation and definitions of all the notations are in Appendix A):

For i $\leq$ j,

$$M_{ij} = \sum_{k=1}^{i} \theta_k^2 (\frac{L_k^2}{3} + \frac{L_k}{2}(z_{ki} + z_{kj}) + z_{ki} z_{kj}) + \theta_i a_i \theta_j a_j I_{ij} + \sigma_0^2 I_{ij}$$

where the summation is over each PDT plane in the toroid, and i, and j refers each PDT plane.

Using the error matrix above, the χ^2 is

$$\chi^2_{p,charge} = \sum_{i=1}^{N} \sum_{j=1}^{N} (x_i^m - x_i^p) M_{ij}^{-1} (x_j^m - x_j^p)$$

where the summation is over the N PDT planes the track passes through in the toroid.

For each charge assumption, we can find the minimum χ^2 and corresponding momentum. If the χ^2 minimum is found only for one charge assumption, we decide that the charge assumed is the actual charge for the track. If χ^2 minimum is found for both negative and positive charge assumptions, then they are compared, and we select the charge of the track which gives the smaller χ^2 value. How well this method works has been checked with Monte Carlo, and next section discusses the results in detail.

5.4 Analysis Results

We generated 240K CCDIS (ν) Monte Carlo events, which is equivalent to four times the WBB data sample. In addition, we generated 100K Monte Carlo events, which contains 16K QE, 18K CCSP, 7K NCSP, 11K NCDIS, and 6K EL events, which is approximately equivalent to our data sample together with 40K CCDIS events (this 40K is part of 240K CCDIS sample). (In all the data reduction tables, the MC event numbers are from this 100K Monte Carlo sample, to compare with WBB data.) We expect all of our backgrounds to come from CCDIS but we generated others to make sure.

First we want to know how well we were doing the sign determination. Here we have a total of 126 neutrino and 28 antineutrino induced Monte Carlo events (event numbers here are the actual (not normalized) event numbers in the sample).

χ^2 distributions for μ^- and μ^+ Monte Carlo events are shown in Figure 5.1, and Figure 5.2 before applying any χ^2 cuts; the μ^- sample ($\nu-$run: μ^- is focused in the toroid) contains 87 events, while the μ^+ sample ($\overline{\nu}-$run: μ^+ is focused in the toroid) contains only 24 events.

We decided to make a χ^2 per degree of freedom cut of 10 based on these χ^2 distributions. The number of muon tracks passing successive cuts are summarized in Table 5.1 for the muon tracks, and the number of hadron tracks faking muon tracks in the same passing successive cuts are summarized in Table5.2 and Table 5.3 for the neutrino and antineutrino Monte Carlo samples respectively. With the final χ^2 cut

of 10, we can convince ourselves that we never make a mistake in sign determination of muon tracks at least with these statistics. With these cuts, as Table 5.2 indicates, only a couple of remaining hadron tracks faking muons survived in the sample.

The reconstructed energy distributions of the final sign determined muon tracks are shown in Figure 5.3 for Monte Carlo μ^- tracks and in Figure 5.4 for Monte Carlo μ^+ tracks. The reconstructed momentum compared to the Monte Carlo generated momentum is shown in the form $(1/p_{recon} - 1/p_{mc})/(1/p_{mc})$ which is a good way of understanding toroid momentum resolution (Figure 5.5 and Figure 5.6 for Monte Carlo μ^- and μ^+ respectively).

We have also examined individual muon tracks (regardless of any other tracks in the same event) in the dimuon candidate sample of Charm_MC. Before applying the χ^2 cut, 160 μ^- tracks, and 83 μ^+ tracks exist in the sample (again the event numbers here are not normalized). Corresponding tables are Table 5.4 for the muon tracks, and Table 5.5 for the hadronic tracks faking muon tracks in the same sample.

With a χ^2 cut of 10, we tell the sign of the track correctly for only 98 % of 138 surviving μ^- tracks, and for only 93 % of 69 surviving tracks in the Charm_MC dimuon sample. This has to do with the fact that for the opposite sign dimuon events, two tracks coexist in the toroid, the μ^- is focused and the μ^+ is defocused, while muons from single muon events are always focused and the average energy of the muon is in general higher compared to muons in dimuon events, consequently tracks in dimuon events leave fewer hits in the toroid.

Ultimately, we want to know how many opposite sign dimuon events are in the actual data and Monte Carlo, and the efficiency of finding them.

The same set of successive cuts were applied to each of the tracks in the WBB data, the MC event, and Charm_MC event samples. The results are summarized in Tables 5.8, 5.9, and 5.10. Here the MC event sample has been normalized to the WBB data sample.

The Charm_MC event sample has been normalized to the original 10,000 dimuon events generated (since the entire Charm_MC sample was not fully manually scanned). The MC event sample is to study background, so the normalized MC event numbers can be compared to WBB data event numbers. The Charm_MC event sample is to study actual acceptance of dimuon events from the actual analysis, so the acceptance of each level can be read off by dividing the normalized event numbers by original 10,000 dimuon events.

Based on this study, we expect 1.1 opposite sign ($\mu^-\mu^+$) and 1.1 same sign ($\mu^-\mu^-$) dimuon events from charm-nonproducing neutrino interactions. The χ^2 distributions for both the μ^- and μ^+ of the opposite sign dimuon events and energy distributions for events with $\chi^2 < 10$ found for each sample are shown in Figure 5.7. For the MC event sample, the events from the additional 200,000 CCDIS events were included.

Opposite sign dimuon events from the Charm_MC (Table 5.10 for normalized, and Table 5.7 for the actual number of events in the sample) reveals that we have 18.3 events $\mu^+\mu^-$ Charm_MC events with 3.3 $\mu^-\mu^-$ same sign background Charm_MC

events.

	ν - **Run** (μ^- focused)			$\overline{\nu}$ - **Run** (μ^+ focused)		
	μ^-			μ^+		
		Charge Found			Charge Found	
Cuts	Total	Right(-)	Wrong(+)	Total	Wrong (-)	Right(+)
Before Cut	126	–	–	28	–	–
N>4 & E>1GeV	92	83	9	25	1	24
Exit Cut	87	80	7	24	1	23
$\chi^2 < 20$	73	71	2	21	0	21
$\chi^2 < 10$	66	66	0	20	0	20

Table 5.1: MC: Sign determination of single μ^- and μ^+ tracks in the dimuon candidate background MC sample (both ν and $\overline{\nu}$ runs)

	ν - **Run**(μ^- focused): Among 126 MC events								
	π^-			π^+			proton		
Cuts	Total	(-)	(+)	Total	(-)	(+)	Total	(-)	(+)
Before cut	21	–	–	55	–	–	46	–	–
N>4 & E>1GeV	2	2	0	3	2	1	1	1	0
Exit Cut	2	2	0	3	2	1	1	1	0
$\chi^2 < 20$	2	2	0	3	2	1	1	1	0
$\chi^2 < 10$	2	2	0	3	2	1	0	0	0

Table 5.2: MC: Sign determination of hadron tracks faking muon tracks in the dimuon candidate background MC sample (ν–run)

	$\overline{\nu}$ - **Run**(μ^+ focused): Among 28 MC events								
	π^-			π^+			proton		
Cuts	Total	(-)	(+)	Total	(-)	(+)	Total	(-)	(+)
Before cut	15	–	–	1	–	–	11	–	–
N>4 & E>1GeV	0	0	0	0	0	0	0	0	0

Table 5.3: MC: Sign determination of hadron tracks faking muon tracks in the dimuon candidate background MC sample ($\overline{\nu}$–run)

	ν - **Run** (μ^- focused, μ^+ defocused) Among 338 $\mu^-\mu^+$ Charm_MC events					
	μ^-			μ^+		
		Charge Found			Charge Found	
Cuts	Total	Right(-)	Wrong(+)	Total	Wrong (-)	Right(+)
Before Cut	332	—	—	328	-	-
N>4 & E>1GeV	166	158	8	93	12	81
Exit Cut	160	154	6	83	9	74
$\chi^2 < 20$	152	147	5	75	7	68
$\chi^2 < 10$	138	135	3	69	5	64

Table 5.4: Charm_MC (Opposite sign dimuon events from Λ_c^+ decay): Sign determination of muon tracks in dimuon candidate charm_MC sample ($\nu-$run)

	ν - **Run** (μ^- focused, μ^+ defocused) Among 338 $\mu^-\mu^+$ Charm_MC events								
	π^-			π^+			proton		
Cuts	Total	(-)	(+)	Total	(-)	(+)	Total	(-)	(+)
Before cut	1	-	-	0	-	-	15	-	-
N>4 & E>1GeV	0	0	0	0	0	0	1	1	0
Exit Cut	0	0	0	0	0	0	1	1	0
$\chi^2 < 20$	0	0	0	0	0	0	1	1	0
$\chi^2 < 10$	0	0	0	0	0	0	0	0	0

Table 5.5: Charm_MC (Opposite sign dimuon events from Λ_c^+ decay): Sign determination of hadron tracks faking muon tracks in the dimuon candidate charm_MC sample ($\nu-$run)

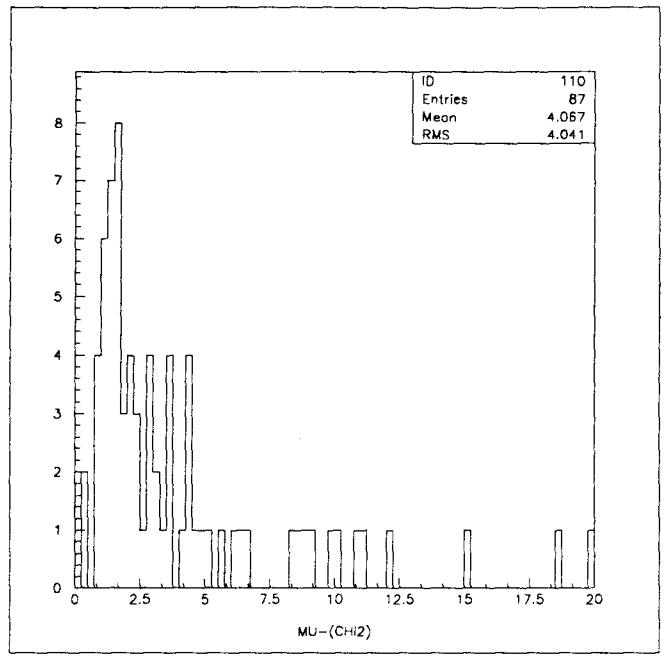

Figure 5.1: Monte-Carlo μ^-: χ^2 distribution before applying χ^2 cut

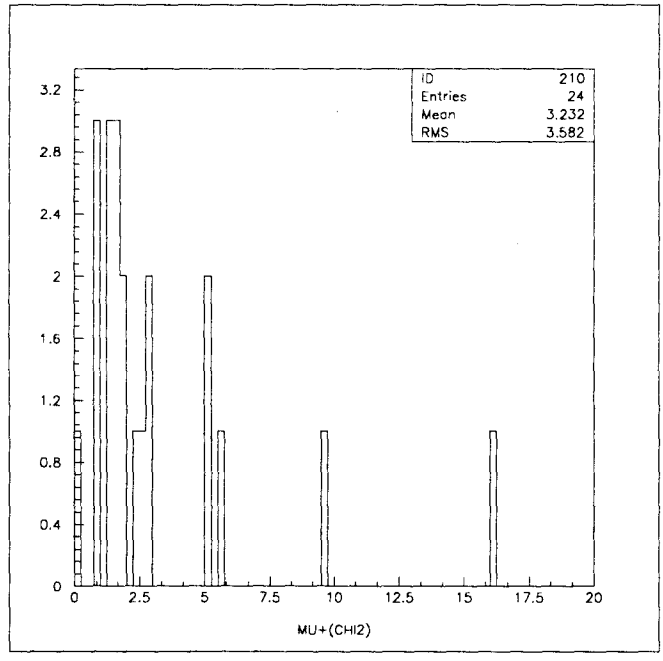

Figure 5.2: Monte-Carlo μ^+: χ^2 distribution before applying χ^2 cut

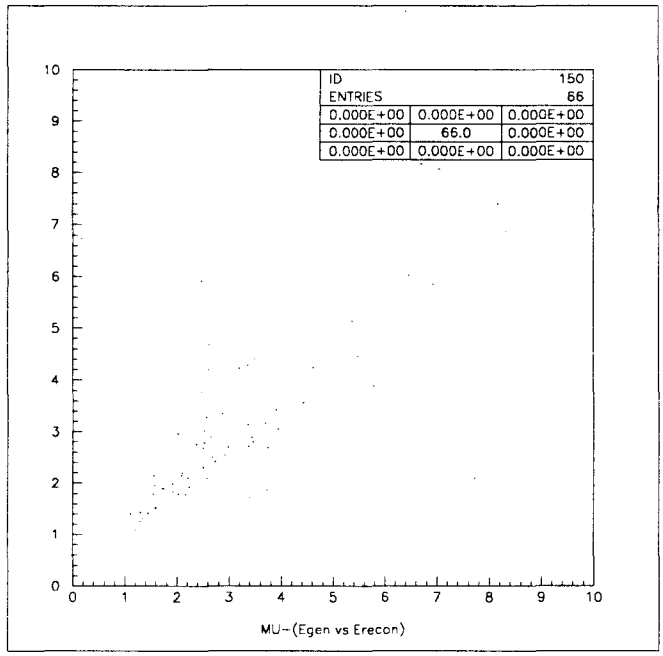

Figure 5.3: Monte-Carlo μ^-: Energy reconstruction for μ^- after χ^2 cut (E in GeV)

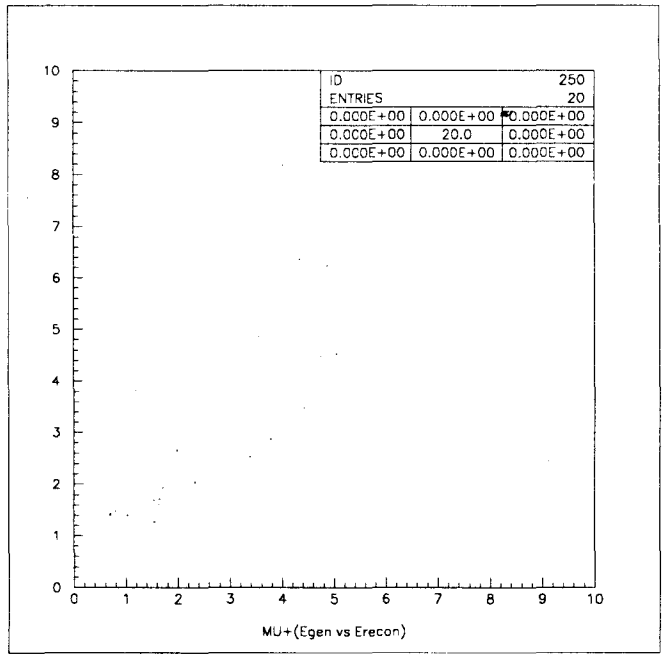

Figure 5.4: Monte-Carlo μ^+: Energy reconstruction for μ^+ after χ^2 cut (E in GeV)

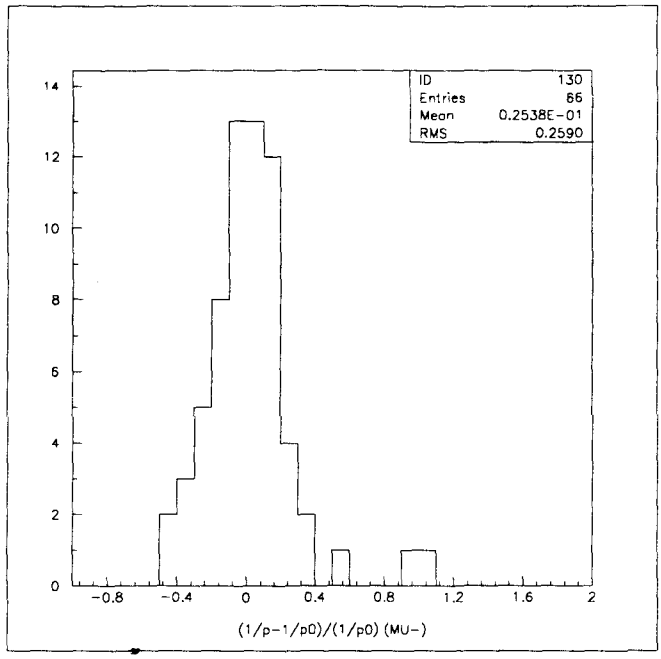

Figure 5.5: Monte-Carlo μ^- : $(1/P_{RECON} - 1/P_{MC})/(1/P_{MC})$

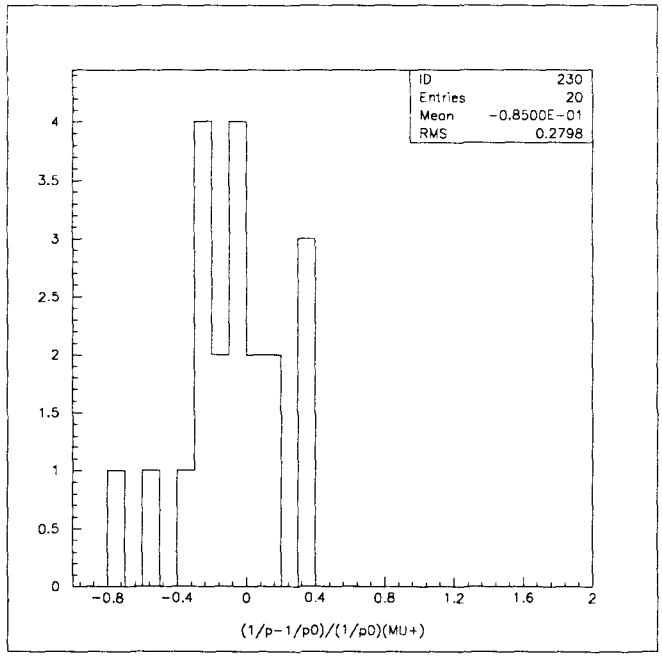

Figure 5.6: Monte-Carlo μ^+ : $(1/P_{RECON} - 1/P_{MC})/(1/P_{MC})$

	MC: (ν)		
Cuts	$\mu^+\mu^-$	$\mu^+\mu^+$	$\mu^-\mu^-$
Before cut	5	1	10
N>4 & E>1GeV	1	0	2
Exit Cut	1	0	2
$\chi^2 < 20$	1	0	1
$\chi^2 < 10$	1	0	1

Table 5.6: MC: Dimuon events(ν): not normalized

	Charm_MC: From Λ_c^+ decay (ν)		
Cuts	$\mu^+\mu^-$	$\mu^+\mu^+$	$\mu^-\mu^-$
Before cut	43	4	12
N>4 & E>1GeV	24	1	3
Exit Cut	21	1	2
$\chi^2 < 20$	17	1	2
$\chi^2 < 10$	11	0	2

Table 5.7: Charm_MC: Dimuon events(ν): not normalized

	WBB DATA(ν)		
Cuts	$\mu^+\mu^-$	$\mu^+\mu^+$	$\mu^-\mu^-$
Before cut	13	0	7
N>4 & E>1GeV	6	0	3
Exit Cut	3	0	3
$\chi^2 < 20$	3	0	2
$\chi^2 < 10$	2	0	1

Table 5.8: WBB DATA: Dimuon events(ν)

	MC: (ν)		
Cuts	$\mu^+\mu^-$	$\mu^+\mu^+$	$\mu^-\mu^-$
Before cut	5.6	1.1	11.2
N>4 & E>1GeV	1.1	0	2.2
Exit Cut	1.1	0	2.2
$\chi^2 < 20$	1.1	0	1.1
$\chi^2 < 10$	1.1	0	1.1

Table 5.9: MC: Dimuon events(ν): normalized to WBB DATA

	Charm_MC: From Λ_c^+ decay(ν)		
Cuts	$\mu^+\mu^-$	$\mu^+\mu^+$	$\mu^-\mu^-$
Before cut	71.6	6.7	20.0
N>4 & E>1GeV	40.0	1.7	5.0
Exit Cut	35.0	1.7	3.3
$\chi^2 < 20$	28.3	1.7	3.3
$\chi^2 < 10$	18.3	0	3.3

Table 5.10: Charm_MC: Dimuon events(ν): normalized to 10,000 Original Dimuon events

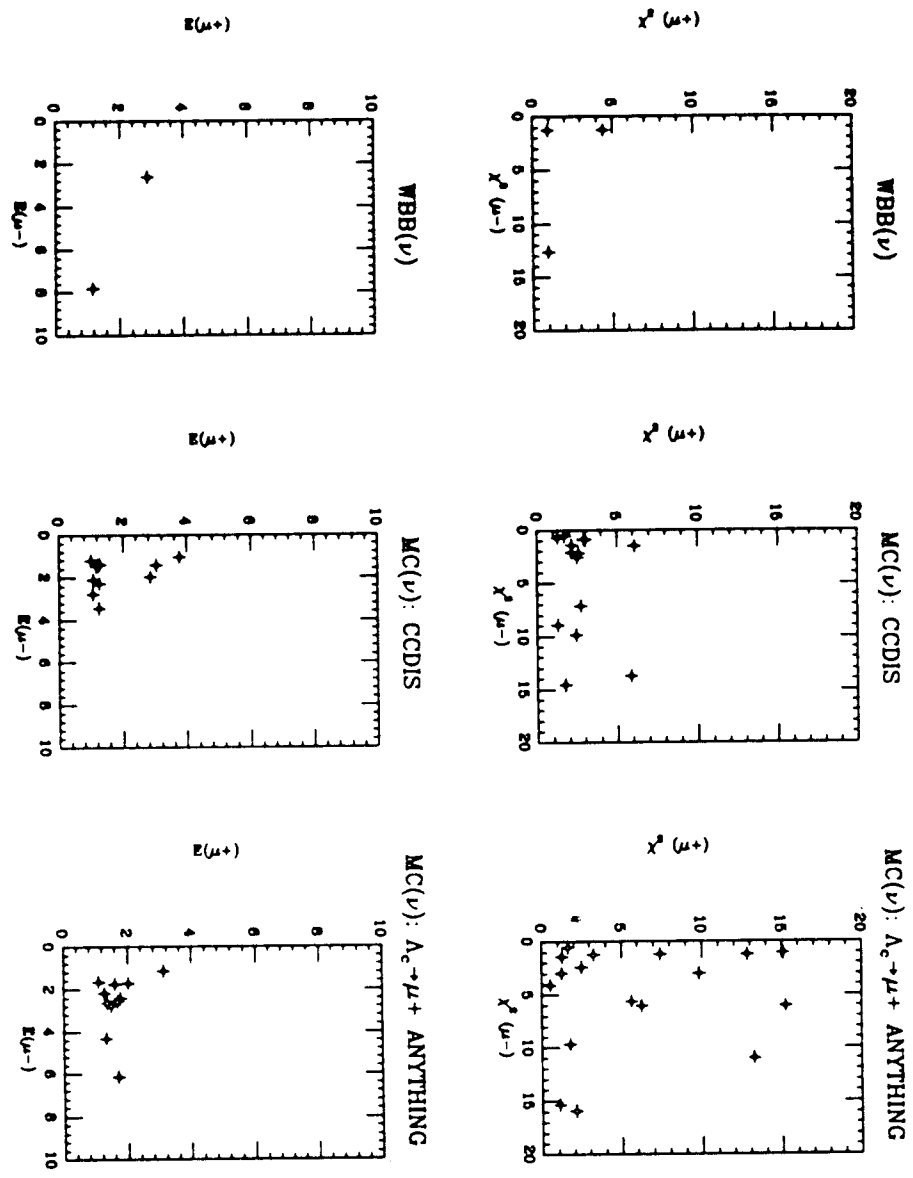

Figure 5.7: Candidates for opposite sign dimuon events: for WBB data, MC CCDIS, and Charm_MC Dimuon events from Λ_c^+ decay. Shown figures are χ^2 for μ^- and μ^+. Energy distribution for μ^- and μ^- is after χ^2 cut of 10 is applied. (E in GeV)

5.5 Opposite Sign Dimuon Events MC Study

After making all the cuts, the acceptance of Monte Carlo opposite sign dimuon events is only 0.18%. To understand why the acceptance of dimuon events is so small, we've closely examined 1,000 Charm_MC opposite sign dimuon events. For Λ_c^+ producing neutrinos, the neutrino energy distribution is shown in Figure 5.8. The corresponding muon energy distributions are shown in Figures 5.9 and Figure 5.10. The μ^- which originates from the lepton vertex has a higher energy ($\overline{E}_{\mu^-} = 1$ GeV) than that of the μ^+ from the charmed particle decay ($\overline{E}_{\mu^+} = 0.8$ GeV) in general.

We've applied a 1 GeV energy cut, and angle cut of $\cos\theta > 0.8$ in the actual dimuon data analysis. We applied the same cuts on the MC data to study how the efficiency changes, and the followings is the results.

- A($E_{\mu^-} > 1$ GeV) = 33.2 %
- A($E_{\mu^+} > 1$ GeV) = 29.4 %
- A($E_{\mu^-} > 1$ GeV & $E_{\mu^+} > 1$ GeV) = 9.8 %
- A($E_{\mu^-} > 1$ GeV & $cos\theta_{\mu^-} > 0.8$) = 30.6 %

  $\overline{E}_{\mu^-} = 2.2$ GeV after cut
- A($E_{\mu^+} > 1$ GeV & $cos\theta_{\mu^+} > 0.8$) = 26.4 %

  $\overline{E}_{\mu^+} = 1.4$ GeV after cut
- For both tracks,

$$A(E_{\mu^-} > 1 \text{ GeV } \& \ cos\theta_{\mu^-} > 0.8 \ \& \ E_{\mu^+} > 1 \text{ GeV } \& \ cos\theta_{\mu^+} > 0.8) = 7.6 \ \%$$

where A is the Monte Carlo acceptance.

The acceptance for Monte Carlo opposite sign dimuon events after making energy and angle cuts on both tracks on MC values is only 7.6 %. With a vertex fiducial factor of 64 %, the acceptance at this level becomes

$$7.6\% \times 64\% = 4.9\%$$

which can be compared to the 5.6 % for the Charm_MC dimuon events sample after the manual scan, and before the full dimuon sign analysis.

For us to determine the sign of both tracks with confidence, based on the MC single muon track study, a minimum of 5 toroid hits on each track (i.e. a track traversing minimum of 2 toroid Fe-plates) was required. Only 7 % of those dimuon events satisfy this condition for both tracks, while 18 % of them, neither track satisfies the condition, and for the rest of events only one track satisfies the condition. Thus, at this level an overall Monte Carlo acceptance becomes

$$4.9\% \times 7\% = 0.34\%$$

Further cuts which require the track not to exit the side of the toroid and have a good χ^2 value, were made afterwards. This explains why acceptance for dimuon events is so small, and the final acceptance for opposite sign dimuon events of 0.18% is reasonable for the given beam energy and detector.

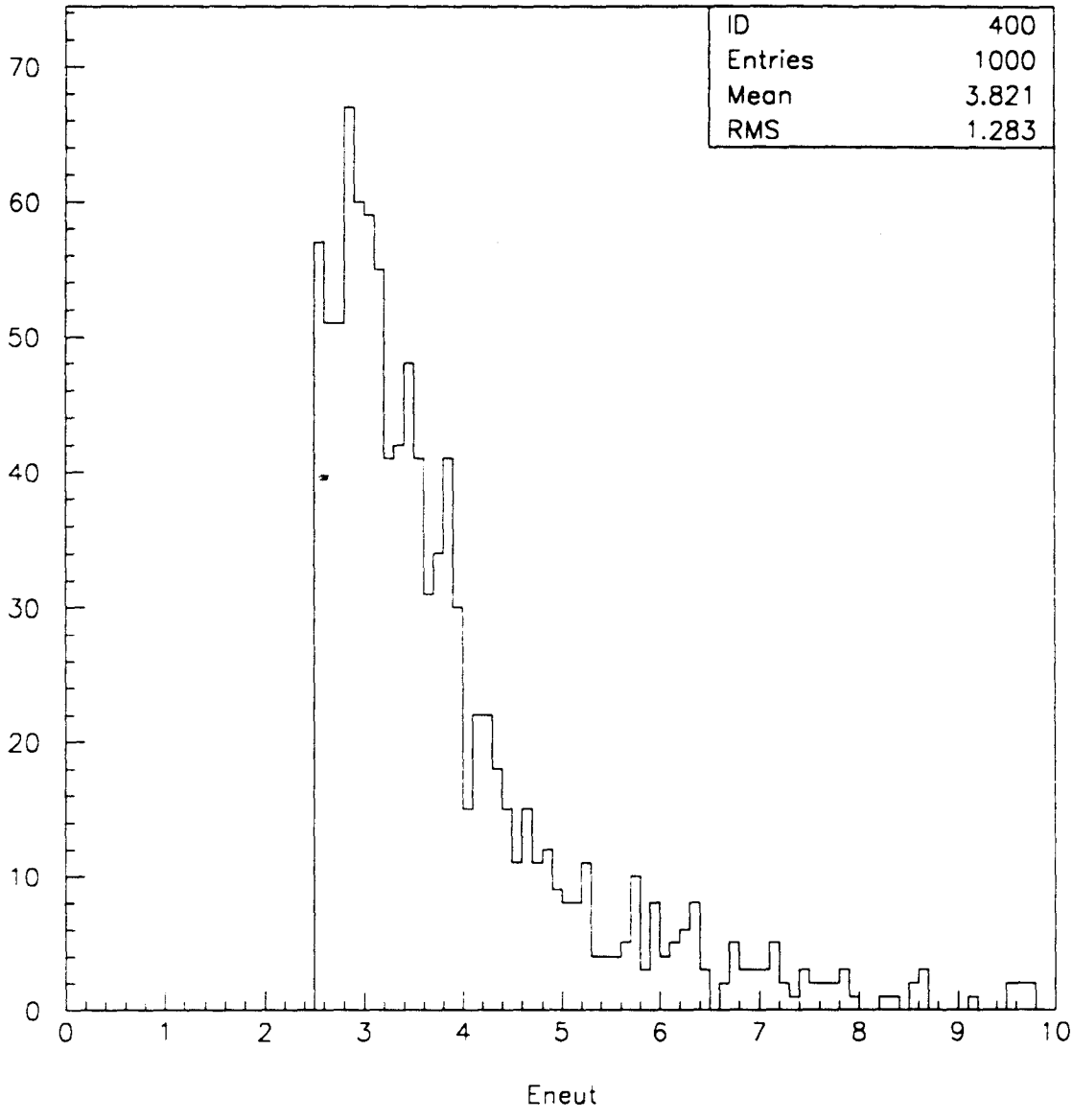

Figure 5.8: Monte-Carlo Dimuon Generator: E_ν distribution of neutrinos which can produce Λ_c^+ particles (E in GeV)

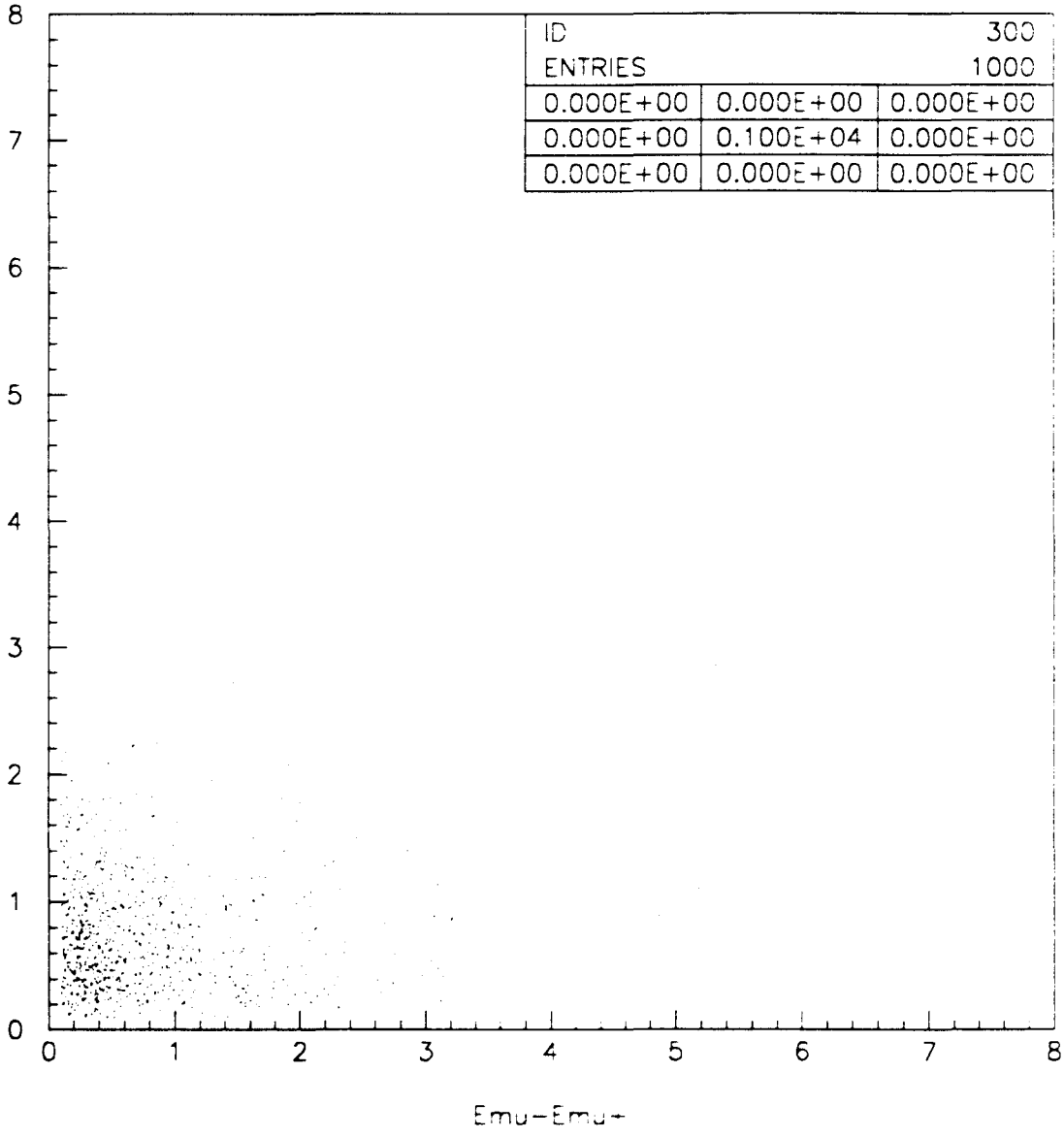

Figure 5.9: Monte-Carlo Dimuon Generator: distribution of E_{μ^-} (horizontal axis) and E_{μ^+} (vertical axis) for dimuon events from Λ_c^+ decay (E in GeV)

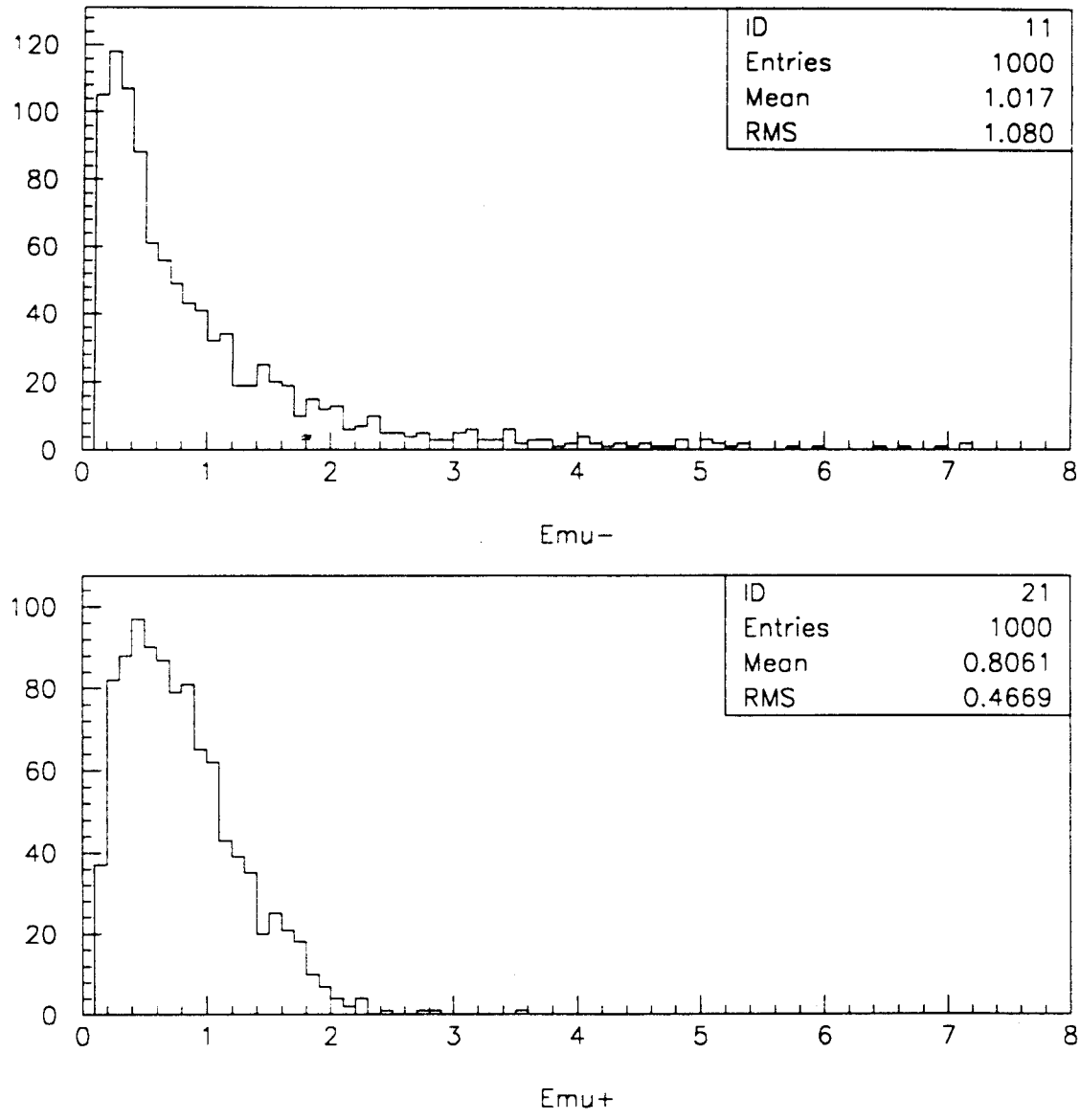

Figure 5.10: Monte-Carlo Dimuon Generator: distribution of E_{μ^-} and E_{μ^+} respectively in dimuon events from Λ_c^+ decay (E in GeV)

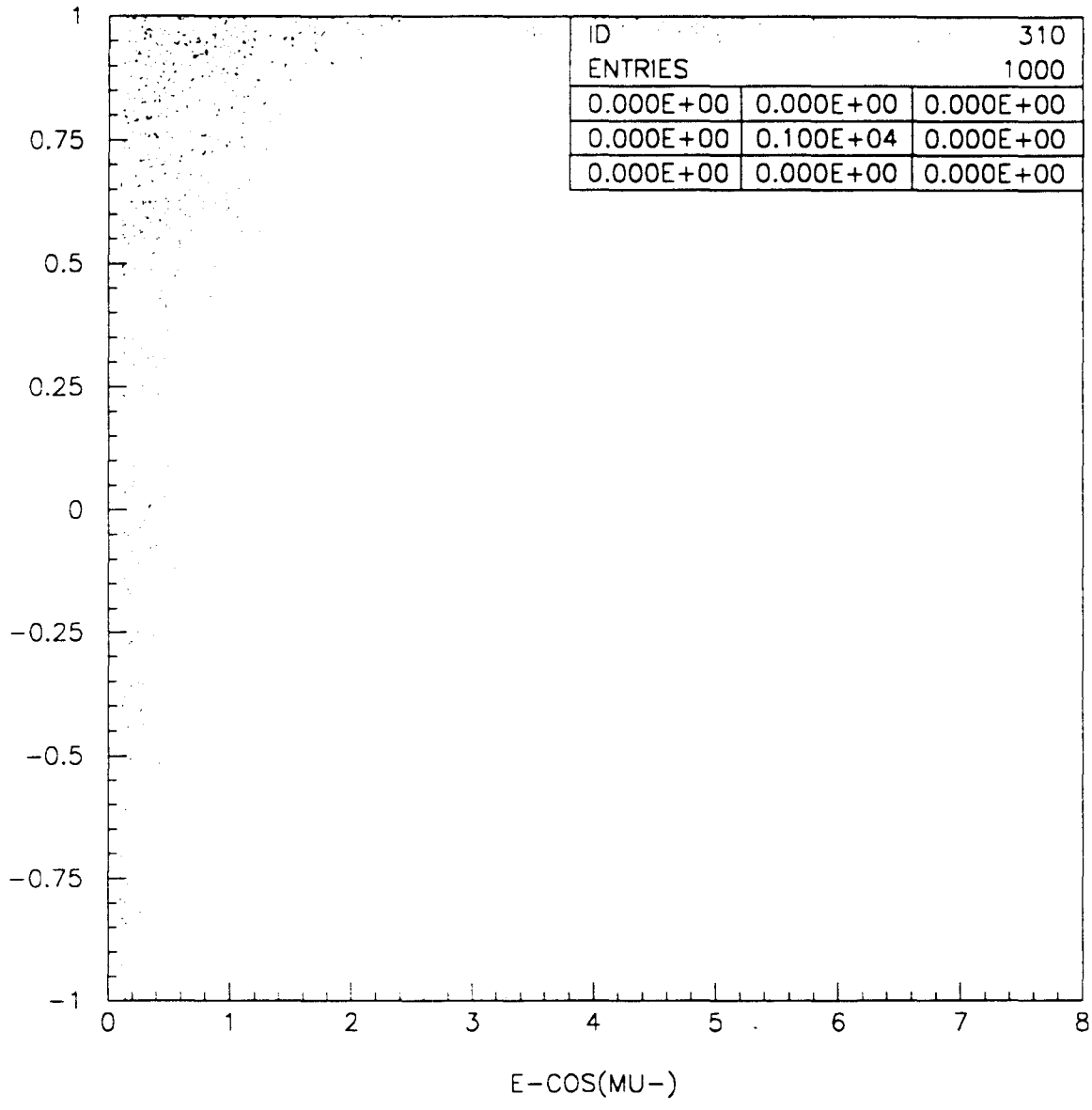

Figure 5.11: Monte-Carlo Dimuon Generator: distribution of E_{μ^-} (in GeV: horizontal axis) and $cos\theta_{\mu^-}$ (vertical axis) in dimuon events from Λ_c^+ decay

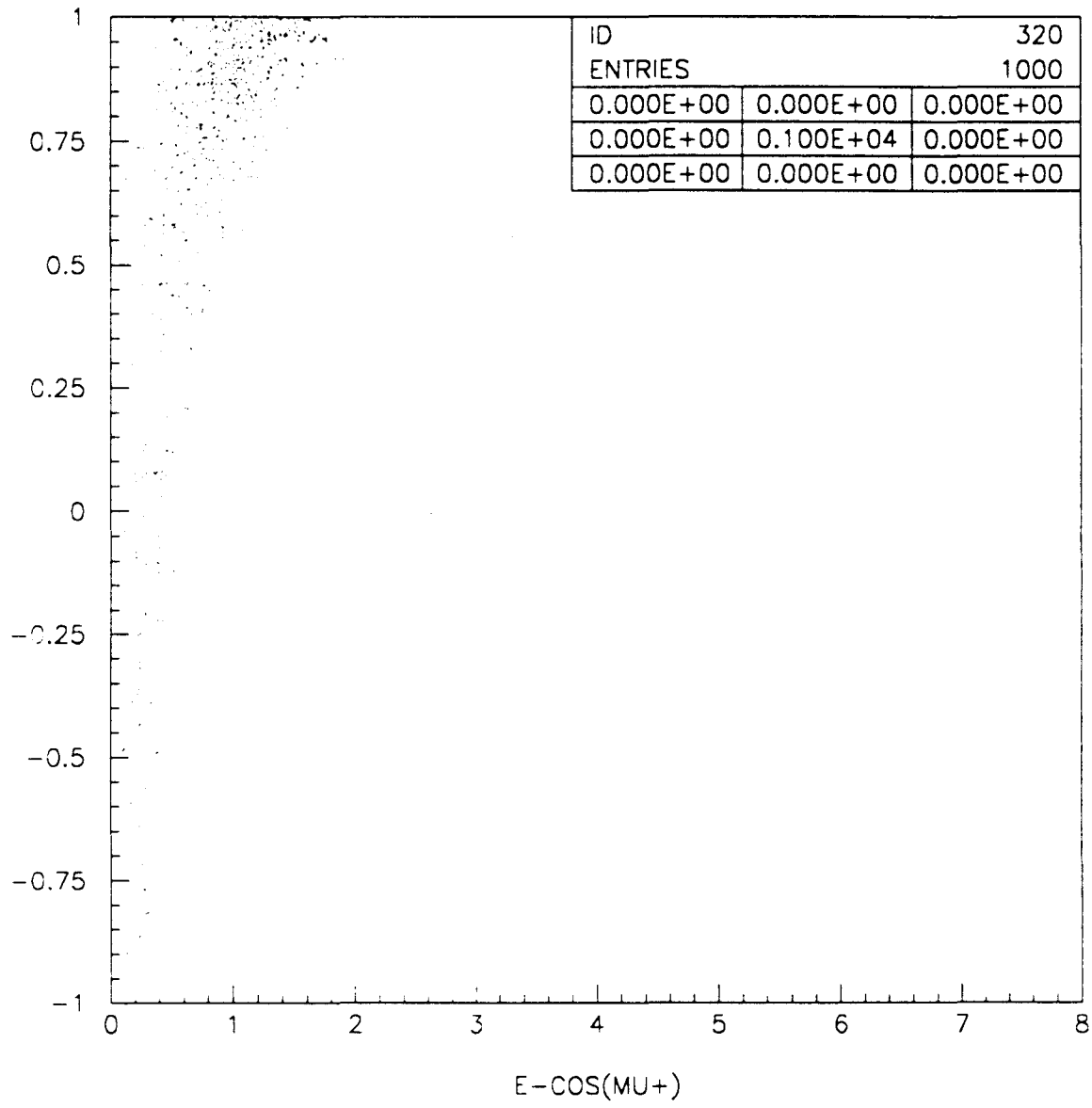

Figure 5.12: Monte-Carlo Dimuon Generator: distribution of $E_{\mu+}$ (in GeV: horizontal axis) and $cos\theta_{\mu+}$ (vertical axis) in dimuon events from Λ_c^+ decay

5.6 Expected Number of Events in E776

The number of events expected in the experiment can be estimated in general as follows. (A schematic diagram of the detector is shown in Figure 5.13).

$$\begin{aligned} N_{expected} = \ & \{\int \frac{dN}{dE}\sigma(E)dE\} \times 10^{-4} \times (\#\text{ of POT}) \\ & \times(\#\text{ of Nucleons in detector}) \end{aligned} \tag{5.2}$$

$\frac{dN}{dE}$: Neutrino energy flux $(1/m^2/POT/GeV)$

$\sigma(E)$: Neutrino interaction cross section (cm^2)

dE : Neutrino energy : integration variable (GeV)

10^{-4} : Unit factor (m^2/cm^2)

Number of Nucleons in detector can be calculated as

$$=\rho\ N_A\ l\ A$$

=(Detector mass in gram) $\cdot N_A$

- ρ : Density of material (g/cm^3)
- l : Length (cm)
- A : Cross-sectional area perpendicular to the beam direction (cm^2)
- N_A : Avogadro's Number

Defining F as

$$F \equiv \int \frac{dN}{dE}\sigma(E)dE \tag{5.3}$$

the number of expected events for E776 can be calculated as

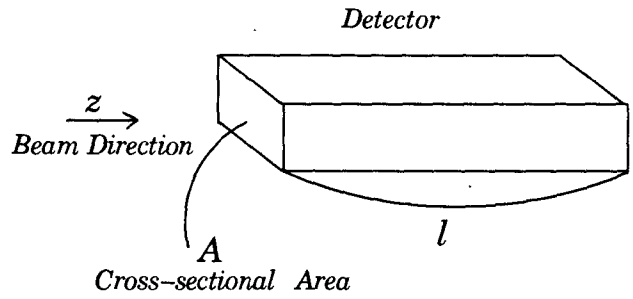

Figure 5.13: Schematic diagram of detector describing parameters used in event rate calculation

$$N_{expected} = F \times 10^{-4} \times (\#\text{ of POT}) \times \text{ (Detector mass in gram)} \times N_A \qquad (5.4)$$

Then, respectively for $\nu-$run and $\overline{\nu}-$run:

$$\begin{aligned} N_{expected}(\nu - run) &= F \times 10^{-4} \times (1.43 \times 10^{19} POT) \times (236 \times 10^{6}) \times (6 \times 10^{23}) \\ &= F \times 2.025 \times 10^{47} \end{aligned} \qquad (5.5)$$

$$\begin{aligned} N_{expected}(\overline{\nu} - run) &= F \times 10^{-4} \times (1.55 \times 10^{19} POT) \times (236 \times 10^{6}) \times (6 \times 10^{23}) \\ &= F \times 2.195 \times 10^{47} \end{aligned} \qquad (5.6)$$

Using this formula and the calculated cross sections, the anticipated Λ_c^+, Σ_c^{++}, Σ_c^+, and D_c event rates with respect to the neutrino beam energy were calculated, and are shown in Figure 5.14. The event rate for Σ_c^+ can be read off from Σ_c^{++} just by dividing by two.

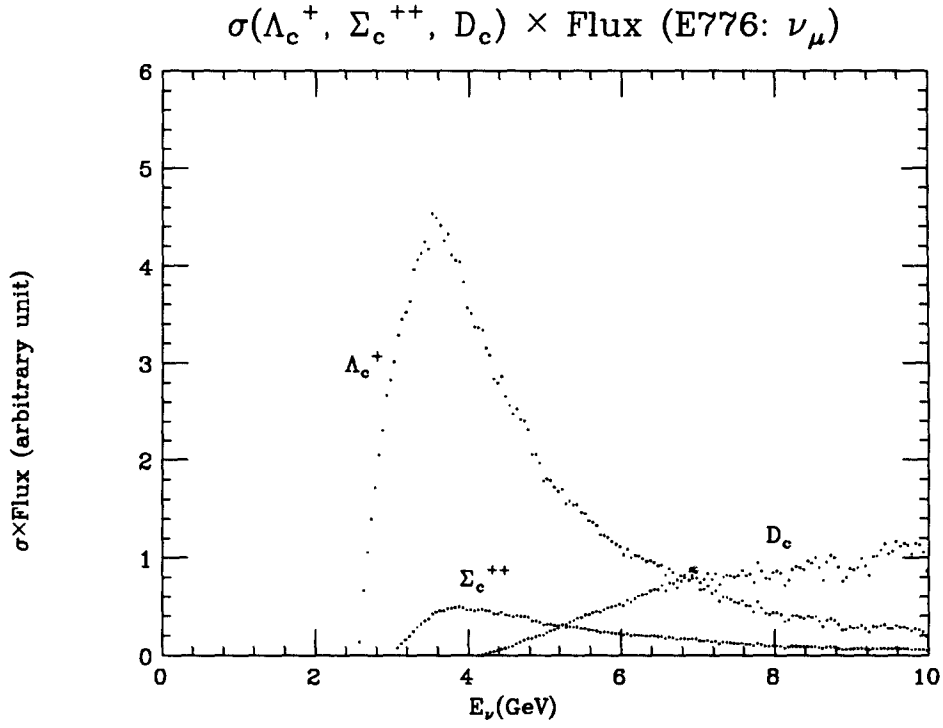

Figure 5.14: Event rate estimate for charmed particles in E776 $\nu-$Run. Event rate for Σ_c^+ can be read off Σ_c^{++} just by scaling down by half.

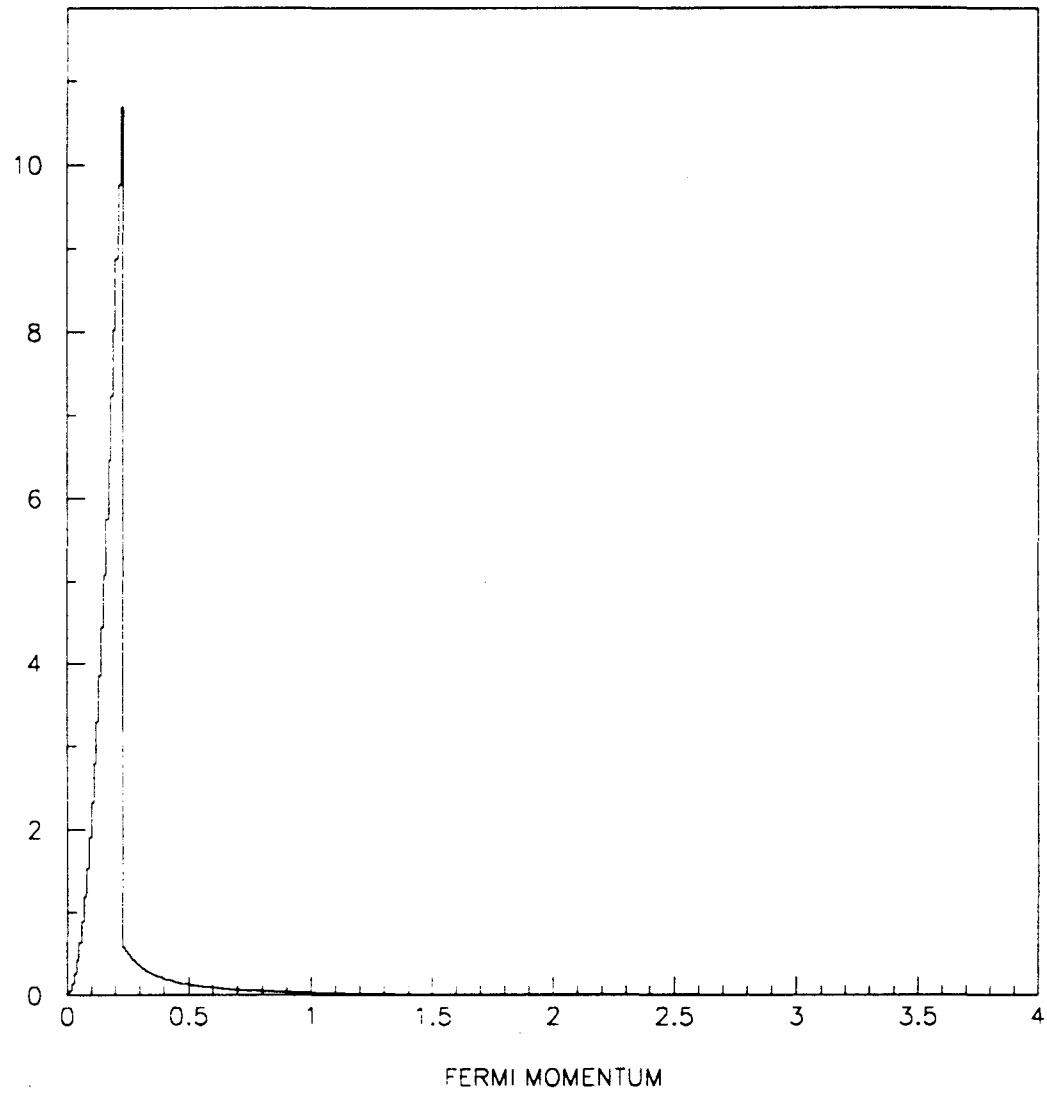

Figure 5.15: Fermi momentum (in GeV) inside the nucleus

Because we are near the threshold of charmed baryons, it is important to incorporate the Fermi motion of the target nucleon. It is well known that an individual nucleon inside nucleus is not exactly at rest, instead it has a certain momentum (called *Fermi Momentum*), according to the distribution(Figure 5.15) which follows a power law of p^2 up to about 230 MeV/c with a very little above this cut-off momentum. So the actual event rate estimate as well as the MC generator should take this Fermi momentum into account. Particularly for exclusive charmed particle production in E776, the neutrino beam energy populates even below the lowest charmed particle threshold, so even a little bit of Fermi momentum around threshold can make the total CM-energy high enough to produce charmed particles.

The actual event rate for a given neutrino energy was obtained statistically as follows.

1. Generate Fermi momentum many times according to the distribution shown in Figure 5.15.

2. Calculate average CM-energy.

3. Calculate new neutrino energy corresponding to the same average CM-energy assuming the target nucleon is at rest.

4. Pick cross section for the new calculated neutrino energy.

Event rate estimates for possible charmed particle reactions are listed in Table 5.11 along with the $F-$value (defined in equation 5.3). With Fermi momentum included,

the expected event rate increased a little over 10%.

		F(w/Fermi)	F(w/o Fermi)	$N_{expected}$ (w/o Fermi)
$QE\nu_\mu$	μ^-	1.256×10^{-5}	1.238×10^{-5}	25,070
ν_μ–induced	Λ_c^+	2.453×10^{-7}	2.189×10^{-7}	443
Exclusive	Σ_c^{++}	3.352×10^{-8}	3.008×10^{-8}	61
charm Production	Σ_c^+	1.676×10^{-8}	1.504×10^{-8}	31
ν_μ Deep-inelastic	D_c^*	$\cdots$	7.555×10^{-8}	166
$\overline{\nu}_\mu$ Deep-inelastic	$\overline{D}_c$	$\cdots$	2.927×10^{-9}	6

Table 5.11: Event rate estimate for the exclusive production of charmed particles in E776, where $F \equiv \int \frac{dN}{dE}\sigma(E)dE$ (in unit of $10^{-38}/POT$)

In Table 5.11, exclusive single pion charmed baryon production was not included due to the uncertainty involved in the calculation of cross sections, but a reasonable assumption is that it is similar to QE charmed baryon production.

The dimuon rate can be obtained by multiplying by the muon branching ratios of these charmed particles. However these leptonic branching ratios are not that well understood, or experimentally confirmed. The inclusive branching ratio of charmed baryons to muons is predicted to be less than 5%, and that of charmed mesons to be about 10%.

If we use these numbers, and assume that the single pion charmed production rate is the same as that of QE charmed production, then we would have 70 opposite sign dimuon events (with Fermi momentum, about 77 events) if the acceptance is 100%.

Chapter 6

CONCLUSION

The data from the E776 WBB ν_μ run has been analyzed for the presence of dimuon events. This analysis yielded 2 $\mu^-\mu^+$ events and 1 $\mu^-\mu^-$ event in the data sample. Based on Monte Carlo studies, the background rate is expected to be 1.1 $\mu^-\mu^+$ and 1.1 $\mu^-\mu^-$ events. The number of events observed is consistent with the background rate expected, and we conclude that there is no evidence for observation of quasi elastic charm production. The expected number of events based on the current theoretical value for cross section times branching ratio for the $\Lambda_c^+ \rightarrow \mu^+ X$ and the neutrino flux and the acceptance is 0.14.

These results contradict the earlier published results of dilepton production in ν interaction by Bross [22]. Based on those results, a signal of 30 dimuon events should have been observed.

Bibliography

[1] W. Pauli. *Proc. VII Solvay Congress, Brussels.* Gauthier-Villars, 1933.

[2] C. S. Wu and S. A. Moszkowski. *Beta Decay.* Interscience Publishers, 1966.

[3] J. Chadwick. Possible existence of a neutron. *Nature*, **129**:312, 1932.

[4] E. Fermi. *Z. Phys.*, **88**:161, 1934.

[5] F. Reines and C. L. Cowen. *Phys. Rev.*, **113**:273, 1959.

[6] K. Goulianos L.M. Lederman N.Mistry M. Schwartz G. Danby, J. M. Gaillard and J. Steinberger. *Phys. Rev. Lett.*, **9**:36, 1962.

[7] F. J. Hasert *et al. Phys. Lett.*, **46B**:138, 1973.

[8] A. Benvenuti *et al. Phys. Rev. Lett.*, **32**:800, 1974.

[9] B. Aubert *et al. Phys. Lett.*, **32**:1454, 1974.

[10] S. J. Barish*et al. Phys. Rev. Lett.*, **33**:448, 1974.

[11] B. C. Barish *et al. Proc. of the Seventeenth International Conference on High Energy Physics*, 1974.

[12] W. Lee *et al.* *Proc. of the Seventeenth International Conference on High Energy Physics*, 1974.

[13] J. Iliopoulos S.L. Glashow and L. Maiani. *Phys. Rev.*, **D2**:1285, 1970.

[14] J. E. Augustin *et al.* Discovery of a narrow resonance in e^+e^- annihilation. *Phys. Rev. Lett.*, **33**:1406, 1974.

[15] J. J. Aubert *et al.* Experimental observation of a heavy particle j. *Phys. Rev. Lett.*, **33**:1404, 1974.

[16] B. Knapp *et al.* *Phys. Rev. Lett.*, **34**:1040, 1975.

[17] E.D. Commins and P.H. Bucksbaum. *Weak Interactions of Leptons and Quarks.* Cambridge U. Press, 1983.

[18] M. Kobayashi and T. Maskawa. *Prog. Theor. Phys.*, **49**:652, 1973.

[19] S. R. Klein. Charmed baryons: A new laboratory for charm studies. *Internal report of Boston University (BU-HEP-89-16)*, 1989.

[20] E. G. Cazzolio *et al.* *Phys. Rev. Lett.*, **34**:1125, 1975.

[21] N. Ushida *et al.* Experimental observation of a heavy particle j. *Phys. Lett.*, **206**:380, 1988.

[22] A. Bross. PhD thesis, University of Illinois, 1977.

[23] N. Kondakis. PhD thesis, Columbia University, 1988.

[24] B. C. Rubin. PhD thesis, Columbia University, 1989.

[25] H. J. Moehring J. Ranft P. A. Arino, A. Fasso and G. R. Stevenson. A long writeup of the fluka86 program. *CERN Divisional Report TIS-RP/168*, 1986.

[26] J. Ranft and S. Ritter. Particle production in hadron-nucleus collisions in a multi-chain fragmentation model. *Z. Phys.*, **C20**:347, 1983.

[27] J. Ranft and S. Ritter. The monte carlo codes nucevt and hadevt to simulate hadron production in hadron-nucleus and hadron-hadron collisions. *CERN Internal Report TIS-RP/IR/83-23*, 1983.

[28] K. Haensgen and J. Ranft. Hadronic event generation for hadron cascade calculations and detector simulation: Inelastic hadron-nucleon collisions at energies below 5 *gev*. *Nucl. Sci. Eng.*, **88**:537, 1984.

[29] R. Hagedorn H. Grote and J. Ranft. Atlas of particle spectra. *CERN report*, 1970.

[30] J. R. Sanford and C. L. Wang. Empirical formulars for particle production in p-be collisions between 10 and 35 bev/c. *BNL Report No. 11479*, 1967.

[31] L. Borodovsky. PhD thesis, Columbia University, 1991.

[32] G. Sullivan. PhD thesis, University of Illinois, 1990.

[33] J. F. Krizmanic. PhD thesis, The Johns Hopkins University, 1989.

[34] C. Y. Chi. PhD thesis, Columbia University, 1988.

[35] C. H. Llewellyn Smith. Neutrino reactions at accelerator energies. *Phys. Report*, **3C**:261, 1972.

[36] Deiter Rein and Lalit M. Sehgal. *Ann. of Phys.*, **133**:79–153, 1981.

[37] Deiter Rein and Lalit M. Sehgal. *Nucl. Phys.*, **B223**:29, 1983.

[38] S. Drell. Lepton-hadron scattering. *Proc. of the Nineteenth SLAC Summer Institute on Particle Physics*, page 41, 1991.

[39] F. Sciulli. Lepton-hadron scattering. *Proc. of the Nineteenth SLAC Summer Institute on Particle Physics*, 1991.

[40] P. G. Reutens. PhD thesis, The University of Chicago, 1986.

[41] Benjamin W. Lee *et al.* Estimates of charm production in exclusive neutrino reactions. *Phys. Rev. D*, **13**:2539, 1976.

[42] H. Georgi and H. D. Politzer. *Phys. Rev.*, **D14**:1829, 1976.

[43] R. M. Barnett. *Phys. Rev. Lett.*, **36**:1163, 1976.

[44] S. A. Rabinowitz. PhD thesis, Columbia University, 1992.

[45] L. Chichura. PhD thesis, The Johns Hopkins University, 1989.

[46] Hideo Hiyayama Walter R. Nelson and David W.O. Rodgers. The *egs*4 code system. *SLAC Report No. 265*, 1985.

[47] W. A. Lyle. PhD thesis, The Johns Hopkins University, 1989.

[48] American Physical Society. Review of particle properties. *Phys. Rev.*, **D45**, 1992.

Appendix A

MUON TRACK FITTING IN THE TOROID

When a charged particle travels through material, it not only loses energy by dE/dX, but also suffers repeated elastic Coulomb Scatterings from nuclei and atomic electrons in the material. The particle thus follows a random zigzag path as it goes through the material.

Although the mean path remains the same as the incident particle direction, any individual particles experience the deflection from the original direction due to the net angle of successive small angle scatterings. This gets more complicated for a charged particle passing through a toroid, since the magnetic field inside the toroid forces the track to bend depending on its charge, momentum and position.

Therefore, it is very important to understand this multiple Coulomb scattering in the medium and to put this effect properly into the error matrix, in addition to the energy loss in the medium and bending in the toroid, in the χ^2 - minimization calculation to find the track momentum and to determine the charge of the track.

A.1 Multiple Scattering

The multiple scattering angle, the net deflection angle after a number of independent scatterings, can be obtained by considering the probability distribution of small angle single scatterings. (A Coulomb scattering has an angular dependence of $1/\sin^4(\frac{\theta}{2})$, so a charged particle is much more likely to undergo a small angle scattering than a larger one.)

In the Gaussian Approximation of such a probability distribution and further refined by the empirical formula, the projected RMS MULTIPLE SCATTERING ANGLE is estimated to be [48]:

$$\sqrt{<\theta^2>} = \frac{13.6MeV}{\beta cp} z \sqrt{\frac{x}{X_0}} [1 + 0.038 ln(\frac{x}{X})] \qquad \text{(A.1)}$$

where

p = momentum in MeV/c

βc = velocity

z = the charge number of the incident particle

x = path length in the medium

X_0 = radiation length of the medium in cm

In this approximation, $\theta^2_{space} \approx (\theta^2_{plane,x} + \theta^2_{plane,y})$, where $\theta_{plane,x}$ and $\theta_{plane,y}$ are independent and identically distributed. The projected RMS multiple scattering angle, θ^{rms}_{plane}, which is given by the Eq. A.1 is related to the space angle in the following way [48].

$$\theta_0 \stackrel{\text{def}}{=} \theta^{rms}_{plane} = \frac{1}{\sqrt{2}}\theta^{rms}_{space} \tag{A.2}$$

As is shown in the formula, the multiple scattering effect gets large and important particularly in a high Z material, where radiation length is small, and when the momentum of the particle is small.

In the E776 experiment, the toroid is made of iron, with a radiation length of only 1.76 *cm*, small compared to the thickness of each plate which is 5 inches (12.7 *cm*), or 7 inches (17.78 *cm*). This results in a multiple scattering angle of about 2.5 degree for an 1 GeV muon after going through one 5 inch toroid plate.

What we measure in our experiment is the track positions between the toroid plates, so any lateral displacement caused by this multiple scattering needs to be understood, and is known to be related to the multiple scattering angle so that [48]

$$< \delta^2 > = \frac{1}{3}x^2\theta_0^2 \tag{A.3}$$

$$< \psi^2 > = \frac{1}{3}\theta_0^2 \tag{A.4}$$

$$< \theta\delta > = \frac{1}{2}x\theta_0^2 \tag{A.5}$$

where 'x' is the thickness of the medium the particle travels through, 'θ' is the projected RMS multiple scattering angle in plane, 'δ' is the displacement due to θ, and

'ψ' can be understood as a corresponding average angle which is related to δ, $\delta \sim x\psi$.

A.2 Magnetic Bending in the Toroid

To predict the most probable path of a charged track in the toroid, bending arising from the magnetic field inside the toroid should be taken into account. This is straight forward to calculate once the magnetic field inside the toroid, the momentum, the direction, and the charge of the incident particle are known.

The magnetic field in the toroid is fairly uniform and has no dependence on azimuthal angle φ. In the E776 experiment, a very careful measurement was done to prove this is the case. An actual survey showed a slight dependence on the radial position, R, of the magnetic field, and this has been taken care of in the simulation.

The magnetic bending angle in the uniform magnetic field after a charged particle has passed through a distance l, is given by:

$$p\theta_{bending} = 0.3Bl \tag{A.6}$$

where

p = momentum in GeV/c

B = magnetic field in kG

l = the distance traveled in magnetic field in cm

A.3 Multiple Scattering Error Matrix

In general, a toroid is made of certain number of toroidal plates and in between there is a device which measures the position of the passing track locates. Mechanically there must be some space for this device between the toroid plates, and this gap introduces more lateral displacement due to multiple scattering in the position measurement. The measuring device in E776 experiment is the PDT(Proportional Drift Tubes), the thin enclosure of the PDT is made of aluminum and the inside is filled with gas; overall the radiation length of this PDT planes is so small compared to that of the toroid, it can be treated as an air gap.

Figure A.1 describes the parameters used in forming the error matrix due to multiple scattering.

Displacements at each plane where measurement of position is made are:

$$\begin{aligned}
\Delta_1 &= \delta_1 + a_1\theta_1 \\
\Delta_2 &= (\Delta_1 - a_1\theta_1) + (A_1 + L_2)\theta_1 + \delta_2 + a_2\theta_2 \\
&= (\delta_1 + \delta_2) + (A_1 + L_2)\theta_1 + a_2\theta_2 \\
\Delta_3 &= (\Delta_2 - a_2\theta_2) + (A_2 + L_3)(\theta_1 + \theta_2) + \delta_3 + a_3\theta_3 \\
&= (\delta_1 + \delta_2 + \delta_3) + (A_1 + A_2 + L_1 + L_2)\theta_1 + (A_2 + L_3)\theta_2 + a_3\theta_3 \\
&\vdots
\end{aligned}$$

As one can see from this formula, downstream of the toroid, the multiple scattering

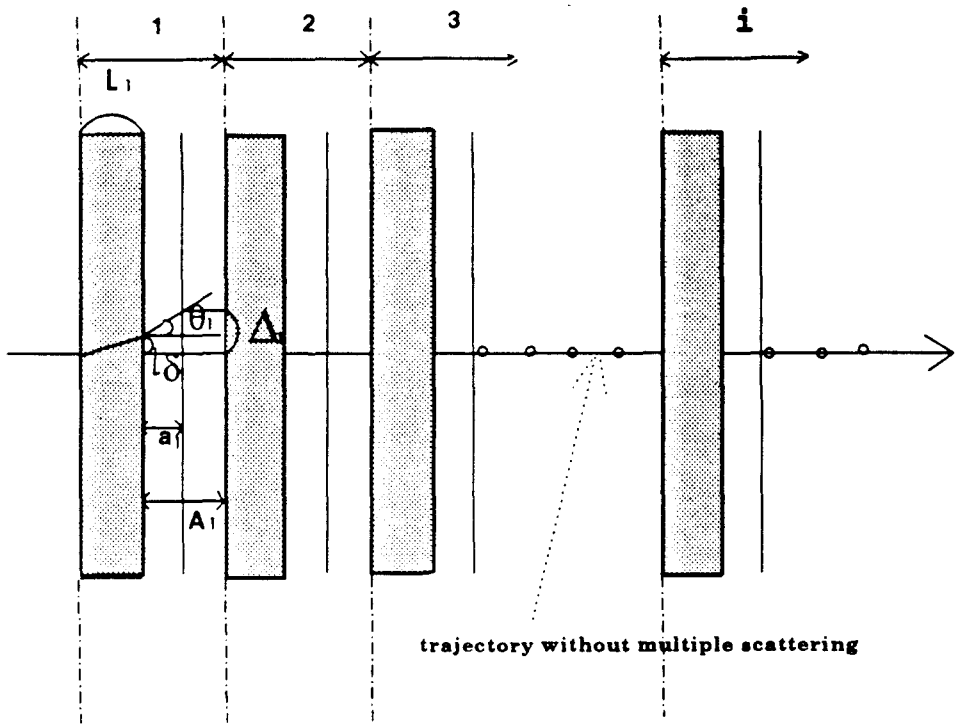

multiple scattering medium

θ_i multiple scattering angle due to i_th medium

δ_i displacement due to θ_i

Δ_i displacement on i_th plane

a_i distance from medium to measuring plane

A_i distance between media

Figure A.1: Multiple scattering parameters

effect gets bigger and bigger since earlier multiple scattering effects multiplicate as the particle passes more material, and the particle loses energy along the way, making the multiple scattering angle itself bigger. In general, Δ_i can be written as:

$$\begin{aligned}\Delta_i &= \sum_{k=1}^{i}\delta_i + \sum_{k=1}^{i-1}\theta_k \sum_{m=k+1}^{i} L_m + \sum_{k=1}^{i-1}\theta_k \sum_{m=k}^{i-1} A_m + \theta_i a_i \\ &= \sum_{k=1}^{i}\delta_i + \sum_{k=1}^{i-1}\theta_k l_{ki} + \sum_{k=1}^{i-1}\theta_k A_{ki} + \theta_i a_i\end{aligned}$$

Here l_{ki} and A_{ki} are defined as:

$$\begin{aligned}l_{ki} &\stackrel{\text{def}}{=} \sum_{m=k+1}^{i} L_m \\ A_{ki} &\stackrel{\text{def}}{=} \sum_{m=k}^{i-1} A_m\end{aligned}$$

Using the fact, $l_{ii} = A_{ii} = 0$, Δ_i can be expressed as:

$$\Delta_i = \sum_{k=1}^{i}(\delta_k + \theta_k l_{ki} + \theta_k A_{ki}) + \theta_i a_i$$

We define further z_{ki} as:

$$z_{ki} \stackrel{\text{def}}{=} l_{ki} + A_{ki}$$

Then displacement at plane i is written in a simpler form,

$$\Delta_i = \sum_{k=1}^{i}(\delta_k + \theta_k z_{ki}) + \theta_i a_i \qquad \text{(A.7)}$$

The multiple scattering error matrix, M_{ij} is,

$$\begin{aligned} M_{ij} &= < (x_i^m - x_i^p)(x_j^m - x_j^p) > \\ &= < \Delta_i \Delta_j > \\ &= < (\sum_{k=1}^{i}(\delta_k + \theta_k z_{ki}) + \theta_i a_i)(\sum_{l=1}^{j}(\delta_l + \theta_l z_{lj}) + \theta_j a_j) > \end{aligned}$$

where x_i^m, x_i^p are measured and predicted positions on the i^{th} plane.

$$\begin{aligned} M_{ij} = < & (\sum_{k=1}^{i}(\delta_k + \theta_k z_{ki})(\sum_{l=1}^{j}(\delta_l + \theta_l z_{lj}) \\ & + \theta_i a_i(\sum_{l=1}^{j}(\delta_l + \theta_l z_{lj}) \\ & + \theta_j a_j(\sum_{k=1}^{i}(\delta_k + \theta_k z_{ki}) \\ & + \theta_i \theta_j a_i a_j > \end{aligned}$$

Note that M_{ij} is a symmetric matrix. And $< \theta >= 0$, and $< \delta >= 0$, while θ^{rms}, and δ^{rms} are not zero. Considering $i \leq j$,

$$M_{ij} =< \sum_{k=1}^{i}(\delta_k^2 + \delta_k \theta_k (z_{ki} + z_{kj}) + \theta_k^2 z_{ki} z_{kj}) + \theta_i a_i \theta_j a_j >$$

Substituting the lateral displacement formula introduced in the multiple scattering section, we can finally get the expression,

$$M_{ij} = \sum_{k=1}^{i} \theta_k^2 (\frac{L_k^2}{3} + \frac{L_k}{2}(z_{ki} + z_{kj}) + z_{ki} z_{kj}) + \theta_i a_i \theta_j a_j I_{ij} \qquad \text{(A.8)}$$

where I_{ij} is an $ij-$component of the identity matrix.

Combining the intrinsic resolution of the PDT σ_0,

$$M_{ij} = \sum_{k=1}^{i} \theta_k^2 (\frac{L_k^2}{3} + \frac{L_k}{2}(z_{ki} + z_{kj}) + z_{ki} z_{kj}) + \theta_i a_i \theta_j a_j I_{ij} + \sigma_0^2 I_{ij} \qquad (A.9)$$

This is a symmetric error matrix, which the diagonal elements represent the variances while the off-diagonal elements represent the covariances. If there is no multiple scattering, then the matrix will be reduced to a diagonal matrix.

In the case of toroid tracking, it becomes a non-linear χ^2- minimization problem, due to the bending in the magnetic field. In this case, we must rely on numerical methods to locate the minimum of the χ^2 surface, and to determine the errors on the parameter estimates.

Assuming that we know the initial direction of the track entering the toroid from the analysis in the calorimeter, the position on the face of the toroid is predicted. Then we have two free parameters left, which are the momentum and the charge of the track. We can still constrain the momentum of the particle if a particle stops in the toroid, and we can still at least know the minimum momentum of the particle even if it punches through the toroid, or exits side of the toroid.

Suppose we have N data points, one measured point on each plane, in the toroid. Then for a given set of parameters, in this case charge and momentum of the track, a corresponding N $\times$ N multiple scattering error matrix can be calculated. The exact position for the given parameters on each plane can be predicted by carefully following the track step by step considering energy loss due to $\frac{dE}{dX}$ and continuous bending due

to the magnetic field in the toroid. Then track parameters can be determined by searching for a minimum in χ^2 for a certain number of sets of parameters. In each set of parameters, χ^2 can be calculated using the formula,

$$\chi^2_{p,charge} = \sum_{i=1}^{N}\sum_{j=1}^{N}(x_i^m - x_i^p)M_{ij}^{-1}(x_j^m - x_j^p) \qquad \text{(A.10)}$$

where the summation is over N data points.

Noting that unlike momentum which should be searched continuously in the vicinity of the minimum value, the charge of the particle is either $+1$ or -1, we have searched χ^2- minimum for varying momenta between p_{min} and p_{max} constrained by its range in the toroid for both charge assumptions. The correct sign charge assumption will give better, or smaller χ^2, while with wrong sign charge assumption, there may not exist χ^2- minimum, or even if one finds the minimum, χ^2 value itself would be a lot larger than the one in the correct sign charge assumption. By comparing both χ^2 minimum values for both charge assumptions, one can determine both parameters, charge and momentum of the toroid entering track. Combined with the energy loss in the calorimeter, one can finally determine the charge and original energy of the particle under study.

Appendix B

SCAN RULE

Definitions

X-view = left part of picture
Y-view = right part of picture

Detector (or detector block) = bottom square

Toroid (or Toroid block) = top square

Flow direction: from bottom to top of the picture

Vertex = The point (hit) where all hit activity emerges from.

Example:

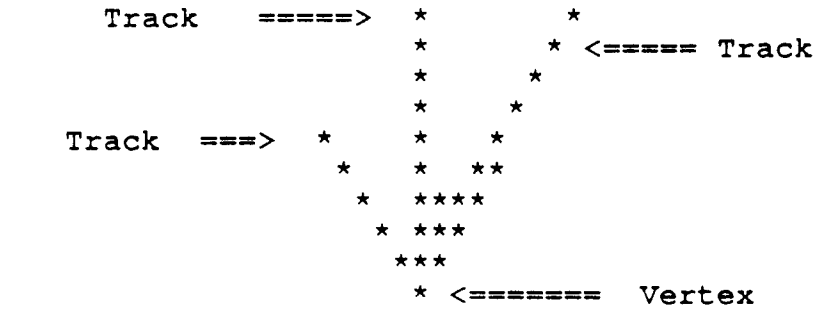

Track = Sequence of single hits in a more or less
-----   straight direction.
        Sometimes a track may include a double hit.
        Sometimes a track may have a missing hit.

Example:

Shower = A sequence of hits resembling a fat track
------   with missing hits as well as double and
         tripple hits at times.

Example:

B-track (Broken track) = A track that has a
-------   clear kink

I-track (Interacting track) = A track with a little
-------   shower near its end

Example:

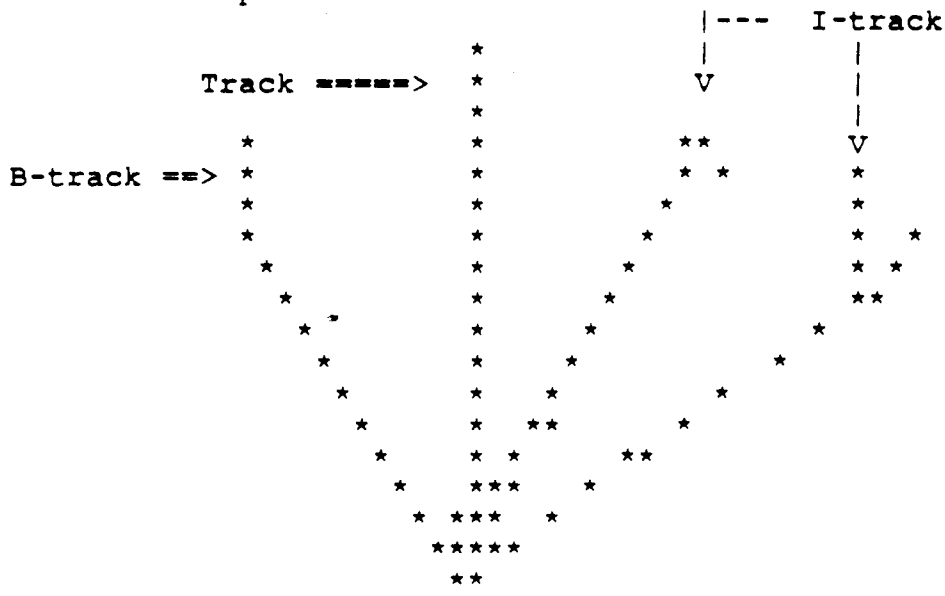

D-track = a track that starts from the vertex
-------   and ends somewhere in the detector
          or exits from the sides.

M-track = a track that starts from the vertex
-------   and extends itself into the toroid,
          having one or more hits in either view
          of the toroid.

Track length (or simply length) = number of gaps
------------ in the direction of flow from
              the vertex to the end of the track
              in the detector only.

SCAN RULES

We are looking for events which have two clearly acceptable tracks. (Caution! The event may contain in addition other tracks or clusters of hits around the vertex). Focus attention only on the two longest tracks! Ignore the rest of the junk around the vertex!

An event is acceptable when it contains two acceptable tracks in one view and at least one acceptable track in the other view.

Warnings!!

a. Sometimes two tracks may fall on top of each other in one or both views. LOOK CAREFULLY.

b. The beginning of an acceptable track (near the vertex) may be imbended in a lot of junk. Don't mind that provided that the rest of the track is clearly identifiable.

Track acceptance Criteria

A track is acceptable if

a. It is a M-track

b. It is not a B-track
c. It is not an I-track

d. It is a D-track and
   (i) length >= 30 gaps for the longest track
   (ii) length >= 24 gaps for the second longest track.